



Vourch, Clement J. (2016) *Bull's eye leaky wave antenna for terrestrial and space applications*. PhD thesis.

<http://theses.gla.ac.uk/7708/>

Copyright and moral rights for this thesis are retained by the author

A copy can be downloaded for personal non-commercial research or study, without prior permission or charge

This thesis cannot be reproduced or quoted extensively from without first obtaining permission in writing from the Author

The content must not be changed in any way or sold commercially in any format or medium without the formal permission of the Author

When referring to this work, full bibliographic details including the author, title, awarding institution and date of the thesis must be given

Glasgow Theses Service

<http://theses.gla.ac.uk/>

theses@gla.ac.uk

Bull's eye leaky wave antenna for terrestrial and space applications



Clement J. Vourch
School of Engineering
University of Glasgow

Submitted in fulfilment of the requirements for the
Degree of Doctor of Philosophy (PhD)

September 2016

Abstract

This work presents the study of Bull's eye antenna designs, a type of leaky wave antenna (LWA), operating in the 60 GHz band. This band emerged as a new standard for specific terrestrial and space applications because the radio spectrum becomes more congested up to the millimetre-wave band, starting at 30 GHz. Built on existing Bull's eye antenna designs, novel structures were simulated, fabricated and measured, so as to provide more flexibility in the implementation of wireless solutions at this frequency.

Firstly, the study of a 60 GHz Bull's eye antenna for straightforward integration onto a CubeSat is presented. An investigation of the design is carried out, from the description of the radiation mechanism supported by simulation results, to the radiation pattern measurement of a prototype which provides a gain of 19.1 dBi at boresight. Another design, based on a modified feed structure, uses a microstrip to waveguide transition to provide easier and inexpensive integration of a Bull's eye antenna onto a planar circuit.

Secondly, the design of Bull's eye antennas capable of creating beam deflection and multi-beam is presented. In particular, a detail study of the deflection mechanism is proposed, followed by the demonstration of a Bull's eye antenna generating two separate beams at $\pm 16^\circ$ away from the boresight. In addition, a novel mechanically steerable Bull's eye antenna, based on the division of the corrugated area in paired sectors is presented. A prototype was fabricated and measured. It generated double beams at $\pm 8^\circ$ and $\pm 15^\circ$ from the boresight, and a single boresight beam.

Thirdly, a Bull's eye antenna capable of generating two simultaneous orbital angular momentum (OAM) modes $l = \pm 3$ is proposed. The design is based on a circular travelling wave resonator and would allow channel capacity increase through OAM multiplexing. An improved design based on two stacked OAM Bull's eye antennas capable of producing four orthogonal OAM modes $l = (\pm 3, \pm 13)$ simultaneously is presented. A novel receiving scheme based on discretely sampled partial aperture receivers (DSPAR) is then introduced. This solution could provide a lower windage and a lower cost of implementation than current whole or partial continuous aperture.

Preface

The work presented in this Thesis was published as follows:

Journal papers

C.J. Vourch, B. Allen and T.D. Drysdale, “Planar millimetre-wave antenna simultaneously producing four orbital angular momentum modes and associated multi-element receiver array,” in *Microwaves, Antennas & Propagation, IET*, accepted for publication in the October 2016 special issue on “Millimetre Wave Systems, Circuits and Antenna Integration Challenges for Broadband Everywhere”.

C.J. Vourch and T.D. Drysdale, “V-band Bull’s eye antenna for multiple discretely steerable beams,” in *Microwaves, Antennas & Propagation, IET*, vol. 10, no. 3, pp. 318-325, Feb. 2016.

B.R. Johnson, **C.J. Vourch**, T.D. Drysdale, *et al.*, “A CubeSat for Calibrating Ground-Based and Sub-Orbital Millimeter-Wave Polarimeters (Cal-Sat),” in *Journal of Astronomical Instrumentation*, vol. 4, no. 3-4, pp. 1550007-1 - 1550007-18, Dec. 2015.

C.J. Vourch and T.D. Drysdale, “V-Band “Bull’s Eye” Antenna for CubeSat Applications,” in *Antennas and Wireless Propagation Letters, IEEE*, vol. 13, pp. 1092-1095, 2014.

Conference proceedings

C.J. Vourch and T.D. Drysdale, “Planar waveguide feed for V-band Bull’s eye antenna,” *Microwave Conference (EuMC), 2016 46th European*, London, 2016, accepted for presentation in October 2016.

T.D. Drysdale and **C.J. Vourch**, “Surface wave engineering for beam control in planar millimetre-wave antennas,” *Microwave Conference (EuMC), 2016 46th European*, London, 2016, accepted for presentation in October 2016.

C.J. Vourch and T.D. Drysdale, “Low-Profile Antenna Package for Efficient InterCubeSat Communication in S- and V-band,” in *4th Interplanetary CubeSat Workshop (iCubeSat 2015)*, London, April 2015.

C.J. Vourch and T.D. Drysdale, “Directivity enhancement of V-band “Bull’s eye” antenna with dielectric superstrate,” in *Antennas and Propagation Conference (LAPC), 2014 Loughborough*, pp. 277-280, 10-11 Nov 2014.

C.J. Vourch and T.D. Drysdale, “Parametric study of a double shifted “Bull’s eye” structure at V-band for beamforming,” in *Antennas and Propagation Conference (LAPC), 2014 Loughborough*, pp. 461-464, 10-11 Nov. 2014.

C.J. Vourch and T.D. Drysdale, “Inter-CubeSat communication with V-band “Bull’s eye” antenna,” in *Antennas and Propagation (EuCAP), 2014 8th European Conference on*, pp. 3545-3549, 6-11 April 2014.

Acknowledgements

First and foremost, I would like to thank my supervisor, Dr. Timothy Drysdale, for his strong support throughout my entire PhD program. His guidance and suggestions made this study a challenging and valuable experience. I also thank my second supervisor, Dr. Patrick Harkness, for his advice and the interesting discussions regarding CubeSat technology. Prof. Iain Thayne helped with his administrative support and provided access to CST Microwave Studio.

I would like to acknowledge financial support from the School of Engineering of the University of Glasgow through a James Watt Scholarship. I also want to acknowledge financial support from the “Principal’s Early Career Mobility Scheme: Glasgow-Columbia”. Prof. Amber Miller at Columbia University made my visit possible, and Dr. Bradley Johnson gave me the opportunity to work on the CalSat project.

The technical staff at the Electrical and Mechanical Workshop of the University of Glasgow helped in the fabrication the antenna prototypes, especially Denis Kearns, Wilson MacDougall and Alan Yuill. Also, Peter McKenna took care of the photograph and the poster printing. I also would like to thank Dr. Lourdes Ferre Llin for her help with fabrication process, and Francesco Mirando for his availability for using the equipment. I also want to thank Dr. Chong Li for his help and advice regarding the design of the experimental test bench, and Thomas O’Hara and Monageng Kgwadi for their technical support during measurements.

I want to thank my family, Liliane, Roger, Laura and Benoît, for their loving support, and last but not least my wife, Rachel.

Contents

List of Figures	xiii
List of Tables	xiv
Nomenclature	xv
1 Introduction	1
1.1 Motivation	2
1.1.1 Terrestrial applications	2
1.1.2 Inter-satellite communication	5
1.2 Aim & Scope	7
1.3 Outline	8
2 Background	10
2.1 Antenna definition and figures of merit	10
2.1.1 Definition	10
2.1.2 Radiation pattern, directivity and gain	11
2.1.3 Polarisation	16
2.1.4 Impedance bandwidth	18
2.1.5 Link budget	20
2.2 Typical antennas	21
2.2.1 Dipole antenna	22
2.2.2 Patch antenna	22
2.2.3 Horn antenna	22
2.3 Bull’s eye antenna concept	25
2.3.1 Leaky wave antenna (LWA)	25

2.3.2	Bull's eye antenna description	27
2.3.3	Evolution and latest advances	31
2.4	Chapter summary	33
3	Methods	34
3.1	Simulation tools	34
3.1.1	Finite-difference time-domain (FDTD) method	35
3.1.2	Rigorous coupled-wave analysis (RCWA) method	38
3.2	Fabrication processes	41
3.2.1	Mechanical milling process	41
3.2.2	Electrical discharge machining process	43
3.2.3	Photolithography process	44
3.3	Measurement tools	44
3.3.1	Anechoic chamber	44
3.3.2	V-band test bench	45
3.3.3	Gain Transfer Method	49
3.4	Chapter summary	49
4	Bull's eye antenna design and feed	51
4.1	Bull's eye antenna operating at 60 GHz	51
4.1.1	Design and simulation	51
4.1.2	Measurements	55
4.2	Alternative feeding structure	57
4.2.1	Microstrip	58
4.2.2	Design and simulation	59
4.2.3	Fabrication and measurement	64
4.3	Chapter summary	67
5	Bull's eye antenna improvements	70
5.1	Fixed beam deflection	71
5.1.1	Single direction shift concept	71
5.1.2	One dimensional grating model	74
5.1.3	Multiple symmetrical beams	77
5.1.4	Measurements	80
5.2	Sectorial Bull's eye antenna	82

5.2.1	Steering concept	82
5.2.2	Design and simulation	86
5.2.3	Fabrication and measurements	88
5.3	Conformal Bull’s eye antenna	90
5.3.1	Conformal Bull’s eye antenna with constant grating	90
5.3.2	Model for a conformal Bull’s eye antenna with adjusted grating	91
5.4	Chapter summary	96
6 Orbital angular momentum generated by Bull’s eye antenna		98
6.1	Orbital Angular Momentum	99
6.2	Bull’s eye antenna for OAM generation	102
6.2.1	Single OAM Bull’s eye antenna	102
6.2.2	Stacked OAM Bull’s eye antenna for multiple modes gen- eration	110
6.3	Receiving scheme for multi OAM modes	112
6.3.1	Partial aperture receivers for multiplexed OAM modes	115
6.3.2	Discrete multi-mode receiver	116
6.3.3	Four element receiver for stacked OAM antenna	119
6.4	Chapter summary	121
7 Conclusions and future work		123
7.1	Bull’s eye antenna design and planar feeding technique	125
7.1.1	Future work	126
7.2	Beam deflection and beam steering	126
7.2.1	Future work	127
7.3	Orbital angular momentum multiplexing	127
7.3.1	Future work	128
7.4	CalSat Project	129
A Regulatory policies for frequency spectrum allocation		132
B Ring shifting schemes		135
C Low-profile antenna package for inter-CubeSat communication		138

List of Figures

1.1	Plot of the specific atmospheric attenuation (dB/km) due to oxygen and water vapour as a function of frequency, using the model from the Recommendation P.676.10 of the International Telecommunication Union, 2013.	4
1.2	Picture of a 3U CubeSat (UKube-1) with added dimensions . . .	5
2.1	Illustration of the near-field and far-field regions of an antenna where D is the diameter of the sphere that encloses the antenna. .	11
2.2	Definition of the spherical coordinate system for the radiation pattern of an antenna located at the origin 0.	12
2.3	Polar plots of two main types of radiation pattern: (a) omnidirectional and (b) directional pattern.	15
2.4	Linear and circular polarisation schemes for a plane wave travelling in the z -direction.	17
2.5	Illustration of the E- and H-plane definition for a linearly x -polarised horn antenna.	18
2.6	Plot of an example S_{11} parameter showing the bandwidth defined between f_L and f_H for $S_{11} < -10$ dB for a notional antenna.	19
2.7	Schematic of the line of sight point to point transmission link modelled by the Friis equation where P_{Tx} is the transmitted power, G_{Tx} is the gain of the transmitting antenna, G_{Rx} is the gain of the receiving antenna, and P_{Rx} is the received power.	20
2.8	Illustration of (a) a half-wave dipole showing the electric field distribution, and (b) the 3D toroid-shaped far-field radiation pattern.	23

LIST OF FIGURES

2.9	Illustration of rectangular patch antenna with an inset for impedance matching, operating at 10 GHz, and the 3D far-field radiation pattern in transparency.	24
2.10	Illustration of a 23 dBi rectangular horn antenna with the 3D far-field radiation pattern at 60 GHz.	25
2.11	Illustration of a uniform LWA made of a rectangular waveguide with a continuous slot, with incoming travelling wave in the waveguide (large red arrow) and leaky wave (black arrows).	26
2.12	Illustration of a periodic LWA made of a printed, metallic strip, grating-pattern of period Λ , with incoming travelling surface wave (large red arrow) and leaky wave (black arrows).	27
2.13	Volume comparison between a standard Bull's eye antenna and rectangular horn antenna both operating at 60 GHz. The low profile of the Bull's eye antenna allows straightforward integration on the face of a CubeSat.	28
2.14	Photographs of the two types of Bull's eye antenna: a corrugated Bull's eye antenna (from [52]) and a printed Bull's eye antenna (from [54]).	29
2.15	Illustration of the coupling mechanism between a surface wave of angular wavenumber k_z and the free-space of wavenumber k_0 at an angle θ through a grating of period Λ . For spatial harmonic $n = -1$, $k_\Lambda = \frac{2\pi}{\Lambda}$	30
2.16	Time-line of Bull's eye antenna main advances for microwave, millimetre-wave and terahertz regimes. My contributions to the field since the start of my PhD (October 2012) are listed in red diamond markers.	33
3.1	Illustration of a 3D Yee lattice. The arrows represent the quantities associated with the (i, j, k) cell.	35
3.2	Illustration of the electric and magnetic symmetry conditions for an analysis of a horn antenna in CST MWS.	38
3.3	Illustration of a unidirectional grating of period Λ	39
3.4	Drawing schematic of a standard UG385/U flange for WR-15 waveguides.	42
3.5	Schematic of the electrical discharge machining process illustrating the work piece, the electrode and the dielectric fluid.	43

LIST OF FIGURES

3.6	Characteristics of the EHP-18PCL pyramidal absorber covering the walls of the anechoic chamber.	46
3.7	Test bench for V-band radiation pattern and gain measurement.	47
3.8	Schematic example showing a S_{21} parameter acquisition and data post-processing for displaying of the radiation pattern for θ between -90° and $+90^\circ$ at frequency f_0	48
4.1	Perspective schematic view of a seven-ring Bull's eye antenna with associated dimensions. Dimensions for a structure operating at 60 GHz are shown in Table 4.1	52
4.2	Simulated S_{11} (dB) and maximum gain (dBi) between 55 and 65 GHz	54
4.3	Measured and simulated, E-plane (a) and H-plane (b) radiation pattern	56
4.4	Fabricated 60 GHz Bull's eye antenna on the face of a 2U CubeSat chassis	57
4.5	Perspective view of a microstrip where w is the width of the conducting strip, h is the thickness of the dielectric substrate, and ϵ_r is the relative permittivity of the dielectric substrate.	58
4.6	Schematic side view (cut away) of the microstrip-based feed providing coupling from the microstrip (quasi-TEM mode) to the Bull's eye structure through a hollow waveguide (TE_{10} mode) and a resonant square patch (TM_{01} mode).	60
4.7	Plot of the calculated specific attenuation (dB/cm) for a 0.508 mm thick microstrip of $50\ \Omega$ impedance using the R04350B, R04003C, and RT/duroid 5880 laminates.	61
4.8	Millimetre dimensions of the microstrip transition from the top (a), and bottom (b). The top view has an inset showing an enlarged view of square patch, while the bottom view, the tapered ground under the patch	62
4.9	Exploded perspective view the Bull's eye antenna with the microstrip to waveguide transition with inset of S_{11} values as a function of waveguide transition thickness.	63
4.10	Plot of simulated S_{11} of the Bull's eye antenna fed with the microstrip-to-waveguide transition (M-feed, solid red line) and with a WR-15 waveguide (W-flange, blue circle markers).	64

4.11	Illustration of the undercut concept under an isotropic wet etch process and micrograph showing a perspective view of the test sample showing the substrate after the etch (left part of the picture) and the remaining copper (right part of the picture).	66
4.12	Photograph of the fabricated Bull’s eye antenna mounted on the microstrip to waveguide transition	67
4.13	Simulated and measured E-plane (a) and H-plane (b) normalised radiation pattern at 60 GHz for Bull’s eye antenna fed with the microstrip-to-waveguide transition structure.	68
5.1	Illustration of how the Bull’s eye antenna’s main beam is deflected by shifting the centre of the rings along the E-plane (short side of the subwavelength aperture). Each subfigure shows a polar plot of linear gain above a perspective view of half of the antenna. . . .	72
5.2	Plot of E-plane radiation patterns for an E-plane single shift ring structure for shifts of: 0.00 mm (A), 1.00 mm (B), 2.00 mm (C) and 2.67 mm (D).	73
5.3	Plot of H-plane radiation patterns for H-plane single shift ring structure for shifts of: 0.00 mm (A), 1.00 mm (B), 2.00 mm (C) and 2.67 mm (D).	74
5.4	Plot comparing the simulated deflection angle of optimised (modified) and unoptimised (canonical) Bull’s eye antennas to the coupling angle of the associated one dimensional rectangular profile gratings, as a function of the effective grating period $\Lambda = \Lambda_0 + Shift$. 76	76
5.5	Plot of the E-plane radiation patterns (1); and E-plane double shift rings structure with corresponding 2D radiation pattern for shifts of 0.00 mm (A), 1.00 mm (B), 2.00 mm (C) and 2.67 mm (D). . . .	78
5.6	Plot of the H-plane radiation patterns (1); and H-plane double shift rings structure with corresponding 2D radiation pattern for shifts of 0.00 mm (A), 1.00 mm (B), 2.00 mm (C) and 2.67 mm (D). 79	79
5.7	Plot of the E-plane radiation patterns (1); and E-plane asymmetrical shift rings structure with corresponding 2D projection radiation pattern for shifts of 0.00 mm (A), 1.00 mm (B), 2.00 mm (C) and 2.67 mm (D).	81

LIST OF FIGURES

5.8 (a) Fabricated 2.00 mm E-plane double symmetrical shift Bull’s eye antenna, (b) Normalized simulated and measured E-plane radiation pattern.	83
5.9 E-field distribution and gain (dBi) versus α ($^\circ$) representing the angular active area, for a Bull’s eye antenna with seven indented rings.	84
5.10 Simulation results for a Bull’s eye antenna in position <i>Shift</i> = 0.0 mm with three different paired sectors with single shift of <i>Shift</i> = 0.0, 1.0 and 2.0 mm.	86
5.11 Exploded view the mechanically steerable sectorial Bull’s eye antenna with three pairs of sectors showing from bottom to top: a waveguide extension, a fixed base, a corrugated rotating plate with three paired sectors and mask plates.	87
5.12 Top view of the fabricated and assembled three-pair sectorial Bull’s eye antenna in position in <i>Shift</i> = 2.0 mm.	88
5.13 Simulation and measurement E-plane radiation patterns for three different configurations (<i>Shift</i> = 0.0, 1.0 and 2.0 mm) of the sectorial Bull’s eye antenna. The shift in the main lobe on the negative angle side is attributed to a systematic misalignment error in the measurement plane of the Bull’s eye antenna.	89
5.14 Cut view showing the parallel direction of a leaky wave emitted from a curved Bull’s eye antenna with (a) a constant grating and (b) an adjusted grating.	91
5.15 Illustration of the loss of directivity for a conformal Bull’s eye antenna with constant grating $\Lambda = 4.53$ mm along the E-plane. . .	92
5.16 Schematic view of the conformal Bull’s eye antenna dimensions for the model.	93
5.17 Modelled cut view of a conformal Bull’s antenna model with a radius of curvature $R = 75$ mm.	94
5.18 Illustration of the convex conformal Bull’s eye antenna with adjusted grating dimensions along the E-plane for the $R = 75$ mm, and simulated E- and H-plane radiation patterns.	95
5.19 Summary of the results presented in Chapter 5.	97

6.1	Illustration of the helicoidal wavefront of an electromagnetic wave travelling along the z -axis and carrying OAM mode $ l > 0$	100
6.2	Magnitude and distribution of the electric field on a $80 \times 80 \text{ mm}^2$ plane, 50 mm above the source, for OAM modes $l = 0$ (a,b), +1 (c,d) and +2 (e,f) at 60 GHz.	101
6.3	Perspective view of an OAM Bull's eye antenna with cut-away view of the central resonator for OAM mode $l = \pm 3$	104
6.4	Dimensions of the circular travelling wave resonator and surrounding Bull's eye antenna.	105
6.5	Plot of the simulated null width ($^\circ$) and maximum gain (dBi) as a function of the number of rings of an OAM Bull's eye antenna for $l = \pm 3$	106
6.6	Perspective view of radiating top side with projected absolute electric field on a $160 \times 160 \text{ mm}^2$ plane, 50 mm above the surface the antenna.	106
6.7	Far-field radiation pattern of the Bull's eye OAM antenna and comparison with an eight-element array of diameter $D = 30$ mm made of open-ended WR-15 waveguides.	108
6.8	Phase distribution for the E_θ component on a $160 \times 160 \text{ mm}^2$ plane, 50 mm above the antenna.	109
6.9	Mode purity for three different angles of θ , confirming the mode is $l = +3$. Similar results are obtained for the $l = -3$. The polar angle θ , the angular separation α and the phase difference between two points ($\phi_2 - \phi_1$) are defined in the inset.	110
6.10	Stacked OAM Bull's eye antenna for $l = \pm 3$ and ± 13 , with red for the $l = \pm 3$ structure and green for the $l = \pm 13$ structure.	111
6.11	Magnitude and phase of the electric field distribution on a $173 \times 173 \text{ mm}^2$ plane, 50 mm (10λ) above the OAM stacked Bull's eye antenna.	113
6.12	Simulations of the double ring resonator antenna for modes $l = (+3, +13)$ (results for $l = (-3, -13)$ are similar).	114
6.13	Schematic of the element positions $[\phi_1, \phi_2, \phi_3, \phi_4]$ on the receiving plane for DSPAR or USPAR with $N = 4$ elements.	117
6.14	Results of Monte Carlo simulation and illustration of four-way orthogonality for receivers at position $\phi = 10, 43, 61, \text{ and } 94^\circ$	120

LIST OF FIGURES

6.15	Four element receiver array design optimised to suit transmissions from dual stacked OAM Bull's eye antenna.	122
7.1	Plan view schematic of a microstrip-based, 90° hybrid coupler, and microstrip-to-waveguide transition proposed in Section 4.2.	129
7.2	Exploded view of CalSat showing the different sub-systems. The 4 circular horn antennas (47.1, 80, 140 and 309 GHz) are located in the payload.	130
7.3	Illustration of the first version version of the CalSat payload, and proposed single plate alternative integrating two Bull's eye antennas for the 47.1 and 80 GHz tones.	131

List of Tables

3.1	Dimensions in millimetres of a standard UG385/U flange for WR-15 waveguides.	43
4.1	Dimensions in millimetres of a Bull’s eye antenna operating at 60 GHz with the initial design rules provided by Beruete <i>et al.</i> [56] and the proposed improvements.	53
4.2	Simulated gain versus number of indented rings, physical aperture, effective aperture, and aperture efficiency	54
4.3	Millimetre dimensions of the microstrip to waveguide feed transition	61
5.1	Angle deflection and gain for shifts in the E-plane.	73
5.2	Angle of deflection and gain according to single H-plane ring shift.	74
5.3	Deflection angle, gain and beamwidth according to double E-plane ring shift.	77
5.4	Deflection angle, gain and beamwidth according to double H-plane ring shift.	80
6.1	Dimensions (mm) of the circular travelling wave resonator and surrounding Bull’s eye antenna.	104
6.2	Orthogonal mode pairs for partial apertures of $2\pi/n$, for a selection of starting mode numbers. The number of supported orthogonal modes is indicated by the location of the ‘ \pm ’ symbol.	116
6.3	Side mode rejection ratio (SMRR, dB) for a DSPAR (non-uniform spacing) and USPAR (uniform spacing) with $N = 4$ receivers for selected mode pairs from Table 6.2.	118

Nomenclature

Symbols

β	phase constant
Λ	period
λ	wavelength
E	electric field vector
H	magnetic field vector
ε_r	relative permittivity
c	speed of light in a vacuum, 2.998×10^8 m/s
k	wavenumber
dB	decibel
dBi	decibel isotropic
GHz	gigahertz, 10^9 Hz
Hz	hertz
m	metre
s	second

Acronyms

AUT	antenna under test
-----	--------------------

NOMENCLATURE

CNC	computerised numerical control
COTS	commercial off-the-shelf
CPW	coplanar waveguide
CST MWS	computer simulation technology microwave studio
FDTD	finite-difference time-domain
FIT	finite integration technique
IEEE	institute of electrical and electronics engineer
IF	intermediate frequency
LWA	leaky wave antenna
MMIC	monolithic microwave integrated circuit
OAM	orbital angular momentum
PCB	printed circuit board
RCWA	rigorous coupled-wave analysis
SHF	super high frequency, band of frequency between 3 and 30 GHz
SIW	substrate integrated waveguide
TE	transverse electric
TEM	transverse electromagnetic
TM	transverse magnetic
V-band	band of frequency between 40-75 GHz
VNA	vector network analyser
WLAN	wireless local area network
WPAN	wireless personal area network

Chapter 1

Introduction

The so-called ‘digital economy’ is driving an ever-increasing demand for communication bandwidth [1]. The electromagnetic spectrum is already heavily congested at frequencies up to the super high frequency (SHF) band (3 – 30 GHz) [2]. The millimetre-wave band, above 30 GHz, is slightly less congested, with academic and industrial interest focused on the 60 GHz license-free band, which offers 6 to 9 GHz of bandwidth worldwide, with some small regional variations affecting the precise band boundaries. This interest comes despite strong atmospheric attenuation due to oxygen [3], which in some applications is even viewed favourably, as an aid to security enhancement by reducing interferences in dense networks. Further, there is 11.8 GHz of bandwidth reserved for the inter-satellite service [4].

These conditions resulted in the emergence of new regulatory policies and standards, such as the IEEE 802.15.3c-2009 for wireless personal area network (WPAN) applications targeting short range mobile applications in the 57 to 66 GHz spectral interval [5]. These applications favour reconfigurable and fast adaptive antenna systems to cope with moving users. But fixed point-to-point wireless communication systems are also necessary for applications such as backhaul or wireless fibre extensions. For example the 60 GHz band can provide an alternative solution to fibre-optic systems, to overcome physical path constraints such as rivers or highways, and decrease the installation time and cost [6]. For such invariant or slow-moving environments, improving the antenna performance is necessary to increase the transmission range and the flexibility. A slow moving environment is defined as a configuration requiring sparse antenna reconfigura-

tions induced by an infrequent change in the surrounding environment, or in the relative position of a receiver. Examples include blockage of the line of sight by, for example, a moveable bridge or, the reconfiguration of a swarm of satellites.

Subsequently, the recent rise in use of CubeSats for space exploration presents an exciting use-case, because it is likely that CubeSats will work in swarms, separating data gathering from data processing, and thus benefiting from high data rate communications.

The rest of this Chapter is organised as follows. The first Section of this Chapter outlines the motivation behind the work presented in this Thesis, which is driven by emerging applications for 60 GHz communications on Earth and in space. The second Section defines the scope of this Thesis, and the third Section outlines the organisation of the content.

1.1 Motivation

This Section presents the motivation for investigating the Bull's eye antennas presented in this Thesis. In particular, the motivation arises from the emergence of the 60 GHz band as a future standard for high data rate terrestrial short range links, and for inter-satellite communication schemes, both of which are expected to require low cost, high gain, directive antennas in order to be fully exploited.

1.1.1 Terrestrial applications

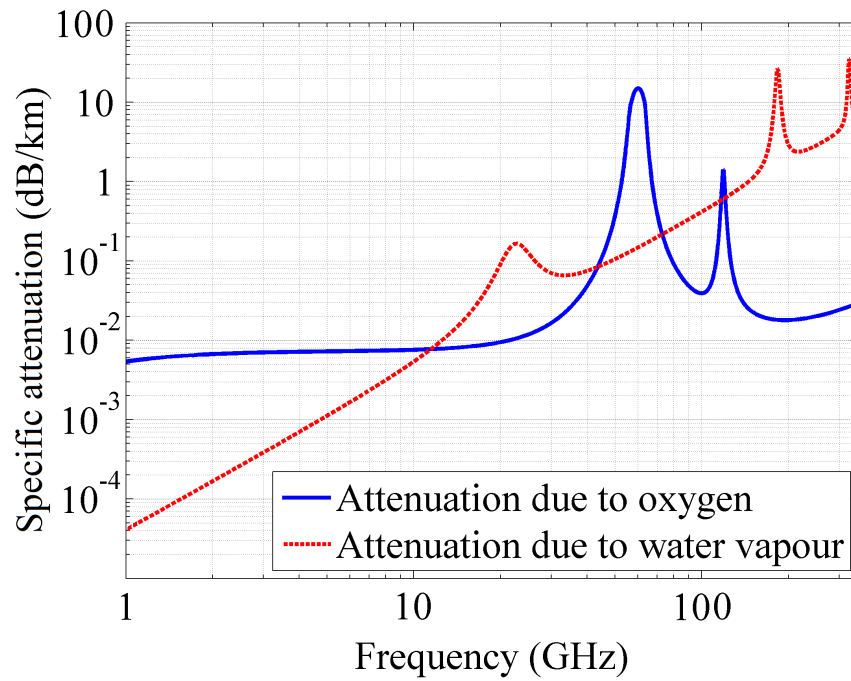
Wireless links using unlicensed bands have often the advantage of being cost effective and fast to deploy. The 60 GHz band is emerging as an alternative to lower frequency bands to improve short range terrestrial communication [7]. The main drivers for the use of the 60 GHz band are the large available bandwidth and the need to move away from the congested 2.45 GHz and 5 GHz bands [8]. The increase in potential users pushed the main regulatory institutions such as the Federal Communications Commission (FCC) to regulate the 60 GHz band [9]. An overview of the regulations for terrestrial applications is presented in Appendix A.

Subsequently, several specifications emerged to support and regulate the use of the 60 GHz band. For example the IEEE 802.11ad standard allocates four 2.16 GHz bandwidth channels between 58.24 and 65.88 GHz, allowing data rates up to

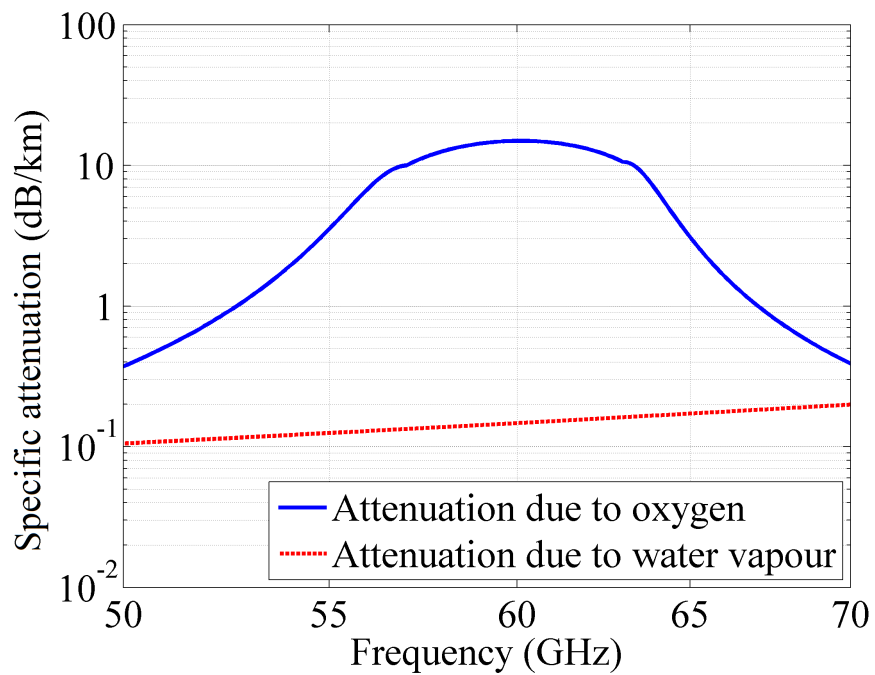
6.75 Gbit/s [10]. Medium range wireless links, such as the backhaul sections of a wireless local area network (WLAN), are favoured with this IEEE standard [11].

Other applications require a short-range wireless link with high data rate transmission within a WPAN, such as radio links within data centres using the recent IEEE 802.15.3c standard. These wireless systems can achieve cost-saving by eliminating cables, which otherwise account for up to 8% of the infrastructure cost [12]. In the configuration of fixed transmitters and receivers, directional and steerable antennas can be used to maximise the energy efficiency by improving the link budget. In this specific slow varying environment, the link distance and energy efficiency are prioritised over steering speed, so mechanically steerable antennas can become attractive because they avoid the expense, complexity and insertion losses associated with electronic steering.

Such applications require directional antennas to overcome the limited power of millimetre-wave sources and the 60 GHz band propagation properties, and avoid interferences in dense networks. The 60 GHz band suffers from a particularly strong atmospheric attenuation mainly caused by oxygen molecules [13]. The total specific atmospheric attenuation reaches 15 dB/km at 60 GHz at sea level. This attenuation must be accounted for in radio link budgets, whereas for frequencies below 30 GHz, atmospheric attenuation can often be neglected for short range transmissions. A simplified model based on curve-fitting of spectroscopic measurements can be used to provide an estimation of gaseous attenuation [14]. For altitudes ranging from sea level to 5 km high, this model agrees within an average error of about $\pm 15\%$ for major absorption lines, with a maximum absolute error of 0.7 dB/km near 60 GHz. Figure 1.1(a) shows the plot of the attenuation caused by oxygen molecules and water vapour, calculated between 1 and 350 GHz with the model described in [14]. Figure 1.1(b) shows a close up of the same curve between 50 and 70 GHz. This model is defined separately for three frequency bands (1 to 54 GHz, 54 to 57 GHz, and 57 to 350 GHz), resulting in two minor discontinuities at 54 and 57 GHz visible in Figure 1.1(b).



(a) Specific atmospheric attenuation between 1 and 300 GHz.



(b) Specific atmospheric attenuation between 50 and 70 GHz.

Figure 1.1: Plot of the specific atmospheric attenuation (dB/km) due to oxygen and water vapour as a function of frequency, using the model from the Recommendation P.676.10 of the International Telecommunication Union, 2013.

1.1.2 Inter-satellite communication

Actors in the space industry have focused on cost reduction [15], leading to the realistic prospect of missions using swarms of small satellites [16] for Earth-observation and remote sensing [17].

High bandwidth communication is expected to play a critical role in enabling these missions. In order to understand the constraints this would place on the antenna, it is useful to describe the small satellite platform itself.

A type of small satellite is called CubeSat and combines a small size, a standardised chassis and the intensive use of commercial off the shelf (COTS) components [18]. CubeSat is a class of nano-satellite, weighing 1.0 to 10.0 kg, and consisting of at least one block, sized $10 \times 10 \times 10 \text{ cm}^3$ [19]. This size is referred to as 1U and larger sizes of CubeSats are usually defined as multiples of this (e.g. 3U). Figure 1.2 shows the picture of a 3U CubeSat.

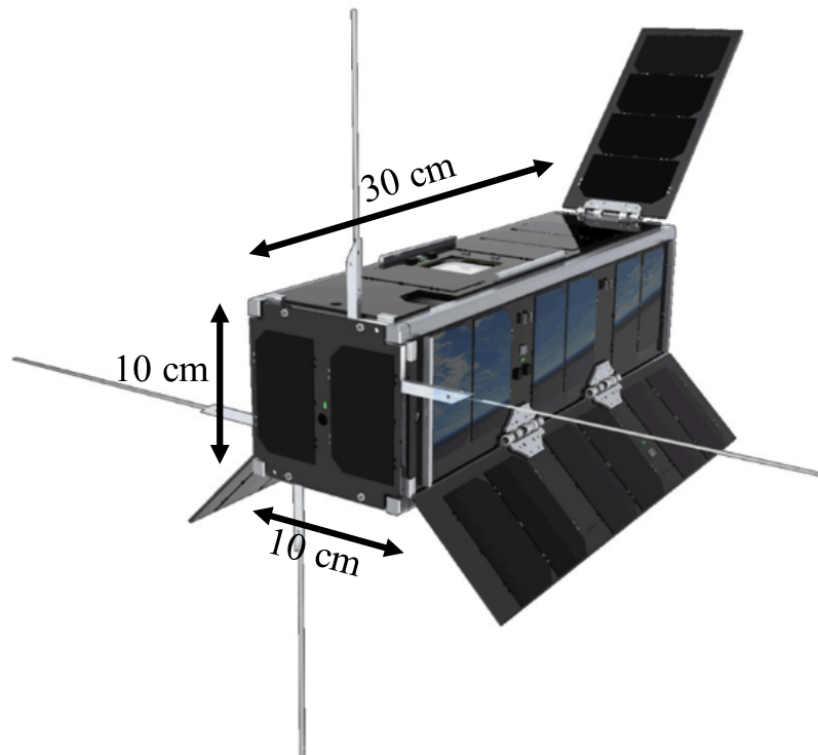


Figure 1.2: Picture of a 3U CubeSat (UKube-1) with added dimensions ©Clyde Space 2016 - Image supplied by ClydeSpace Ltd.

The popularity of CubeSats is growing, with 108 launched in 2015 alone [20]. The price of CubeSat missions is lower than traditional satellite missions for two main reasons:

1. CubeSat development is mainly based on simple, non-redundant systems and extensive use of COTS components [21]. A CubeSat can typically be developed in less than two years [22]. However, this decreases the reliability of the mission, with nearly one quarter of missions failing since 2000, including the deaths-on-arrival (15.4%) and early losses (7.4%) [20];
2. CubeSats are launched, for the most part, as auxiliary payloads on a ‘rideshare’ approach, using spare space in large rockets. This decreases the overall cost of the launch, but limits the number of launch opportunities and restrains the type of available orbits. Recent advances are expected to provide more suitable launch system such as two-stage rockets targeting nominal payloads of 150 kg for 500 km circular orbits [23, 24].

An organised CubeSat swarm appears to be a practical and affordable method of achieving missions requiring a large aperture in orbit [25]. A swarm will most likely consist of CubeSats distributed across a finite planar region, from a few hundred metres to tens of kilometres across, depending on the number of members [26, 27]. Beside spreading the risk and the cost of a mission, swarms can be far larger than the arms of even the largest conventional satellites, which are currently limited to tens of metres for telescopic booms [28], or a hundred metres for complex modular-mesh deployment structures [29]. For example, the Orbital Low Frequency ARray (OLFAR) mission is designed for radio astronomy observation below 30 MHz [30, 31]. At those low frequencies, a large aperture of over 10 km is needed to achieve the required spatial resolution, so a CubeSat swarm could operate as a distributed aperture synthesis array.

For inter-satellite communication, a number of systems have been developed which use radio frequencies from very high frequency (VHF) upwards, and even optical links [32]. However, the limited size and payload of the CubeSat platform brings new challenges in the integration of the communication sub-systems. To date, most CubeSat communication sub-systems use a VHF, ultra high frequency (UHF), or S-band (2-4 GHz) link coupled with low profile antennas (e.g. patch

antennas) or deployable structures (e.g. deployable dipole antennas [33]), in order to meet the size, weight and cost requirements. Not all CubeSat missions require high data rate millimetre-wave communication links, but there is a need for improving the capabilities of inter-satellite links when required for three main reasons:

1. Radio links operating at frequencies below S-band require large antennas, particularly when directional antennas are required. This is because the size of an antenna is proportional to the gain and inversely proportional to the frequency-squared of operation.
2. The emergence of new terrestrial applications using the 60 GHz band offers numerous low-cost COTS components which are a key point of the CubeSat ethos.
3. Some specific space applications are more and more demanding with respect to data throughput requirements, with data rate expected to exceed 6 Mbit/s [34].

To this extent, the key step toward developing more efficient inter-satellite links is the identification of the frequency band which suits the CubeSat design requirements and international regulations. The Inter-Satellite Service bands are exclusively reserved for communications between satellites [4, 35]. In outer-space there is little of the strong attenuation that occurs lower in the atmosphere. For these reasons, the 60 GHz band appears to be a promising option for future inter-satellite links within a CubeSat swarm. An antenna operating at 60 GHz is 25 times smaller than an antenna with similar performance operating in the unlicensed 2.45 GHz band.

1.2 Aim & Scope

The aim of this Thesis is to address these needs by designing and demonstrating suitable antennas that operate in the 60 GHz band. Specifically to:

1. develop a 60 GHz Bull's eye antenna to suit a CubeSat chassis;
2. investigate planar waveguide for the purpose of cost reduction;

3. study the modifications to the ring structure of the Bull's eye antenna so as to generate and deflect multiple beams, and create a discretely steerable Bull's eye antenna; and,
4. explore the possibility of generating orbital angular momentum modes, with the aim of improving spectral efficiency in line of sight links.

Given that developments in the 60 GHz band are still at a relatively early phase, the aim of this study is to investigate Bull's eye antennas' capabilities. It is not the aim of this study to demonstrate the Bull's eye antenna within the context of a specific application, but rather to offer designs with improved performance that benefit emerging terrestrial and space applications.

1.3 Outline

The Thesis is organised as follows:

Chapter two provides a background of leaky wave antennas, a class of antennas to which the Bull's eye antenna belongs, followed by an outline of recent Bull's eye antenna development. The first Section describes the key figures-of-merit for the study of antennas. The second Section introduces the concept of a periodic, leaky wave and Bull's eye antenna.

Chapter three presents the simulation methods, fabrication processes and the measurements tools used in the study of Bull's eye antennas.

Chapter four gives details of the design, simulation data, and measurements of a standard Bull's eye antenna operating at 60 GHz. Subsequently, an alternative feeding technique for the Bull's eye antenna, based on a microstrip to waveguide transition, is investigated.

Chapter five explores the beam deflection capabilities of the Bull's eye antenna designs where deflected single beam, deflecting double beams, and discretely steerable beams are considered. Subsequently, the design of a conformal Bull's eye antenna is proposed to allow integration on convex surfaces.

Chapter six explores the production of orbital angular momentum (OAM) modes with the Bull's eye antenna. Designs producing two and four modes are considered. A new receiving scheme called DSPAR is also introduced, which

increase the number of mode choices available to a partial aperture receiver of OAM modes.

Chapter seven concludes the Thesis, and presents suggestions for future work.

Chapter 2

Background

This Chapter sets out the background material upon which the work in this Thesis builds. This Thesis is primarily concerned with the design of Bull’s eye antennas operating at millimetre-wave frequencies. The first Section of this Chapter starts by defining the role of an antenna and presenting several key performance metrics. Three common types of antennas are presented in the second Section, so as to show the typical performance available using conventional designs. Then, in the third Section, the concept of leaky wave antennas (LWAs) is introduced. A LWA relies on a surface wave, which is coupled to free space in a controlled way. In the case of a periodic LWA, the coupling mechanism is dictated by the surface profile. The Bull’s eye antenna is a type of periodic LWA. Its behaviour is outlined, along with a description of the evolution of its design to date.

2.1 Antenna definition and figures of merit

This Section defines the concept of antennas and the key figures of merit used to quantify their performance.

2.1.1 Definition

An antenna is defined by the *IEEE Standard Definitions of Terms for Antennas* as a means for radiating or receiving radio waves [36]. More specifically, an antenna is the ‘structure associated with the region of transition between a guided wave

2.1 Antenna definition and figures of merit

and a free-space wave, or vice versa' [37]. The guided wave to free space transition is a key factor determining the quality on the radio link. Practical systems must eventually consider the impact of the propagation environment such as in Section 1.1.1 & 1.1.2, but it is useful to describe the behaviour of the fields around the antenna in isolation first. Studies of propagation in practical systems are outside the scope of this Thesis.

In the case of a vacuum surrounding the antenna, two distinct regions can be defined as shown in Figure 2.1:

1. The near-field region is the region immediately surrounding the antenna, and extends up to the far-field region.
2. The far-field region is furthest from the antenna, starting at a distance of $r = 2D^2/\lambda$, where D is the maximum antenna dimension and λ is the free space wavelength. In this region the field distribution is independent at distance from the phase centre of the antenna.

The far-field can be seen as the Fourier transform of the near-field, which requires a full vector description of the E and H-field in the near-field region.

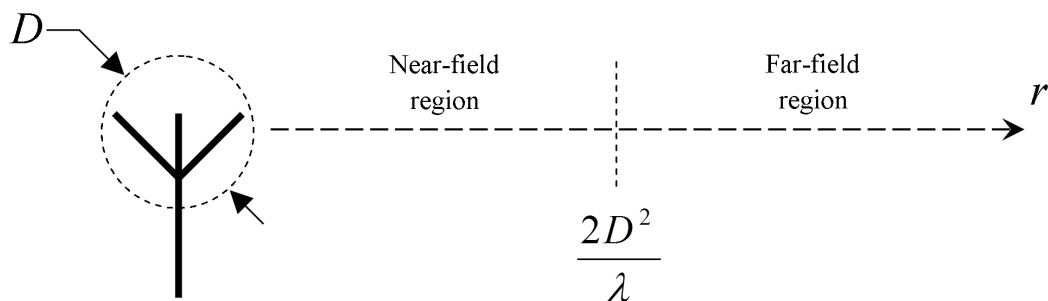


Figure 2.1: Illustration of the near-field and far-field regions of an antenna where D is the diameter of the sphere that encloses the antenna.

2.1.2 Radiation pattern, directivity and gain

The radiation pattern of an antenna is the spatial representation of the radiated power as a function of the direction [38]. The far-field power radiation patterns are most commonly used and are depicted using a spherical coordinates systems (ϕ, θ, r) , as defined in Figure 2.2.

2.1 Antenna definition and figures of merit

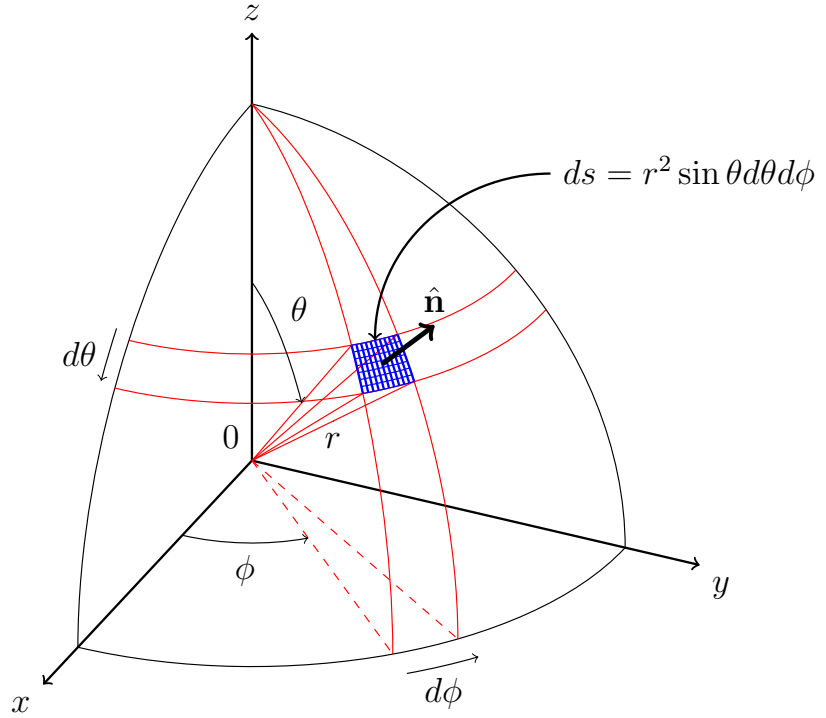


Figure 2.2: Definition of the spherical coordinate system for the radiation pattern of an antenna located at the origin 0.

In the far-field region, the instantaneous total radiated power \mathcal{P}_{rad} is the integral of the instantaneous Poynting vector \mathcal{W} [39] over the entire surface of a sphere S :

$$\mathcal{P}_{rad} = \iint_S \mathcal{W} \cdot \hat{\mathbf{n}} ds = \iint_S (\mathcal{E} \times \mathcal{H}) \cdot \hat{\mathbf{n}} ds, \quad (2.1)$$

where $\mathcal{E} = \text{Re}[\mathbf{E} \exp(j\omega t)]$ is the instantaneous electric field intensity with \mathbf{E} the electric field, $\mathcal{H} = \text{Re}[\mathbf{H} \exp(j\omega t)]$ is the instantaneous magnetic field intensity with \mathbf{H} the magnetic field, $\hat{\mathbf{n}}$ is the outward directed unit vector normal to the surface of the sphere, and ds is an infinitesimal element of the sphere.

Similarly, the time-average radiated power P_{rad} can be calculated by integrating the time-averaged Poynting vector, also called time average vector power density, written $\mathbf{P}_{avg} = \frac{1}{2} \text{Re}[\mathbf{E} \times \mathbf{H}^*]$:

$$P_{rad} = \iint_S \mathbf{P}_{avg} \cdot \hat{\mathbf{n}} ds = \frac{1}{2} \iint_S \text{Re}(\mathbf{E} \times \mathbf{H}^*) \cdot \hat{\mathbf{n}} ds. \quad (2.2)$$

2.1 Antenna definition and figures of merit

Expanding Equation 2.2, with $\mathbf{P}_{avg} = P_{avg} \cdot \hat{\mathbf{n}}$ and $ds = r^2 \sin \theta d\theta d\phi$:

$$P_{rad} = \int_0^{2\pi} \int_0^\pi P_{avg} r^2 \sin \theta d\theta d\phi = \int_0^{2\pi} \int_0^\pi P_{avg} r^2 d\Omega. \quad (2.3)$$

Hence the radiation intensity defined as $I(\theta, \phi) = P_{avg} r^2$ is the power radiated by an antenna per unit solid angle $d\Omega = \sin \theta d\theta d\phi$. Subsequently, the average radiation intensity over the entire sphere surface can be written as:

$$I_{avg} = \frac{\int_0^{2\pi} \int_0^\pi I(\theta, \phi) d\Omega}{4\pi}. \quad (2.4)$$

The directivity $D(\theta, \phi)$ of an antenna is defined as the ratio of the radiation intensity in a given direction $I(\theta, \phi)$ to the radiation intensity averaged over all directions I_{avg} , and can be written as:

$$D(\theta, \phi) = \frac{I(\theta, \phi)}{I_{avg}} = \frac{4\pi I(\theta, \phi)}{P_{rad}}, \quad (2.5)$$

although it is typically expressed using a logarithmic scale $D(\theta, \phi)_{dBi} = 10 \log_{10} D(\theta, \phi)$.

The directivity does not include the radiation efficiency of the antenna. To encompass the directivity and the efficiency, the gain of an antenna is defined as the ratio of the radiated power density in a given direction from the antenna P_{avg} to the total antenna input power P_{in} . This definition slightly varies from the definition of the directivity because the considered total power is the power with which the antenna is fed, and not the total radiated power. In other words, the gain accounts for the efficiency of the antenna e_{rad} defined as:

$$P_{rad} = e_{rad} P_{in}. \quad (2.6)$$

The gain can hence be written as:

$$G(\theta, \phi) = e_{rad} D(\theta, \phi). \quad (2.7)$$

The gain is also typically expressed using a logarithmic scale as, where the term ‘dBi’ refers to an ideal isotropic antenna of gain $G_{iso}(\theta, \phi) = 1$:

$$G(\theta, \phi)_{dBi} = 10 \log_{10} G(\theta, \phi). \quad (2.8)$$

2.1 Antenna definition and figures of merit

Another definition of the gain, called realised gain, is defined as the gain G_{dBi} of Equation 2.8 but reduced by the losses due to the input impedance mismatch of the antenna [40]. The realised gain is important for small antennas where matching can be challenging.

The aperture efficiency of an antenna e_a describes how an antenna performs as a function of the dimensions of its aperture and is defined as:

$$e_a = \frac{A_{eff}}{A_{phys}}, \quad (2.9)$$

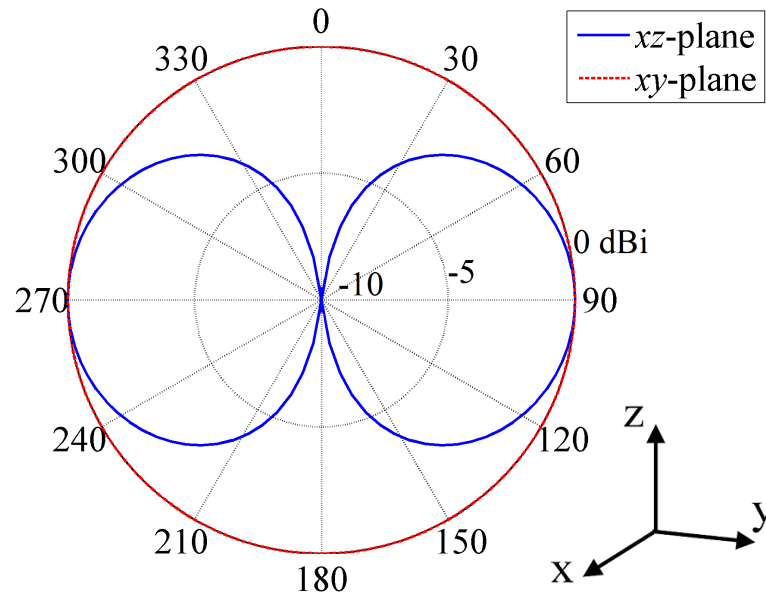
where $A_{eff} = \frac{\lambda^2}{4\pi}G$ and A_{phys} is the physical aperture of the antenna.

Antennas are often categorised in two main types with regard to their radiation patterns' shape:

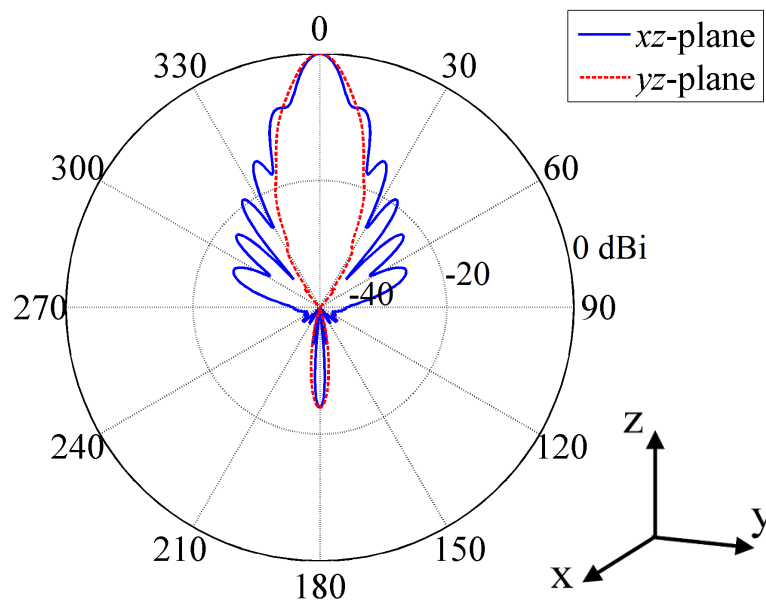
- (a) Omnidirectional antennas: These antennas have a substantially directionally-uniform radiation pattern. Applications such as broadcast usually require antennas with an omnidirectional pattern because the position of the receivers is not known. It is not possible to produce a perfect omnidirectional pattern, but the dipole antenna comes close enough for broadcast use. The pattern of an example dipole antenna is plotted in Figure 2.3(a).
- (b) Directional antennas: Those antennas typically radiate maximum power in one specific direction (sometimes more than one direction). Antennas with a directional radiation pattern are used in applications where the relative positions of the receivers are known so as to maximise energy efficiency and radio link quality. An example of a directional antenna is the horn antenna. The radiation pattern of a typical horn antenna is plotted in Figure 2.3(b), showing the primary lobe at boresight, and multiple secondary lobes.

The -3 dB beamwidth, or half-power beamwidth, is an often used figure of merit that quantifies the gain of an antenna in a plane containing the main beam. It is defined as the angle between the two directions for which the radiated power is half (or -3 dB in logarithmic scale) of maximum value of the main beam. For a directional antenna, the half power beamwidth gives a useful guide to the optimum location of receivers. Another aspect that affects the placement of the receivers is the polarisation of the signal.

2.1 Antenna definition and figures of merit



(a) Omnidirectional radiation pattern of a half-wave dipole antenna along the z -axis.



(b) Directional radiation pattern of a directional antenna radiation in the z direction.

Figure 2.3: Polar plots of two main types of radiation pattern: (a) omnidirectional and (b) directional pattern.

2.1.3 Polarisation

The polarisation of an antenna is defined according to the orientation and behaviour of the radiated E-field vector. The general expression of a plane wave travelling in the z -direction and capable of representing all possible polarisation states is:

$$\mathbf{E} = E_x \sin(\omega t - kz)\hat{\mathbf{x}} + E_y \sin(\omega t - kz + \varphi)\hat{\mathbf{y}}, \quad (2.10)$$

where E_x and E_y are the two orthogonal x and y electric field amplitudes, ω is the angular frequency, k is the propagation constant and φ is the phase difference between the two electric field components. There are three main types of polarisations: linear, elliptical and circular. Figure 2.4 shows examples of a linearly and a circularly polarised electromagnetic wave travelling in the z -direction.

For a linearly polarised plane wave, the two electric field components are in phase ($\varphi = 0$). In particular, for $E_x \neq 0$ and $E_y = 0$, the wave is linearly polarised in the x -direction. Similarly, for $E_x = 0$ and $E_y \neq 0$, the wave is linearly polarised in the y -direction. In the case of $E_x \neq 0$ and $E_y \neq 0$, the plane of polarisation is at angle ϕ with respect to the x -axis such as:

$$\phi = \tan^{-1} \frac{E_y}{E_x}. \quad (2.11)$$

Figure 2.4(a,b) illustrates an electromagnetic plane wave linearly polarised in the x -direction, where $E_x \neq 0$ and $E_y = 0$.

Circular polarisation is a special case of elliptical polarisation where $E_x = E_y$ and for which the two electric field components are out of phase by a quarter wave ($\varphi = \pi/2$). Figure 2.4(c,d) illustrates a right hand circularly polarised (RHCP) electromagnetic wave (from the source-perspective) which can be expressed as:

$$\mathbf{E}_{RHCP} = E_x \sin(\omega t - kz)\hat{\mathbf{x}} - E_y \cos(\omega t - kz)\hat{\mathbf{y}}. \quad (2.12)$$

The cross-polarisation is the polarisation orthogonal to the polarisation of reference. As antennas are intended to radiate energy in a particular polarisation, the cross-polarisation quantifies the amount of power radiated in the unwanted polarisation.

2.1 Antenna definition and figures of merit

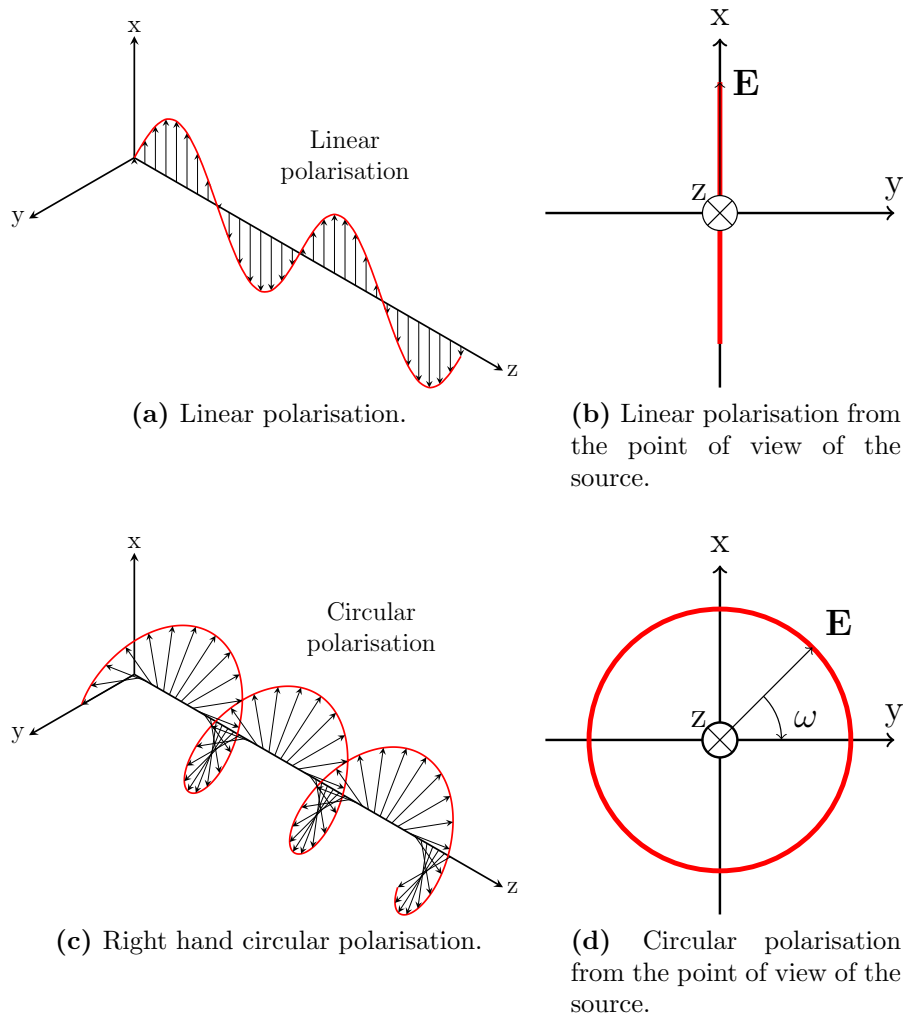


Figure 2.4: Linear and circular polarisation schemes for a plane wave travelling in the z -direction.

For a linearly-polarised antenna, such as the rectangular horn antenna to be presented in Section 2.2.3, the E- and H-plane are defined such that the E-plane is aligned with the polarisation axis. The H-plane is orthogonal to the E-plane as shown in Figure 2.5.

The polarisation is a key parameter because a difference in the polarisation scheme between the transmitter and the receiver introduces a polarisation loss factor [41]. For two linearly polarised antennas facing each other, the polarisation

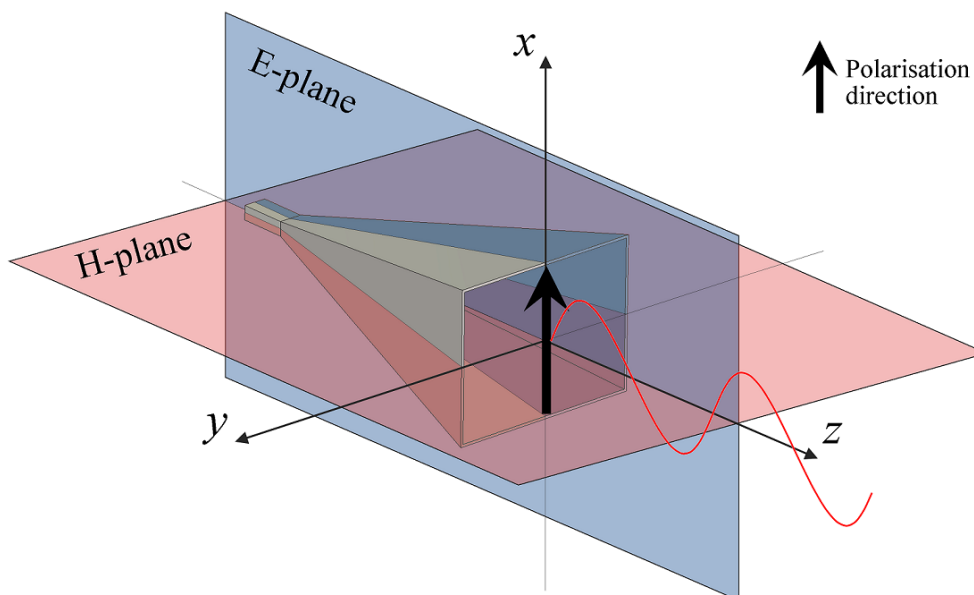


Figure 2.5: Illustration of the E- and H-plane definition for a linearly x -polarised horn antenna.

loss factor PLF_{dB} is expressed as:

$$\text{PLF}_{dB} = 10 \log_{10} (\cos^2 \psi), \quad (2.13)$$

where ψ is the angular mismatch between the two linear polarisation planes. For $\psi = 0^\circ$, $\text{PLF}_{dB} = 0 \text{ dB}$ so the loss due to the polarisation mismatch is nil. For $\psi = 90^\circ$, the two polarisations are orthogonal to each other so $\text{PLF}_{dB} = -\infty \text{ dB}$, resulting in zero received power. This illustrates the necessity to take the polarisation scheme into account during the design of a radio link. In particular, linear polarisation schemes should usually only be used when the relative position of the receiver is fixed or slowly changing.

2.1.4 Impedance bandwidth

The bandwidth is a figure of merit describing the domain of frequency over which an antenna performs within specified requirements. The fractional bandwidth, in percent, is the most commonly used definition and is defined as:

$$\text{BW}(\%) = 200 \times \frac{f_H - f_L}{f_H + f_L}, \quad (2.14)$$

2.1 Antenna definition and figures of merit

where f_L is the lower and f_H the upper limit of the frequency of operation.

The impedance bandwidth is defined as the frequency band over which the S_{11} value is lower than -10 dB, as shown in Figure 2.6. This particular S_{11} value is equal to a reflected power of 10% at the antenna input port.

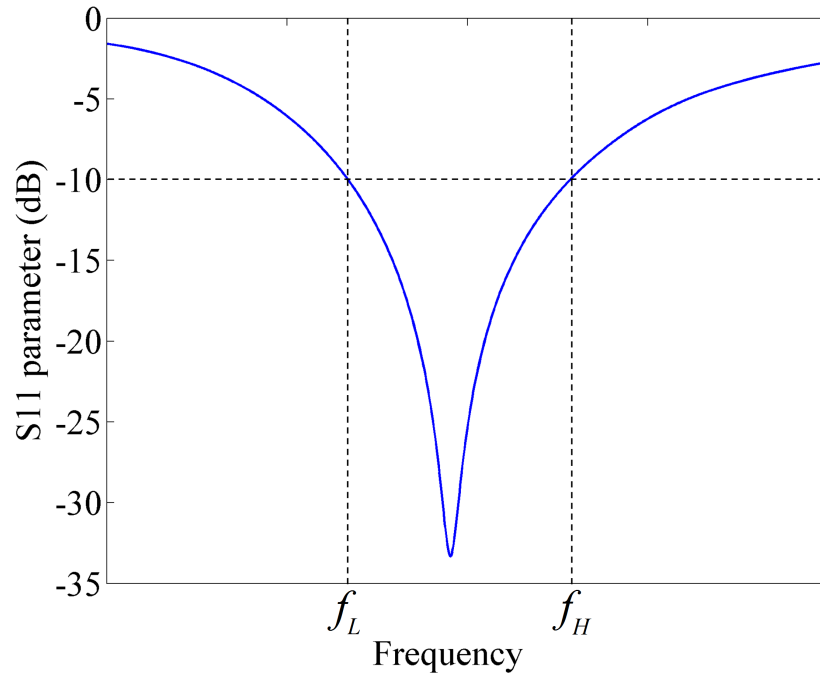


Figure 2.6: Plot of an example S_{11} parameter showing the bandwidth defined between f_L and f_H for $S_{11} < -10$ dB for a notional antenna.

The Voltage Standing Wave Ratio (VSWR) is another commonly used figure of merit, and relates to the S_{11} parameter and to the reflection coefficient Γ such that:

$$\text{VSWR} = \frac{1 + |\Gamma|}{1 - |\Gamma|}, \quad (2.15)$$

where Γ is the reflection coefficient. The scattering parameter S_{11} is related to the reflection coefficient by $20 \log_{10} |\Gamma|$. A VSWR of 1.5 is used as a typical limiting value of a good design and corresponds to an S_{11} parameter of about -14 dB or a reflected power of 4%. This is more stringent than the previous criterion of $S_{11} < -10$ dB.

2.1.5 Link budget

The link budget is a calculation used to evaluate the quality of a radio link. The Friis equation gives a useful description in a free space loss radio link [42]. This equation takes into account the gain of the transmitting (Tx) and receiving (Rx) antennas, the frequency at which the signal is transmitted and the distance between the transmitter and the receiver, and is expressed as:

$$P_{Rx,dB} = P_{Tx,dB} + G_{Tx,dBi} + G_{Rx,dBi} + 20 \log_{10} \left(\frac{\lambda}{4\pi d} \right), \quad (2.16)$$

where $P_{Rx,dB}$ is the received power in dB, $P_{Tx,dB}$ is the transmitted power in dB, $G_{Tx,dBi}$ is the gain in dBi of the transmitting antenna, $G_{Rx,dBi}$ is the gain in dBi of the receiving antenna, λ is the wavelength in meters, d is the distance between the two antennas in meters. The last term of Equation 2.16 is called the free space path loss (FSPL) and accounts for the power loss due to the propagation of a plane wave in vacuum. Figure 2.7 illustrates the concept of the Friis equation.

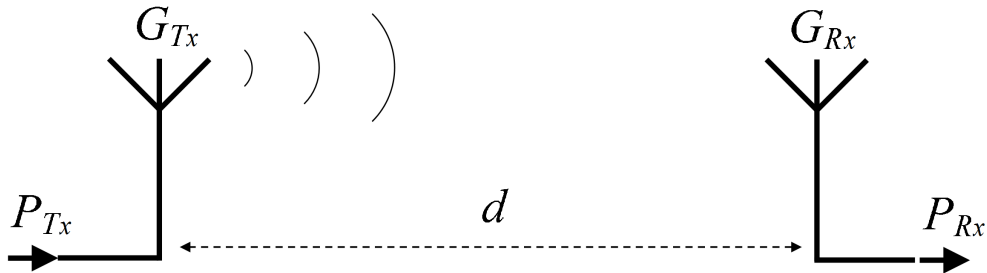


Figure 2.7: Schematic of the line of sight point to point transmission link modelled by the Friis equation where P_{Tx} is the transmitted power, G_{Tx} is the gain of the transmitting antenna, G_{Rx} is the gain of the receiving antenna, and P_{Rx} is the received power.

Equation 2.16 can be rewritten:

$$P_{Rx,dB} = \text{EIRP}_{dB} - \text{FSPL}_{dB} + G_{Rx,dBi} - \gamma_{atm,dB}, \quad (2.17)$$

where $\gamma_{atm,dB}$ is the atmospheric attenuation and EIRP_{dB} is the equivalent isotropic radiated power defined as

$$\text{EIRP}_{dB} = G_{Tx,dBi} + P_{Tx,dBi}. \quad (2.18)$$

Full link budgets are commonly expressed in terms of carrier-to-noise density ratio $\left(\frac{C}{N_0}\right)_{dB}$. The carrier signal power C corresponding to the received power $P_{Rx,dB}$ defined in Equation 2.17, and N_0 is the noise spectral density such as:

$$N = N_0B = k_BTB, \quad (2.19)$$

where N is the thermal noise power, B is the bandwidth, T is the antenna temperature and k_B is Boltzmann's constant.

Hence the carrier-to-noise density ratio is written as:

$$\left(\frac{C}{N_0}\right)_{dB} = \text{EIRP}_{dB} - \text{FSPL}_{dB} + G_{Rx,dBi} - 10 \log_{10}(k_BTB) - \gamma_{atm,dB}, \quad (2.20)$$

and the carrier-to-noise ratio is:

$$\left(\frac{C}{N}\right)_{dB} = \text{EIRP}_{dB} - \text{FSPL}_{dB} + G_{Rx,dBi} - 10 \log_{10}(k_BTB) - \gamma_{atm,dB}. \quad (2.21)$$

The energy per bit to noise power spectral density ratio $\left(\frac{E_b}{N_0}\right)_{dB}$ is related to the carrier-to-noise density ratio such as:

$$\left(\frac{E_b}{N_0}\right)_{dB} = \left(\frac{C}{N_0}\right)_{dB} - 10 \log_{10}(R_b), \quad (2.22)$$

where R_b is the information bit rate.

The energy per bit to noise power spectral density ratio is defined for a reference bandwidth of 1 Hz, and is a function of the modulation scheme and the required signal quality in terms of bit error rate.

2.2 Typical antennas

Many types of antenna exist for which exhaustive descriptions and design rules can be found in antenna handbooks [41, 43]. Despite this, antennas can be broadly categorised according to their operating principles. For the sake of illustration, three widely used antennas, dipole, patch, and horn, are briefly presented in this Section in order to provide an insight into the performance and behaviour of typical antennas.

2.2.1 Dipole antenna

A dipole antenna consists of two separate straight wires, fed by an alternating radio wave generator as illustrated in Figure 2.8. The length of a resonant dipole antenna is a fraction or a multiple of the wavelength of operation (0.25λ , 0.5λ , 1.0λ , ...) so as to allow a standing wave to occur. The far-field radiation pattern of a half-wave dipole has a typical toroid ('doughnut') shape with characteristic nulls along the length of the antenna. A half-wave dipole antenna made of perfectly conducting material has a gain of 2.15 dBi.

Another alternative definition of the gain is based on the gain with respect to a half-wave dipole (2.15 dBi), instead of an isotropic antenna (0 dBi), and is expressed as $G_{dBd} = G_{dBi} - 2.15$.

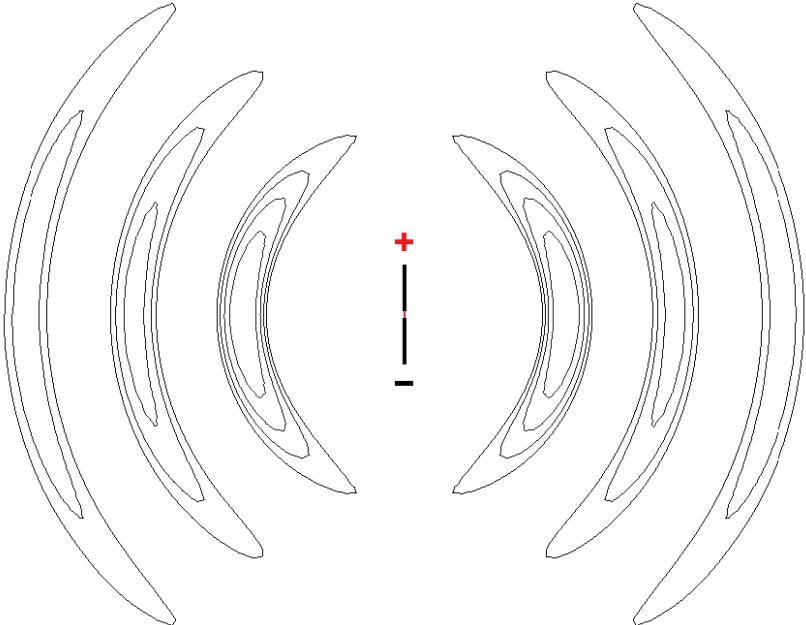
2.2.2 Patch antenna

A patch antenna is a type of printed antenna which consists of a metallic patch separated from a ground plane by a dielectric material. This type of antenna is popular because of its low fabrication cost and its low profile. Figure 2.9 shows a linearly polarised rectangular patch antenna operating at 10 GHz, and the 3D far-field radiation pattern in transparency with a maximum gain of 6.95 dBi.

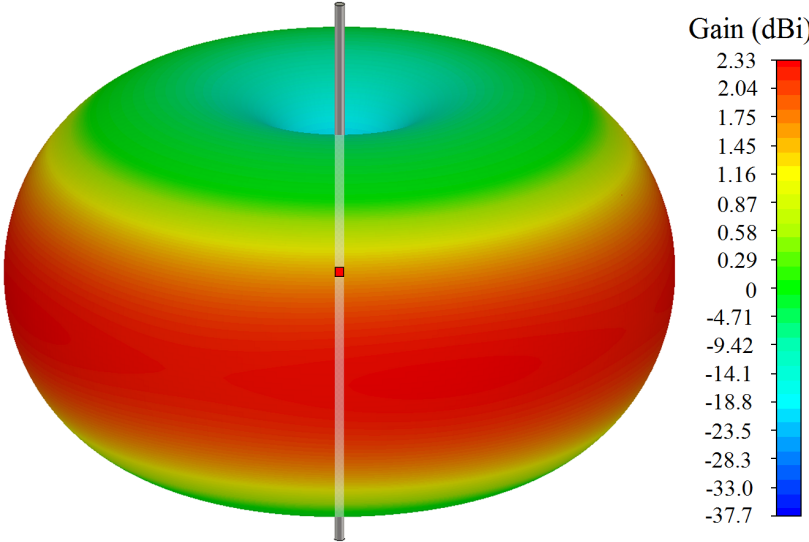
The example antenna has an impedance bandwidth ($S_{11} < -10$ dB) of 184 MHz (1.8%). The impedance matching for a patch antenna is usually straightforward because it can be achieved directly on the printed board. In this example, an inset adjusts the input impedance of the antenna to the standard $50\ \Omega$ without additional circuitry.

2.2.3 Horn antenna

A horn antenna is a type of antenna made of a tapered open-end waveguide, allowing a continuous and smooth transition between a guided wave and a free space radiating wave. Horn antennas usually have a rectangular or a circular aperture, corresponding to a rectangular or circular waveguide feed. They are widely used for their high directivity, low return loss, large bandwidth and robustness. However, the bulky shape of this antenna makes it unsuitable for applications



(a) Contour plot of the electric field distribution around a half-wave dipole at a moment in time.



(b) 3D far-field power radiation pattern with dipole antenna shown in transparency.

Figure 2.8: Illustration of (a) a half-wave dipole showing the electric field distribution, and (b) the 3D toroid-shaped far-field radiation pattern.

requiring a low profile. Like other aperture antennas, the gain of a horn antenna

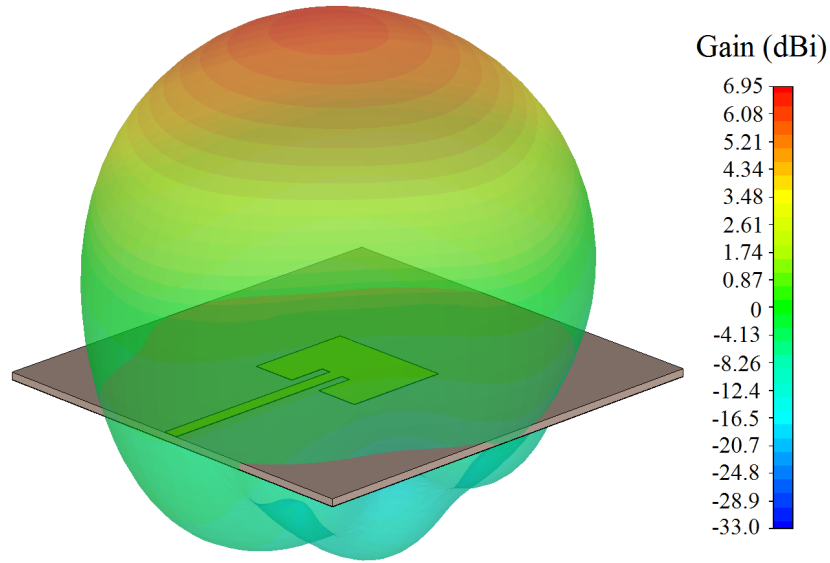


Figure 2.9: Illustration of rectangular patch antenna with an inset for impedance matching, operating at 10 GHz, and the 3D far-field radiation pattern in transparency.

is expressed as:

$$G_{dBi} = 10 \log_{10} \frac{4\pi A_{phys}}{\lambda^2} e_a, \quad (2.23)$$

where the aperture efficiency e_a is about 0.6 for an optimum horn [37]. Figure 2.10 shows a typical 23 dBi rectangular horn antenna ($69.6 \times 38.6 \times 29.5 \text{ mm}^3$) and the 3D far-field radiation pattern. It is fed by a waveguide and operates between 50 and 75 GHz.

Low profile alternatives like arrays of patch antennas can provide high gain but are usually inefficient at millimetre-wave frequencies due to large feeding networks.

As can be appreciated, there are many antenna designs and it would not be appropriate to review them all. Next we consider the antennas upon which the Bull's eye antenna is based.

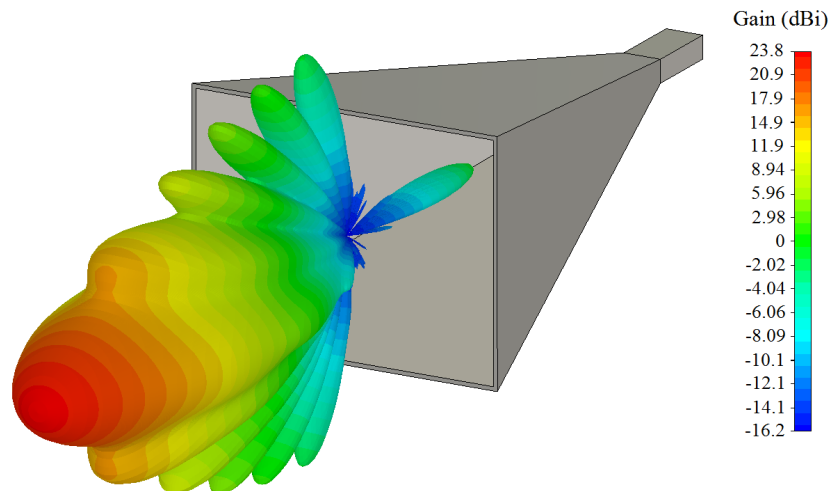


Figure 2.10: Illustration of a 23 dBi rectangular horn antenna with the 3D far-field radiation pattern at 60 GHz.

2.3 Bull's eye antenna concept

2.3.1 Leaky wave antenna (LWA)

A leaky wave antenna (LWA) is a type of planar, travelling wave antenna for which a surface wave, generated by an appropriate feed, couples to free space [44]. LWAs are popular for microwave and millimetre-wave applications because they are low profile and can provide high directivity using straightforward manufacturing processes [45]. The complex angular wavenumber of the surface wave travelling along the planar structure is defined as $k = \beta' - j\beta''$ and the free-space angular wavenumber is k_0 . LWAs can be unidirectional or bidirectional, depending on whether the source generating the surface wave is at one extremity or at the centre of the antenna. Additionally, LWAs can be classified into two main categories: uniform and periodic LWAs.

- A uniform LWA is a homogeneous structure radiating continuously along the direction of propagation. For this structure, the travelling wave is fast compared to free space ($0 < \text{Re}(k) < k_0$) because the wave leaks from a hollow waveguide. A typical uniform LWA is a rectangular waveguide with a continuous slot as shown in Figure 2.11 [46].
- A periodic LWA is that for which the radiating surface is periodically modulated. Consequently, the supported surface wave is slow compared to free

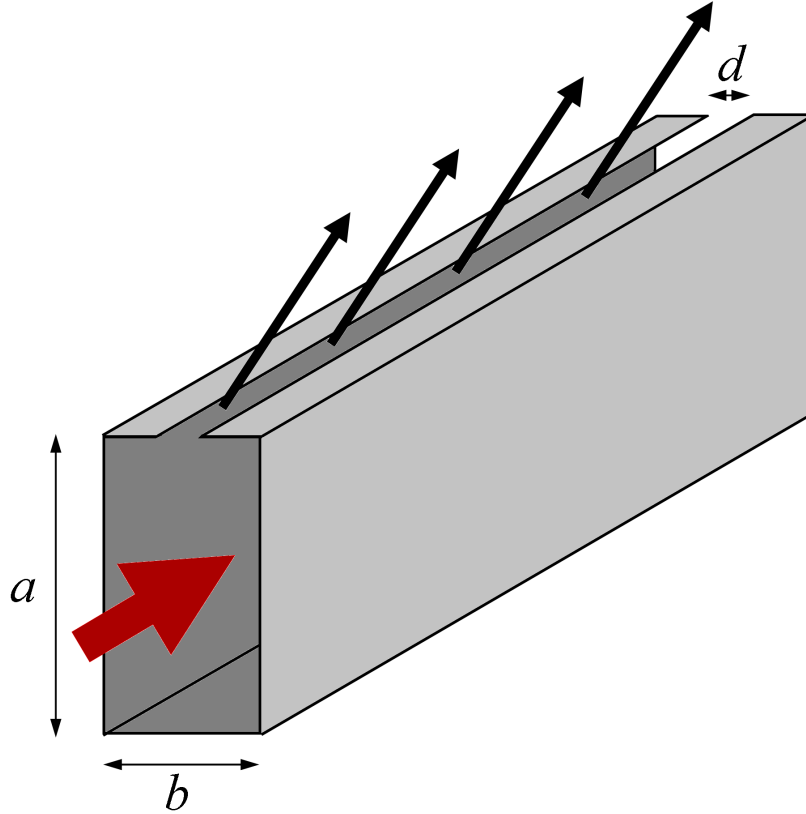


Figure 2.11: Illustration of a uniform LWA made of a rectangular waveguide with a continuous slot, with incoming travelling wave in the waveguide (large red arrow) and leaky wave (black arrows).

space ($Re(k) > k_0$). A common periodic LWA is a printed, metallic-strip, grating pattern fed by a surface wave as shown in Figure 2.12 [47, 48].

Periodic LWAs based on a subwavelength aperture surrounded by corrugations have been reported to operate in the optical regime [49, 50, 51]. At those frequencies, leaky wave theory does not fully describe the radiation phenomenon and the surface wave is referred to as a surface plasmon polariton (SSP). SSP can be described the couple state between a surface plasmon (charge oscillations) and a photon.

The same phenomenon was scaled to the microwave regime and used for radio transmission. In this frequency domain, LWAs can provide a trade off in terms of size, gain and efficiency that is favourable compared to horn antennas and phased arrays. For example, CubeSats have limited power and payload, making LWAs attractive for this application. A 23 dBi rectangular horn antenna (Custom

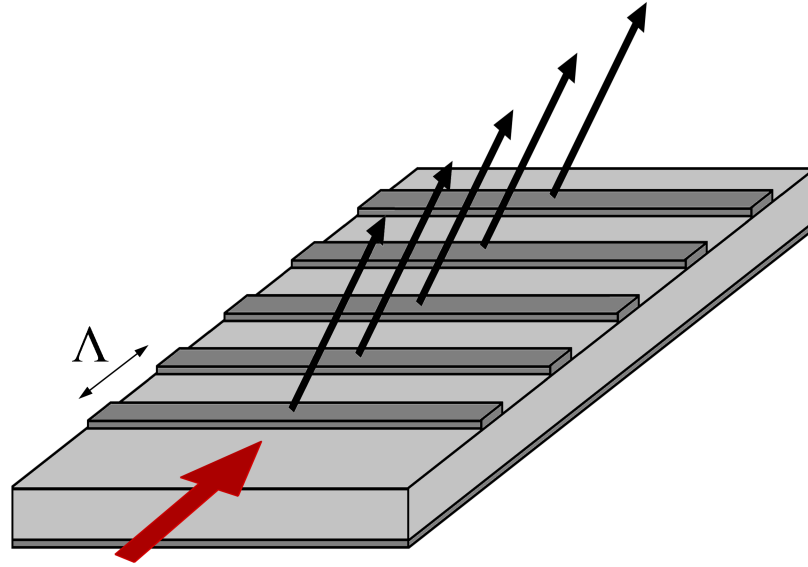


Figure 2.12: Illustration of a periodic LWA made of a printed, metallic strip, grating-pattern of period Λ , with incoming travelling surface wave (large red arrow) and leaky wave (black arrows).

Microwave, Inc. model HO15R) has a 70 mm length and a $36 \times 28 \text{ mm}^2$ aperture, which takes up to 10% of the bulk volume of a 1U payload. On the other hand, the low profile of a LWA allows straightforward integration on the face of a CubeSat. Figure 2.13 shows a photograph of a 3.2 mm thick periodic LWAs’ structure and a horn antenna both operating at 60 GHz illustrating the volume difference.

2.3.2 Bull’s eye antenna description

A Bull’s eye antenna is a bidirectional, periodic LWA which takes its name from the visual aspect of the design, composed of a set of circular corrugations surrounding the central feed [52], as seen in Figure 2.13. The term ‘Bull’s eye’ antenna has also been used for printed periodic leaky wave antennas [53, 54]. In this Thesis, only corrugated Bull’s eye antennas are investigated, for which the whole active surface is made of conducting material such as described by Beruete *et al.* [52]. This is for convenience in manufacture and fitting to materials requirements of space missions where dielectrics can be problematic. To illustrate the difference between a printed and a corrugated Bull’s eye antenna, the two different structures are shown in Figure 2.14.

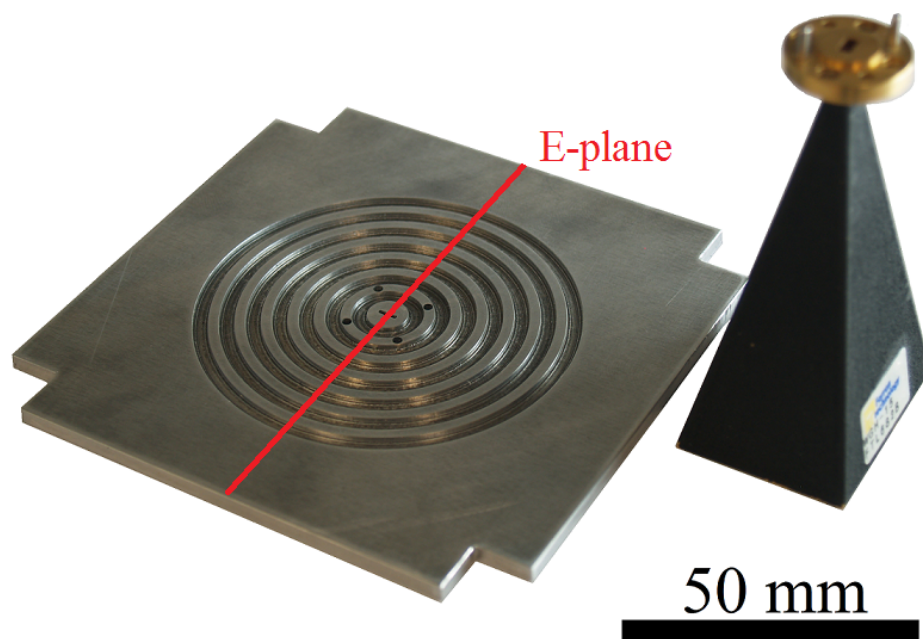
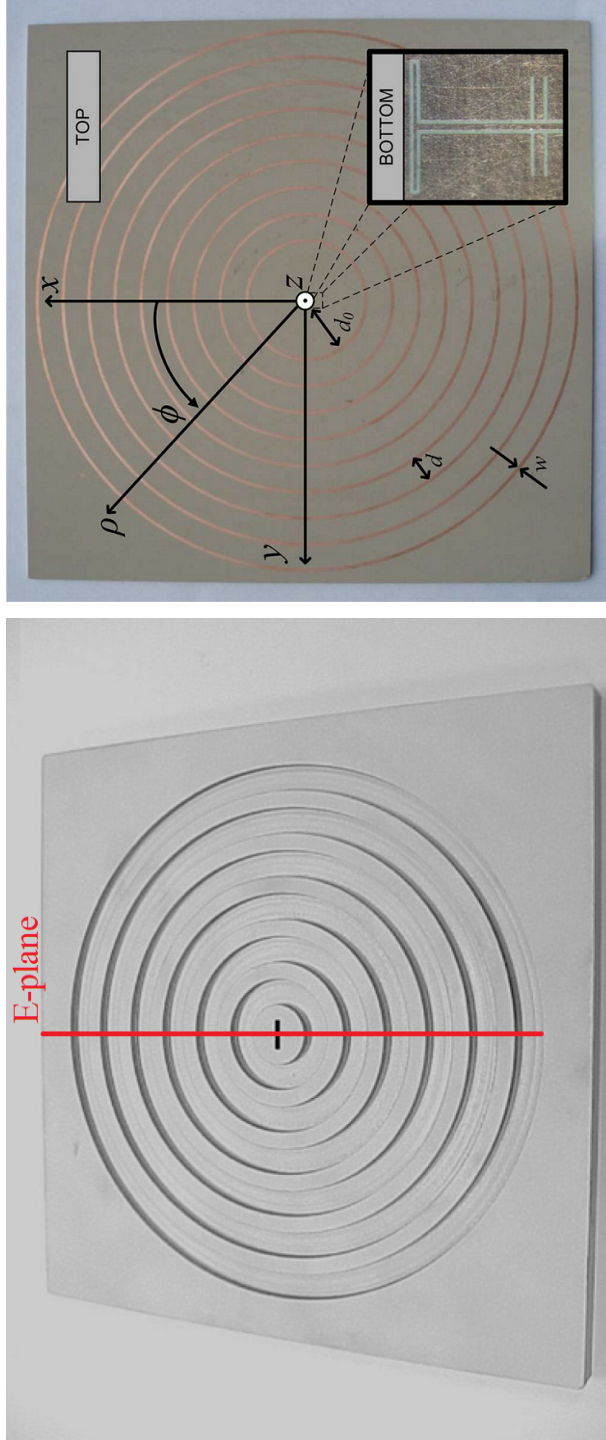


Figure 2.13: Volume comparison between a standard Bull's eye antenna and rectangular horn antenna both operating at 60 GHz. The low profile of the Bull's eye antenna allows straightforward integration on the face of a CubeSat.



(a) Corrugated Bull's eye antenna ©2005 IEEE.

(b) Printed Bull's eye antenna ©2011 IEEE.

Figure 2.14: Photographs of the two types of Bull's eye antenna: a corrugated Bull's eye antenna (from [52]) and a printed Bull's eye antenna (from [54]).

A corrugated Bull's eye antenna is made of a rectangular subwavelength aperture, placed at the centre of the antenna, fed from the rear. This aperture launches an electromagnetic surface wave (slow wave) travelling at the interface between the conductor material of the antenna and free space. The dimensions of the subwavelength aperture (depth, width and length) control the resonant frequency, bandwidth and return loss of the antenna. The feed is typically a rectangular waveguide carrying a linearly polarized TE_{10} mode, making the antenna linearly polarised. The E-plane is orthogonal to the surface of the antenna, and coincides with the short side of the subwavelength aperture. The H-plane is orthogonal to the surface of the antenna and coincides with the long length of the subwavelength aperture.

Looking now in detail at its operation, let us assume a 2D structure of spatial period Λ along the z axis, made of conductive material as defined in Figure 2.15. At the surface of the structure, an electromagnetic surface wave travels along the z axis and its electric field $E(x, z)$ can be written using the Floquet theorem [55]:

$$E(x, z + \Lambda) = \exp[-jk_z\Lambda] E(x, z), \quad (2.24)$$

where k_z is the angular wavenumber of the surface wave.

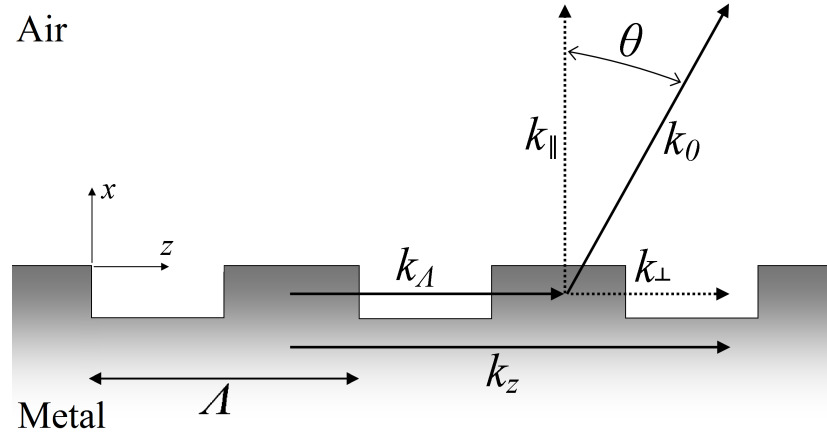


Figure 2.15: Illustration of the coupling mechanism between a surface wave of angular wavenumber k_z and the free-space of wavenumber k_0 at an angle θ through a grating of period Λ . For spatial harmonic $n = -1$, $k_A = \frac{2\pi}{\Lambda}$.

The solutions satisfying equation 2.24 can be written as:

$$E(x, z) = \exp[-jk_z z] P(x, z), \quad (2.25)$$

where P is a periodic function defined as $P(x, z) = P(x, z + \Lambda)$. Because P is periodic, the corresponding Fourier series can be written as:

$$P(x, z) = \sum_{n=-\infty}^{+\infty} a_n(x, y) \exp \left[-j \frac{2\pi n}{\Lambda} z \right], \quad (2.26)$$

where a_n is the complex Fourier coefficient depending on the electric field variations, the excitation and the structure geometry.

The electric field can then be cast by substituting Equation 2.26 in 2.25:

$$E(x, z) = \sum_{n=-\infty}^{+\infty} a_n(x, y) \exp [-jk_{zn}z], \quad (2.27)$$

where

$$k_{zn} = k_z + \frac{2\pi}{\Lambda} n, \quad (2.28)$$

is the z component of the n^{th} harmonic of the free-space wavenumber. Note that also $k_{zn} = k_0 \sin \theta$, where θ is the angle at which the leaky wave best couples to the free-space. This equation is sometimes referred to as the periodic grating equation. It illustrates the matching condition necessary for the surface wave, of wavenumber k_z , to couple with free-space, of wavenumber k_0 . Because $n = -1$ is usually the easiest non-zero harmonic to couple with, the periodic grating equation simplified to:

$$k_z = k_0 \sin \theta + \frac{2\pi}{\Lambda}. \quad (2.29)$$

Equation 2.29 represents a momentum matching criterion that governs the local coupling mechanism between a surface wave of wavenumber k_z and free-space of wavenumber k_0 at an angle θ through a grating of period Λ . The relationship is depicted graphically in Figure 2.15.

2.3.3 Evolution and latest advances

Over the last decade, 17 journal papers and conference proceedings were published on Bull's eye antennas¹. A paper published in 2004 by Beruete *et al.* illustrates

¹Search on IEEE Xplore following the terms 'Bull's eye antenna'

the leaky wave phenomenon at 13.5 GHz with a structure made of linear corrugations on each side of a subwavelength aperture [56]. This is a simplified form of a Bull's eye antenna.

The first actual Bull's eye antenna operating in the microwave band was named and presented in 2005 [52]. This antenna was designed to operate at 16 GHz and provided a maximum gain of 18 dBi, validating the use of the Bull's eye antenna design with surface waves.

In 2006, a subwavelength aperture used for the Bull's eye antenna was investigated and it was shown that it could operate as a dual-band antenna (13.0 and 16.5 GHz) due to the nature of the resonant subwavelength aperture. A version of a subwavelength aperture with linear corrugations was presented by Diaz *et al.* [57].

In 2009, a Bull's eye antenna fed with a patch antenna operating at 12.8 GHz was presented by Huang *et al.* [58]. This antenna reached a maximum gain of 21.8 dBi with five corrugations and showed that alternative feeding structures can be used.

In 2011, the design of a spiral leaky wave antenna operating at 13 and 18 GHz and providing circular polarisation (right or left handed) was presented [59].

In 2013, a Bull's eye antenna intended to serve as a terahertz detector operating around 0.56 THz was presented [60]. In particular, two types of corrugation profiles were investigated: triangular corrugations provided a maximum gain of 15.9 dBi while the square corrugations provided a maximum gain of 16.5 dBi.

More recently, in 2014 and 2015, a Bull's eye antenna with sinusoidal grating profile and operating at 77 GHz was investigated [61, 62, 63]. This particular design provided an improvement in terms of peak gain, reaching 29 dBi for 20 sinusoidal periods.

The work in this Thesis has taken place alongside other independent development in the field. During my PhD, started in October 2012, I have published two journal papers: the first presents the design and operation of a 60 GHz Bull's eye antenna for CubeSat application [64], and the second introduces beam deflection capabilities [65]. These papers are highlighted in red in the time-line of Figure 2.16. A third journal paper presenting the design of a Bull's eye antenna capable of generating two or four orbital angular momentum modes, and the associated receiving scheme, was accepted for publication in the October 2016 special issue

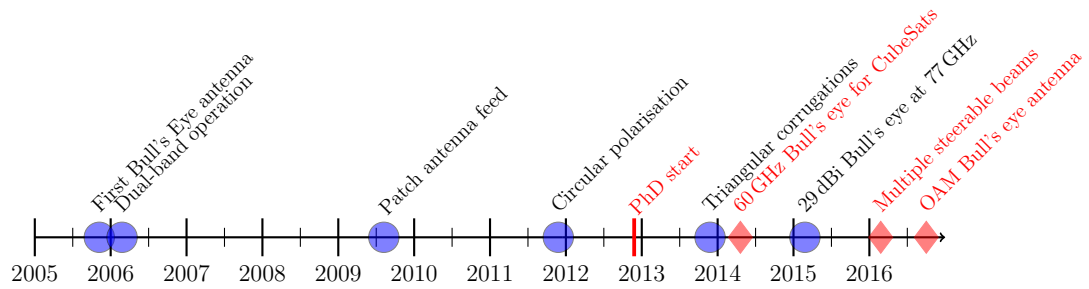


Figure 2.16: Time-line of Bull’s eye antenna main advances for microwave, millimetre-wave and terahertz regimes. My contributions to the field since the start of my PhD (October 2012) are listed in red diamond markers.

on “Millimetre Wave Systems, Circuits and Antenna Integration Challenges for Broadband Everywhere”.

2.4 Chapter summary

This Chapter provided the key figures of merit of antennas that will be used to evaluate the performance of the antennas presented in this Thesis. Three common types of antenna were then presented, namely the dipole, patch and horn antenna, to provide an overview of different radiation mechanism and typical performance figures. The concept of leaky wave antennas (LWAs) and the design of a Bull’s eye antenna structure was then introduced. The Bull’s eye antenna is a bidirectional periodic LWA, composed of a central subwavelength aperture launching a surface wave travelling at the interface between a conductor and free space. The addition of circular corrugations around the aperture increases the wavenumber of the surface wave by $2\pi n/\lambda$, where n is the diffraction harmonic, and allows the surface wave to couple with free space at an angle θ . Subsequently, a chronological list of papers related to the latest advance in the design of Bull’s eye antennas was provided, including my contributions. The next Chapter describes the methods used to develop and test designs.

Chapter 3

Methods

This Chapter presents an overview of the simulation tools, manufacturing processes and measurements' methods that were used in this Thesis. In the first Section, the simulation methods and software tools used to design the Bull's eye antennas are presented, including the finite-difference time-domain (FDTD), finite integration technique (FIT), and the rigorous coupled-wave analysis (RCWA) methods. The fabrication techniques are presented in the second Section. This includes a discussion of the choice of the material for the Bull's eye antenna, the presentation of the machining techniques and the photolithography process. The description of the measurement tools is included in the third Section, focusing on the V-band test bench and the gain transfer method for measuring antenna gain.

3.1 Simulation tools

Electromagnetic solver tools are useful for predicting the performance of an antenna. It is important to understand the advantages and drawbacks of the different available methods. For this Thesis, they include the finite-difference time-domain (FDTD) method, and the finite integration technique (FIT) method implemented in CST Microwave Studio (CST MWS). The rigorous coupled-wave analysis (RCWA) method is also used to model a 2D periodic structure.

3.1.1 Finite-difference time-domain (FDTD) method

The finite-difference time-domain (FDTD) method is a numerical method for solving Maxwell's curl equations in the time domain [66]. This method is widely used in the electromagnetic engineering community because it is straightforward to understand and to implement in its basic form, yet provides powerful predictive capability due to the minimal use of assumptions. Other advantages include computing the evolution of the E- and H-fields in the computational domain which provides a dynamic visualisation that fosters physical insight, and computing results over a large band of frequency when using special types of excitation signal (e.g. modulated Gaussian pulse). It is usually preferred to frequency-based method for structures that operate over a broadband. The method is based on the discretisation of the space and time domain via an elementary meshing scheme called the Yee lattice [67]. This particular lattice determines a specific convention for the spatial distribution of the electric and magnetic field components, as illustrated in Figure 3.1:

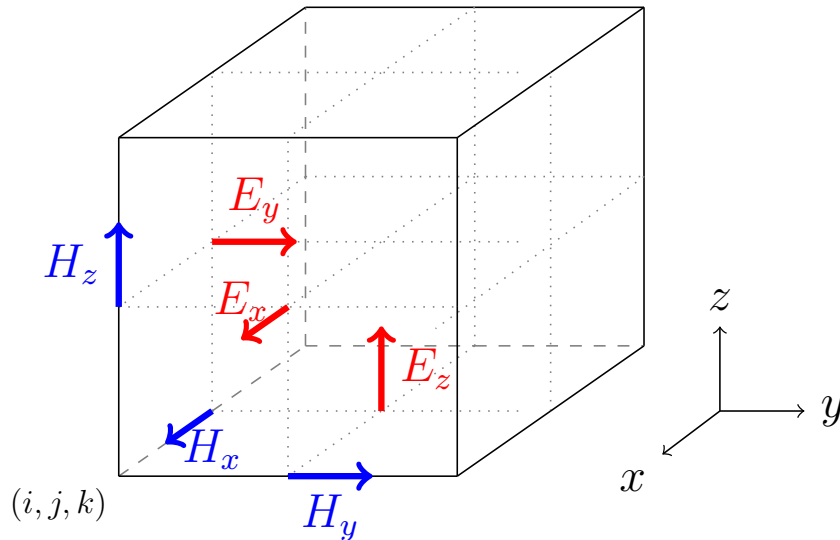


Figure 3.1: Illustration of a 3D Yee lattice. The arrows represent the quantities associated with the (i, j, k) cell.

Each of the electric (magnetic) field components are calculated in the space domain at a time $n + 1/2$ (n) and, then updated at intervals of Δt , the time-step. To do so, the differential form of the Maxwell-Ampere equation is rewritten as

[68]:

$$\nabla \times \mathbf{H} = \varepsilon \frac{\partial \mathbf{E}}{\partial t} + \mathbf{J}, \quad (3.1)$$

where $\mathbf{H} = \mathbf{B}/\mu$, \mathbf{B} is the magnetic field, μ is the permeability, $\mathbf{J} = \sigma \mathbf{E} + \mathbf{J}_{source}$ is the electric current density, and \mathbf{E} is electric field, where σ is the electrical conductivity and \mathbf{J}_{source} is the electric current density of an independence source. For the x -component of the electric field, the following scalar equation can be written:

$$\frac{\partial E_x}{\partial t} = \frac{1}{\varepsilon} \left[\frac{\partial H_z}{\partial y} - \frac{\partial H_y}{\partial z} - J_x \right], \quad (3.2)$$

where H_z is the z -component of the magnetic field, H_y is the y -component of the magnetic field and J_x is the x -component of the current density. Equation 3.2 can then be converted to a discrete equivalent with a central difference for the time and space derivatives, choosing n as the index of the current time, and i , j and k the indexes of the respective current spatial coordinates, such as:

$$\frac{E_x|_{i,j+1/2,k+1/2}^{n+1/2} - E_x|_{i,j+1/2,k+1/2}^{n-1/2}}{\Delta t} = \frac{1}{\varepsilon_{i,j+1/2,k+1/2}} \left[\frac{H_z|_{i,j+1,k+1/2}^n - H_z|_{i,j,k+1/2}^n}{\Delta y} - \frac{H_y|_{i,j+1/2,k+1}^n - H_y|_{i,j+1/2,k}^n}{\Delta z} - J_x|_{i,j+1/2,k+1/2}^n \right], \quad (3.3)$$

where the current density $J_x = J_{source_x} + \sigma E_x$ at coordinates $(i, j+1/2, k+1/2)$ can be written as:

$$J_x|_{i,j+1/2,k+1/2}^n = J_{source_x}|_{i,j+1/2,k+1/2}^n + \sigma_{i,j+1/2,k+1/2} E_x|_{i,j+1/2,k+1/2}^n. \quad (3.4)$$

A central average gives $E_x|_{i,j+1/2,k+1/2}^n$ as:

$$E_x|_{i,j+1/2,k+1/2}^n = \frac{E_x|_{i,j+1/2,k+1/2}^{n+1/2} + E_x|_{i,j+1/2,k+1/2}^{n-1/2}}{2}. \quad (3.5)$$

Reorganising Equation 3.3 with Equations 3.5 and 3.4:

$$E_x|_{i,j+1/2,k+1/2}^{n+1/2} = \left(\frac{1 - \frac{\sigma_{i,j+1/2,k+1/2}\Delta t}{2\varepsilon_{i,j+1/2,k+1/2}}}{1 + \frac{\sigma_{i,j+1/2,k+1/2}\Delta t}{2\varepsilon_{i,j+1/2,k+1/2}}} \right) E_x|_{i,j+1/2,k+1/2}^{n-1/2} + \left(\frac{\frac{\Delta t}{\varepsilon_{i,j+1/2,k+1/2}}}{1 + \frac{\sigma_{i,j+1/2,k+1/2}\Delta t}{2\varepsilon_{i,j+1/2,k+1/2}}} \right) \cdot \left[\frac{H_z|_{i,j+1,k+1/2}^n - H_z|_{i,j,k+1/2}^n}{\Delta y} - \frac{H_y|_{i,j+1/2,k+1}^n - H_y|_{i,j+1/2,k}^n}{\Delta z} - J_{source_x}|_{i,j+1/2,k+1/2}^n \right]. \quad (3.6)$$

Equation 3.6 provides value the E_x component at the point $(i, j + 1/2, k + 1/2)$ and at the time $n + 1/2$ with respect to previously calculated values and initial conditions. The calculation of all the other components of the electric field and the magnetic field can be carried out in the same way to fully characterise the domain.

For the stability of the simulation, the space and time steps need to be carefully chosen. The Courant-Friedrichs-Lewy condition suggests that the time-step Δt is chosen such as:

$$\Delta t \leq \frac{1}{c\sqrt{\frac{1}{\Delta x^2} + \frac{1}{\Delta y^2} + \frac{1}{\Delta z^2}}}, \quad (3.7)$$

where Δx , Δy and Δz are the spatial dimensions of the unit cells.

CST Microwave Studio (CST MWS) is a commercial solver tool that has been used to simulate the performance of all the prototypes presented in this Thesis. Its transient solver is based on a method similar to the FDTD method called finite integration technique (FIT). It is based on the discretisation of the space domain in unit cells for which the voltage \hat{e} along one edge of a cell facet, and the magnetic flux \hat{b} through a cell facet, are calculated for each cell. A detailed derivation of the method is provided by Clemens *et al.* [69].

CST MWS has a graphical interface that allows a straightforward visualisation of the antenna models, which are created by using specific dielectric or conducting materials, and defining sources, boundary and symmetry conditions, and probes for the analysis of the simulations results. Electric and magnetic symmetry conditions are useful for dividing the simulation domain and subsequently decreasing the simulation time and the amount of computational resource required. For example, a horn antenna can benefit from the symmetry conditions because this structure is symmetric in the xz - and yz -planes, as shown in Figure 3.2. In Figure

3.2(a), the electric field distribution on the aperture plane shows that the electric field has no component tangential to the xz -plane. Thus, an electric symmetry condition can be defined to halve the simulation domain. Similarly in Figure 3.2(b), the magnetic field distribution on the aperture plane shows that the magnetic field has no component tangential to the yz -plane. Hence, a magnetic symmetry condition can be defined to halve the simulation domain again. As a result, the simulation domain can be quartered for this structure, decreasing the simulation time from 180 to 50 sec, for a horn antenna operating at 12 GHz.

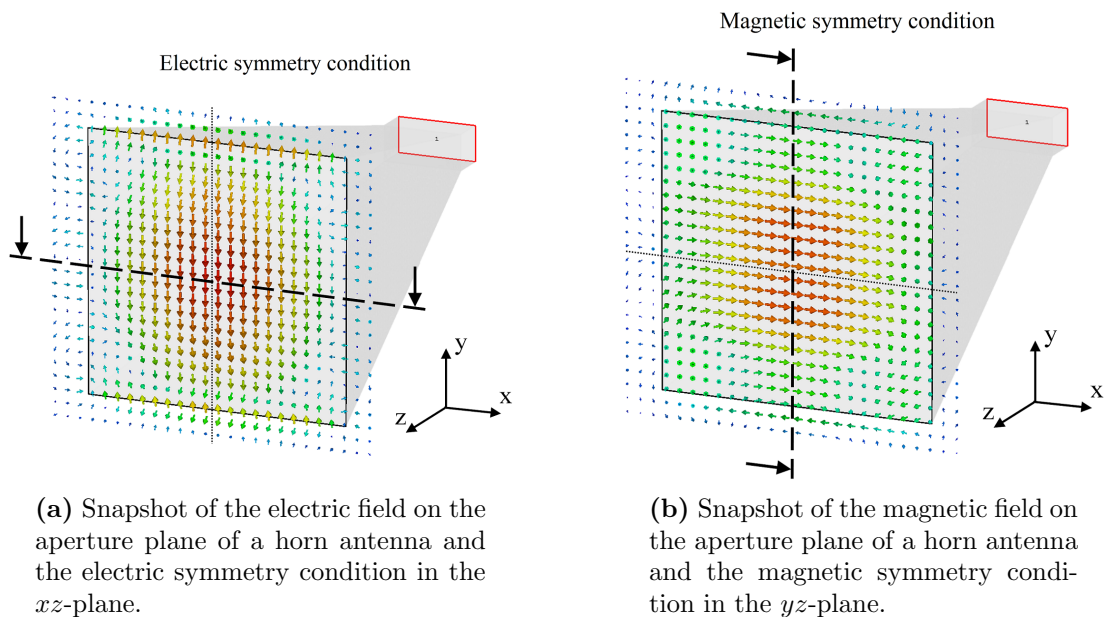


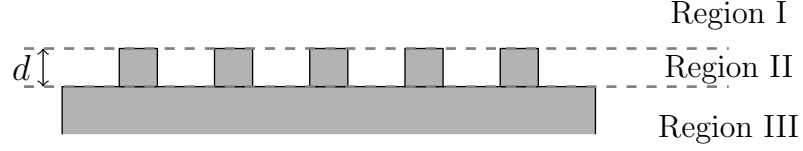
Figure 3.2: Illustration of the electric and magnetic symmetry conditions for an analysis of a horn antenna in CST MWS.

SolidWorks, developed by Dassault Systèmes, was used to model complex structures and exported as $.stl$ files. These types of files can easily be imported into CST MWS as components to be simulated.

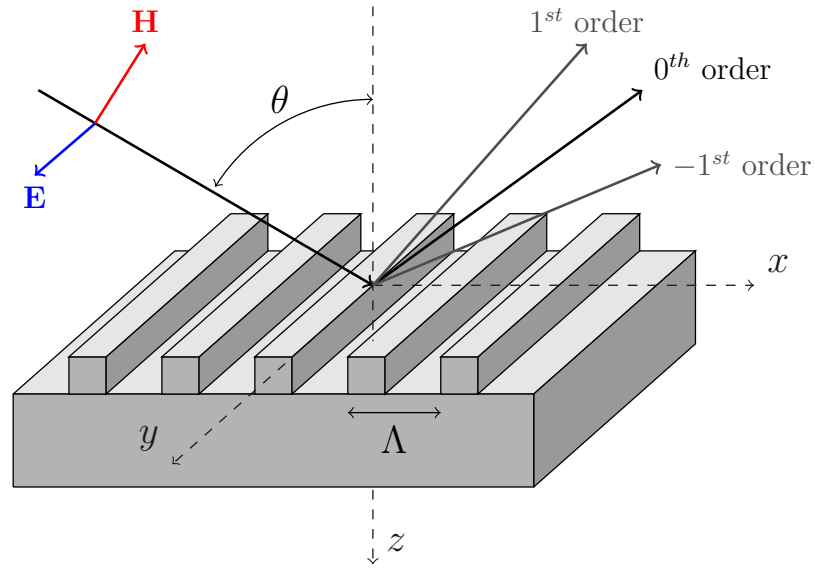
3.1.2 Rigorous coupled-wave analysis (RCWA) method

The rigorous coupled-wave analysis (RCWA) method is a semi-analytical method that is well-suited for modelling lamellar periodic structures. It is based on the analysis of diffracted spatial harmonics created when an incoming plane wave illuminates a period structure. The method was formulated by Moharam *et al.*

[70] for a metallic grating structure of complex permittivity $\varepsilon = \varepsilon' - j\varepsilon''$. To implement the RCWA method on a unidirectional metallic grating, the space domain is first sliced into three different regions as shown in Figure 3.3(a).



(a) Cross section view of a unidirectional grating of period Λ .



(b) Perspective view of a unidirectional grating of period Λ for a TE-polarised incoming wave.

Figure 3.3: Illustration of a unidirectional grating of period Λ .

Region I is the homogeneous input region of real permittivity ε_I . Region III is the homogeneous metallic region of complex permittivity ε_{III} . Region II is the grating region of period Λ for which the permittivity ε_{II} can be written as a Fourier expansion:

$$\varepsilon_{II}(x, z) = \varepsilon_{II}(x + \Lambda, z) = \sum_{p=-\infty}^{+\infty} \varepsilon_p(z) \exp \left[j \frac{2\pi p x}{\Lambda} \right], \quad (3.8)$$

where Λ is the grating period and ε_p is the complex Fourier coefficient.

For a TE-polarised incident plane wave, the electric field polarisation is perpendicular to the plane on incidence (the xz -plane as defined in Figure 3.3(b)).

The total electric field in Region I can be written as the sum of the incident wave and the emergent diffracted waves:

$$E_I = \exp[-j(k_{x0}x + k_{z0}z)] + \sum_{n=-\infty}^{+\infty} R_n \exp[-j(k_{xn}x + k_{znI}z)], \quad (3.9)$$

where $k_{x0} = k\sqrt{\varepsilon_I} \sin \theta$ is the x -component of the wavenumber in Region I, $k_{z0} = k\sqrt{\varepsilon_I} \cos \theta$ is the z -component of the wavenumber in Region I, $k = 2\pi/\lambda$ is the free space wavenumber, λ is the free-space wavelength, and R_n is the amplitude of the n^{th} order emergent-diffracted harmonic.

The x -component of the wavenumber for the n^{th} order emergent diffracted wave is expressed as $k_{xn} = k_{x0} - 2\pi n/\lambda$ and the z -component is written as $k_{znI} = \sqrt{(k^2\varepsilon_I - k_{xn}^2)}$.

The electric field in Region III can be expressed as the sum of incident diffracted waves:

$$E_{III} = \sum_{n=-\infty}^{+\infty} T_n \exp[-j(k_{xn}x + k_{znIII}(z - d))], \quad (3.10)$$

with $k_{znIII} = \sqrt{(k^2\varepsilon_{III} - k_{xn}^2)}$.

In Region II, the electric field can be expressed as a sum of spatial harmonics with matching wavenumber values at the interface with Region I and Region III:

$$E_{II} = \sum_{n=-\infty}^{+\infty} S_n(z) \exp[-j(k_{xn}x + k_{z0}z)], \quad (3.11)$$

where $S_n(z)$ is the complex Fourier coefficient of the n^{th} spatial harmonic.

Furthermore, in Region II, and for a TE-polarised incoming plane wave, the electric field satisfies the Helmholtz wave equation:

$$\nabla^2 E_{II} + k^2\varepsilon(x, z)E_{II} = 0. \quad (3.12)$$

By substituting E_{II} from Equation 3.11 into Equation 3.12, for each space

harmonic, Equation 3.12 becomes:

$$\frac{d^2 S_n(z)}{dz^2} - j2k_{z0} \frac{dS_n(z)}{dz} = (k_{xn}^2 + k_{x0}^2) S_n(z) - k^2 \sum_{p=-\infty}^{+\infty} \varepsilon_p(z) S_{n-p}(z). \quad (3.13)$$

Equation 3.13 is an infinite set of second-order differential, rigorous coupled wave equations. Each of those equations can be solved with a state-variable method used in linear systems analysis, described by Moharam *et al.* [71], and by matching the boundary conditions between the interfaces. The number of diffracted waves needs to be limited so as to solve the rigorous coupled wave equations with limited computational resources.

The Optiscan software implements the RCWA method within the Matlab environment [72, 73] and was used to simulate the 2D metallic gratings presented in Chapter 5. Region I was defined as air ($\varepsilon_I = 1.0005$) and the complex permittivity of Region III was defined as to be a perfect electric conductor (PEC).

3.2 Fabrication processes

Throughout the project, several Bull's eye antenna prototypes were fabricated to allow a comparison between the simulated and the measurement results and illustrate the feasibility of the concept. Three main processes were used for the fabrication of Bull's eye antenna prototypes: a mechanical milling process and an electrical discharge machining process for the Bull's eye antenna, and a photolithography process for the microstrip-based feed.

3.2.1 Mechanical milling process

A milling process was used to machine a work piece by removing material using rotating milling tools. The table on which the work piece is mounted can usually move along one or multiple axes. The optimal tool rotation speed and feed rate are key parameters to achieve the highest machining quality and increase the tool's lifetime. Those empirical values mainly depend on the type of material to machine and the characteristics of the milling tool [74]. The choice of the metal was based on a trade off between the volumetric mass density, the price, the electrical conductivity and the availability of the material. A 6082 aluminium

alloy, made of 95.2 to 98.3% of aluminium, was chosen for the fabrication of the Bull’s eye antennas for the following reasons. Firstly, the density of the 6082 alloy is 3.3 times lower than copper (2.70 against 8.96 g/cm^3) which is key for CubeSat applications where the weight is at a premium. Secondly, the bulk 6082 alloy is two times less expensive than the copper that is widely used in the RF industry (1.5 against 3.4 £/kg on average), which is relevant for terrestrial applications that require high production volumes. Thirdly, despite a lower electrical conductivity of the 6082 alloy ($2.63 \times 10^7 \text{ S/m}$) compared to copper ($5.96 \times 10^7 \text{ S/m}$), it was readily available at the mechanical workshop of the University of Glasgow.

The fabrication was carried out in the workshop of the University of Glasgow with a three-axis XYZ SM2000 CNC milling machine and with a Datron micro-milling machine, using solid carbide milling tools. Typical cutting speeds for aluminium alloys ranges from 75 to 105 m/min . The corresponding rotational speed is a function of the diameter of the milling tool and is between $24,000$ to $33,000 \text{ rpm}$ for a 1.0 mm tool. After milling the surface relief features, a thread milling tool was used to manually create the UNC 4-40 thread to accommodate the screws of the standard UG385/U flange for WR-15 waveguides as defined in Figure 3.4 and Table 3.1. The WR-15 waveguide has a standardised width of 0.148 mm and height of 0.074 mm . The values ($3.7592 \times 1.8796 \text{ inches}^2$) from the metric conversion are impractical to manufacture and are approximated to $3.76 \times 1.88 \text{ mm}^2$.

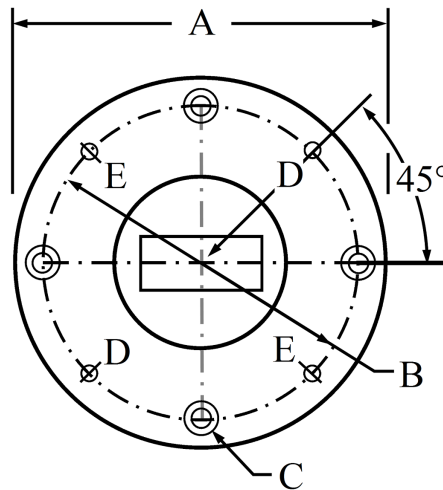


Figure 3.4: Drawing schematic of a standard UG385/U flange for WR-15 waveguides.

Table 3.1: Dimensions in millimetres of a standard UG385/U flange for WR-15 waveguides.

A	B	C holes	D holes	E dowels
19.05	14.29	4-40 UNC	1.613	1.555

3.2.2 Electrical discharge machining process

A mechanical milling process was used for most of the fabrication of the Bull’s eye antenna. However the small width of the subwavelength aperture with respect to the depth appeared to be a limiting factor as small milling tools are not suited for large aspect ratio profiles. As a result, an electrical discharge machining (EDM) process was used and allowed accurate drilling of the aperture. The EDM process is based on the removal of conductive material by a controllable electrode as shown in Figure 3.5. The work piece is immersed in a dielectric fluid and a pulsed voltage is applied between electrode and the work piece. If this voltage is higher than the breakdown voltage of the dielectric fluid, a spark is created between the two parts and produces intense heat that melts the close-surrounding area. The dielectric fluid flushes away the debris, then the process repeats. The EDM process was conducted in the Faculty of Mathematics, Computing & Technology at the Open University.

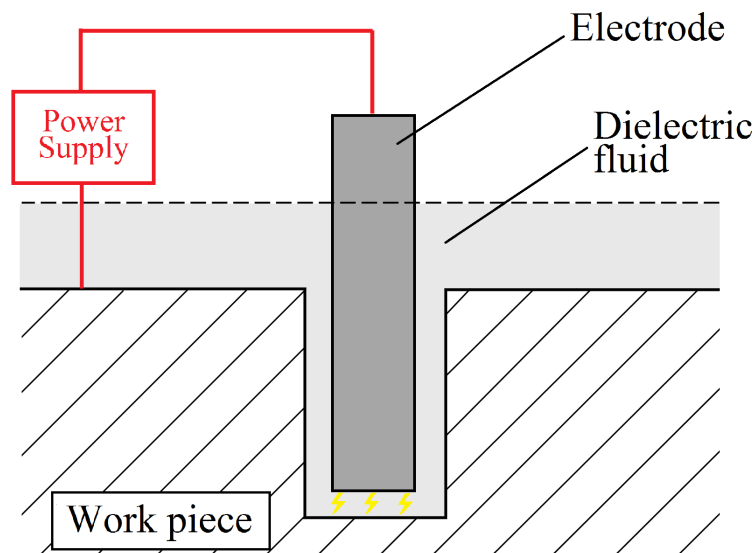


Figure 3.5: Schematic of the electrical discharge machining process illustrating the work piece, the electrode and the dielectric fluid.

3.2.3 Photolithography process

In Section 4.2, a microstrip waveguide feed was needed. For this, a photolithography process was used to fabricate printed circuit boards (PCBs). The PCB substrates are usually laminates, made of epoxy or polytetrafluoroethylene (PTFE) reinforced with woven glass or ceramic inclusions, and clad with one or two sides with copper. The photolithography process is achieved through the following steps:

1. Application of the photoresist on the conductive surface
2. Alignment of the photomask, designed and fabricated beforehand
3. Exposure and development of the photoresist, revealing the areas to etch
4. Etching of the conductive material with wet (liquid chemical) or dry (plasma)
5. Removal of the photoresist

The first part of the photolithography process (1 to 3) was carried out in the James Watt Nano-Fabrication Centre (JWNC) and the last part (4 and 5) in the Electronic Workshop of the School of Engineering at the University of Glasgow.

3.3 Measurement tools

This Section presents the measurement tools used for Bull's eye antenna characterisation at V-band frequencies as used inside an anechoic chamber. The properties of the anechoic chamber are outlined first. The structure of the test bench and the data acquisition process are described next. Subsequently, post-processing leading to reconstruction of the 2D radiation pattern is described.

3.3.1 Anechoic chamber

An anechoic chamber is a confined room providing a clean electromagnetic environment, such as to measure the far-field radiation pattern of an antenna. Two key mechanisms are involved in providing a clean test environment:

1. The external structure of the chamber acts as a Faraday cage and constitutes a shield against external electromagnetic contamination.
2. The inside walls are covered in carbon-loaded pyramidal absorbing foam to limit multipath reflections within the chamber.

The anechoic chamber available at the University of Glasgow measures $4.5 \times 4.5 \times 4.0 \text{ m}^3$ and the inner walls are covered with EHP-18PCL pyramidal absorber manufactured by ETS-Lindgren. Figure 3.6(a) shows a photograph of the anechoic chamber and Figure 3.6(b) shows the dimensions of the EHP-18PCL pyramidal absorber-tile. Figure 3.6(c) shows a plot of the reflectivity of the EHP-18PCL pyramidal absorber between 0 and 40 GHz which is guaranteed to be better than -50 dB between 4 and 40 GHz, and featured ‘for the reduction of reflections from 30 MHz through 100 GHz’. It is reasonable to assume that the reflectivity of the EHP-18PCL pyramidal absorber is better than -50 dB at 60 GHz.

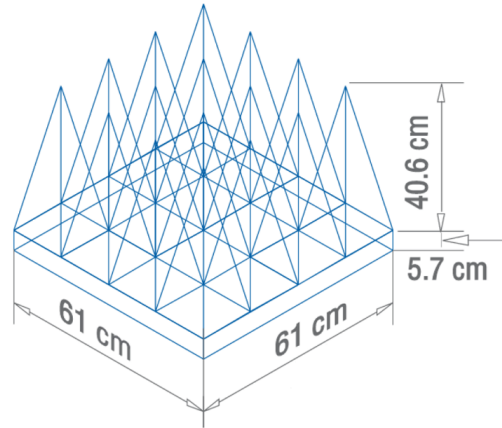
3.3.2 V-band test bench

A 2D far-field measurement system was built to characterise antenna radiation properties at V-band. As shown in Figure 3.7(a), the test bench consists of an antenna under test (AUT) mounted on a Newport URM80APP single axis mechanical rotating stage and aligned with a fixed, 23 dBi horn antenna (Custom Microwave Inc., model HO15R). The AUT and the horn antenna are respectively connected to port 1 and port 2 of an Agilent PNA E8361A VNA operating between 10 MHz and 67 GHz. Figure 3.7(b) shows a photograph of the AUT mounted on the Newport URM80APP rotating stage inside of the anechoic chamber presented in the previous Section.

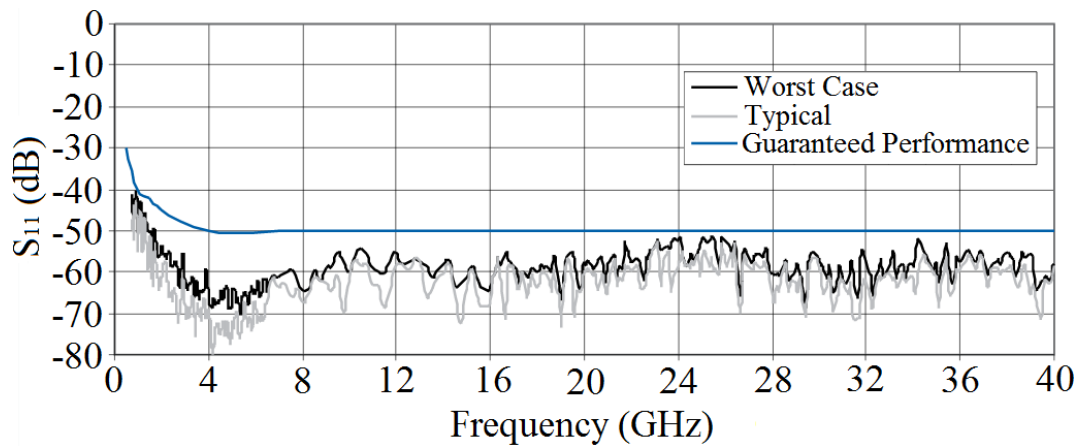
Figure 3.8 illustrates the acquisition scheme and data post-processing leading to the 2D radiation pattern of the AUT. For each angular position θ of the rotating stage, a .s2p file which contains the S_{11} , S_{12} , S_{21} and S_{22} parameters within the frequency range of interest is created. As a result, sets of S_{21} are recorded as a function of frequency for each angular position θ and correspond to the transmission coefficient from port 1 to port 2. In addition, S_{21} is averaged in order to improve measurement accuracy by increasing the signal-to-noise ratio.



(a) Photograph of the anechoic chamber at the University of Glasgow.



(b) Dimensions of a 4×4 EHP-18PCL pyramidal absorber tile (from [75]).

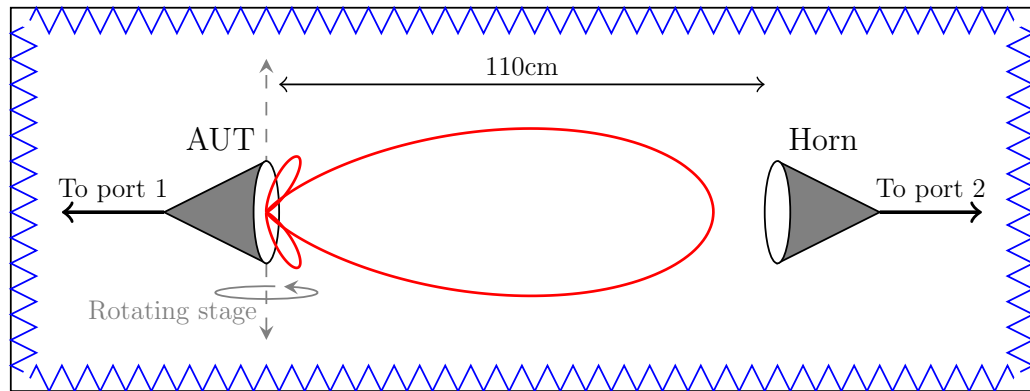


(c) Plot of the reflectivity of the EHP-18PCL pyramidal absorber between 0 and 40 GHz (from [75]).

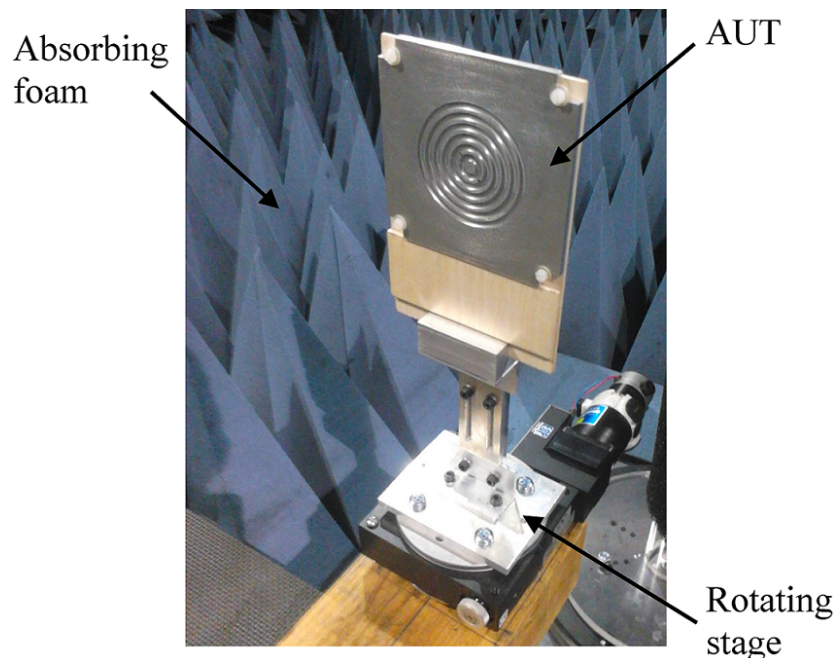
Figure 3.6: Characteristics of the EHP-18PCL pyramidal absorber covering the walls of the anechoic chamber.

In order to obtain the radiation pattern at a particular frequency f_0 , the averaged data are then rearranged so as to plot S_{21} as a function of θ . The radiation pattern is then normalised to the maximum gain value.

For the purpose of this study and because of limited cable length, the V-band test bench was built with a distance of 110 cm between the AUT and the fixed



(a) Schematic of the testbench setup used for V-band antenna characterisations.



(b) Photograph of the AUT mounted on the Newport URM80APP rotating stage inside of the anechoic chamber environment.

Figure 3.7: Test bench for V-band radiation pattern and gain measurement.

horn antenna. This distance corresponds to the maximum span obtained with the available coaxial cables connecting the AUT and the horn antenna to the VNA. At 60 GHz, the far-field transition occurs at about $400D^2$ meters, where D is the maximum dimension of the AUT. As the distance between the AUT and fixed horn antenna is 110 cm or 220λ , the maximum antenna aperture is calculated to be around 75 mm so as to measure the far-field pattern. The phase centre of the AUT and the horn antenna, defined as the point from which the spherical

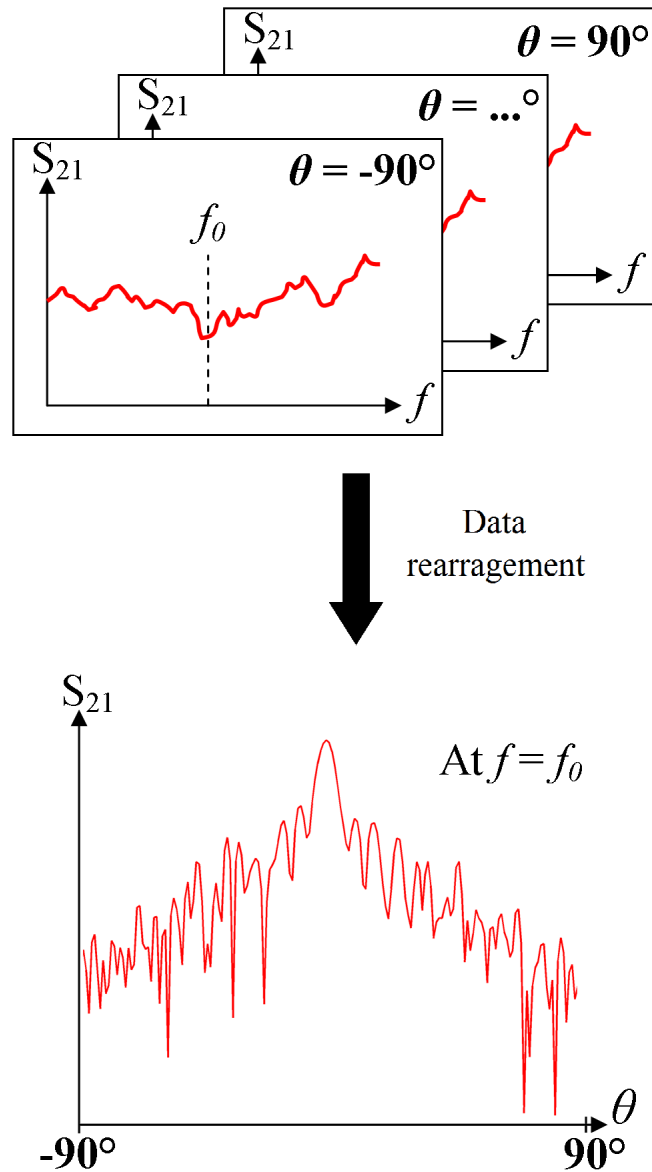


Figure 3.8: Schematic example showing a S_{21} parameter acquisition and data post-processing for displaying of the radiation pattern for θ between -90° and $+90^\circ$ at frequency f_0 .

wavefronts appear to emanate, needs to be strictly aligned. However the direction of the horn antenna boresight does not need to be precisely oriented within this alignment as long as this direction is constant throughout the measurement. Only the relative angular position of the AUT needs to be precisely known with respect to the direction defined by the phase centres. Moreover, the available semi-rigid

cables did not provide enough flexibility for the stage to be automated. In order to prevent the damage of any parts of the test bench, the rotating stage was manually operated and the angular range was limited to about -100 to $+100^\circ$. This method leads to random error on angular alignment for each measurement point. This source of error could be mitigated by averaging multiple, independent measurements for each point at the expense of the total measurement speed. Systematic sources of errors include multiple reflections (chamber and test bench), amplitude and phase variation when flexing the cables, temperature variation effects, VNA dynamic range and crosstalk.

3.3.3 Gain Transfer Method

Two methods are commonly used to measure the gain of an antenna. The first method is the gain transfer method [76], also known as the gain-comparison method, and the second method is the absolute gain method. Only the gain transfer method was used for the characterisation of antennas presented in this Thesis, and will be detailed here. The gain-comparison method requires three antennas: the AUT, a reference antenna and an arbitrary antenna corresponding to the horn antenna of the testbench in the previous section. The method allows the measurement of the gain $G_{AUT,dBi}$ of an AUT by comparing it to the gain $G_{ref,dBi}$ of a reference antenna. A first set of measurement is performed to acquire the power received by the AUT, $P_{AUT,dB}$, when illuminated by the horn antenna. The second set is performed to measure the power received by the reference antenna $P_{ref,dB}$, keeping all other conditions identical. The gain of the AUT is given by:

$$G_{AUT,dBi} = G_{ref,dBi} + P_{AUT,dB} - P_{ref,dB}. \quad (3.14)$$

3.4 Chapter summary

This Chapter introduced key methods used in this Thesis, ranging from simulation techniques (Section 3.1), to fabrication methods (Section 3.2), and measurement techniques (Section 3.3) used to develop the Bull's eye antenna prototypes.

In particular, the finite-difference time-domain (FDTD) method, the finite integration technique (FIT) method implemented in the commercial solver tool CST Microwave Studio, and the Rigorous Coupled Wave Analysis (RCWA) method implemented in the Optiscan software, were presented. The choice of the materials used for the fabrication of the Bull's eye antennas and the fabrication techniques was then presented, including the mechanical milling, the electrical discharge machining (EDM) and the photolithography processes. Additionally, the anechoic chamber and the V-band test bench used for the characterisation of the Bull's eye antennas were described. Next, the first Bull's eye antenna design is presented.

Chapter 4

Bull's eye antenna design and feed

In this Chapter, the design of a Bull's eye antenna operating at 60 GHz is presented. A design for a CubeSat is produced with the aid of simulation tools, and then characterised in an anechoic chamber. The design of an alternative feed structure based on a microstrip-to-waveguide transition is then proposed, simulated, fabricated and characterised.

4.1 Bull's eye antenna operating at 60 GHz

In this Section, the design and simulation results of a standard Bull's eye antenna operating at 60 GHz with seven rings are first presented to illustrate the performance and show the possibility of integration onto a CubeSat chassis. Then, the fabrication process and the results are discussed.

4.1.1 Design and simulation

The Bull's eye antenna is made of a square plate of side length $L_{side} = 100$ mm and thickness $h = 3.20$ mm, with cut-outs in the four corners of 10×10 mm² to match the standard dimensions of a CubeSat chassis. The central raised region of diameter $D_c = 7.12$ mm contains the 0.53×3.40 mm² subwavelength aperture which generates the electromagnetic surface wave [77]. The period of the grating

4.1 Bull's eye antenna operating at 60 GHz

structure is 4.53 mm and the depth is 0.91 mm. The width of the indented rings $R_{indented}$ is 2.67 mm and the width of the high rings R_{high} is 1.86 mm. Figure 4.1 illustrates the dimensions of the design.

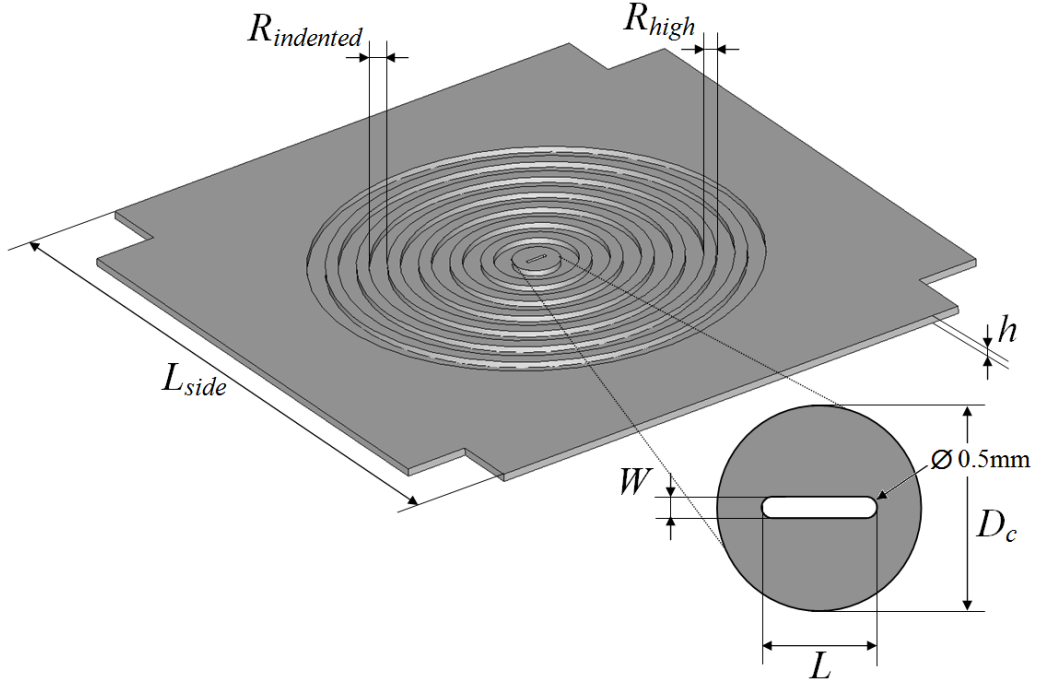


Figure 4.1: Perspective schematic view of a seven ring Bull's eye antenna with associated dimensions. Dimensions for a structure operating at 60 GHz are shown in Table 4.1 ©2014 IEEE [64].

The central subwavelength aperture is fed by a standard WR-15 rectangular waveguide from the rear of the plate. Ideally, the subwavelength aperture would have a rectangular shape but cannot be manufactured with standard milling tools. For this design, a rounded rectangular shape was chosen to simplify the fabrication process using a 0.5 mm diameter milling tool. The dimensions of the subwavelength aperture were optimised so as to improve the impedance match, under the constraint to be equal to the thickness of the aluminium plate (3.2 mm). The aperture has hence a length $L = 3.40$ mm, a width $W = 0.53$ mm, and radius of curvature of 0.265 mm. The dimensions are summarised in Table 4.1. These dimensions were obtained through an optimisation in order to obtain large gain and low return loss around 60 GHz. The starting point of the optimisation is the design rules given by Beruete *et al.* [56]. The optimised dimensions provided a gain increase at 60 GHz from 16.5 dBi to 18.6 dBi, and a bandwidth increase from

4.1 Bull's eye antenna operating at 60 GHz

2.43 GHz to 4.4 GHz for a five ring Bull's eye antenna, providing a satisfactory improvement.

Table 4.1: Dimensions in millimetres of a Bull's eye antenna operating at 60 GHz with the initial design rules provided by Beruete *et al.* [56] and the proposed improvements.

Dimensions (mm)	L_{side}	h	$R_{indented}$	R_{high}	D_c	W	L
Initial	100	3.2	2.5	2.5	5.53	0.53	3.4
Optimised	100	3.2	2.67	1.86	7.12	0.53	3.4

The number of indented rings is an important parameter because it sets the aperture size and influences the gain. This point was illustrated by running multiple simulations of the structure surrounded by a $100 \times 100 \text{ mm}^2$ conducting plate with zero to ten indented rings. The results in Table 4.2 show that the gain asymptotically reaches a maximum value that is a consequence of finite surface wave propagation distances in the presence of the rings. A simple subwavelength aperture surrounded by a flat, conducting surface, has a gain of 6.44 dBi. This improves to 18.2 dBi if ten indented rings are added, where ten is the maximum number of indented rings that can be contained on a standard $100 \times 100 \text{ mm}^2$ CubeSat face. The maximum gain reaches 19.6 dBi for eight indented rings. The gain increase per additional ring falls below 0.5 dB from six rings onwards, suggesting six or seven rings to be a good compromise between size and performance. The physical aperture A_p , the effective aperture A_{eff} and the aperture efficiency e_a are listed in Table 4.2. The physical aperture A_p corresponds to the corrugated area, the effective aperture A_{eff} is calculated as $A_{eff} = \frac{\lambda^2}{4\pi} G$ where λ is wavelength and G is the linear peak gain and the aperture efficiency is $e_a = \frac{A_{eff}}{A_p}$. An aperture efficiency ranging from 6 and 7% is typical and expected for a Bull's eye antenna [63].

Figure 4.2 shows the simulated S_{11} and maximum gain as a function of the frequency between 55 and 65 GHz. The impedance bandwidth at -10 dB is 5.06 GHz (8.4%), between 57.99 GHz and 63.05 GHz. A resonant frequency occurs at 60.08 GHz with a level of -55.4 dB . At 60 GHz, the S_{11} parameter is -38.0 dB and the maximum gain reaches 19.1 dBi. The resonant frequency of the antenna lies within the region of maximum gain, where the gain ranges between 16.7 dBi and 19.7 dBi within the impedance bandwidth.

4.1 Bull's eye antenna operating at 60 GHz

Table 4.2: Simulated gain versus number of indented rings, physical aperture, effective aperture, and aperture efficiency ©2014 IEEE [64].

Number of indented rings	Gain (dBi)	A_p (mm ²)	A_{eff} (mm ²)	e_a (%)
0	6.44	39.8	8.49	21.3
1	9.29	122	16.9	13.9
2	12.4	364	34.6	9.51
3	14.9	734	61.5	8.38
4	16.8	1240	95.2	7.67
5	18.6	1860	144	7.74
6	19.1	2620	161	6.15
7	19.1	3510	161	4.59
8	19.6	4520	181	4.00
9	18.9	5670	154	2.72
10	18.2	6400	131	2.05

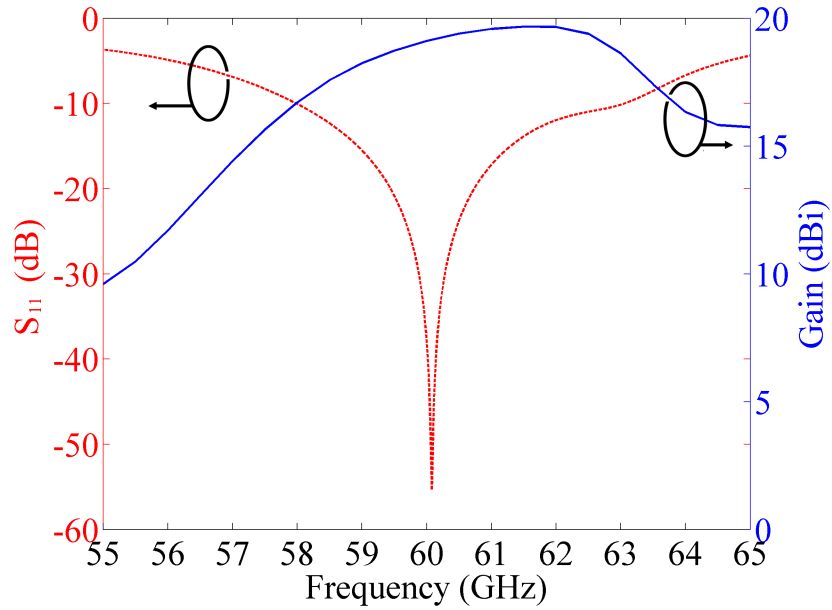


Figure 4.2: Simulated S_{11} (dB) and maximum gain (dBi) between 55 and 65 GHz ©2014 IEEE [64].

For comparison, a typical horn antenna operating in the V-band has a physical aperture $A_p = 1000 \text{ mm}^2$ and a gain of 23 dBi at 60 GHz, resulting in a aperture efficiency $e_a = 39\%$. This suggests that Bull's eye antennas are capable of achieving moderate peak gain with very low profile at the expense of the aperture efficiency. For these reasons, Bull's eye antennas should be preferred for applications where the available volume is more constrained than the available

surface.

4.1.2 Measurements

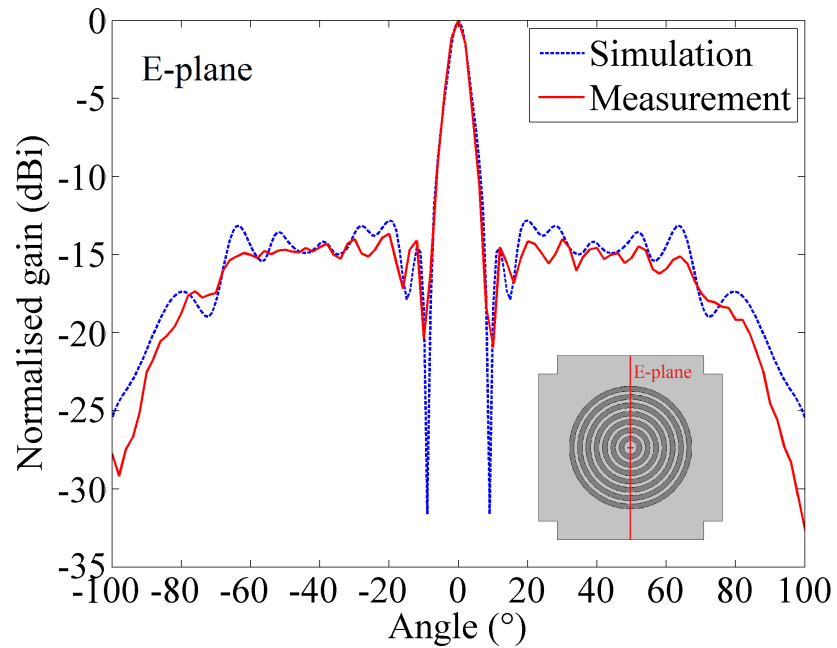
The measurements were taken with the V-band test bench and the method described in Chapter 3, Section 3.3. The Bull's eye antenna was fed with a 1.85 mm female coaxial connector to WR-15 waveguide adapter Ducommun, model PTC-15VF-01 (insertion loss of 0.5 dB) and connected to one port of the VNA with a semi-rigid coaxial cable. The E- and H-plane far-field radiation patterns were recorded successively, measuring the S_{21} parameter from -100° to $+100^\circ$ every 2° . The IF bandwidth was set to 500 Hz and the averaging to 10 points per sample. After rearranging the data according to the method described in the Chapter 3, Section 3.3.2, the radiation patterns were normalised with respect to the peak gain value.

Figure 4.3 shows close agreement between the simulation and the measurement of the E- and H-plane radiation patterns. The measurement planes of interest are shown in the insets.

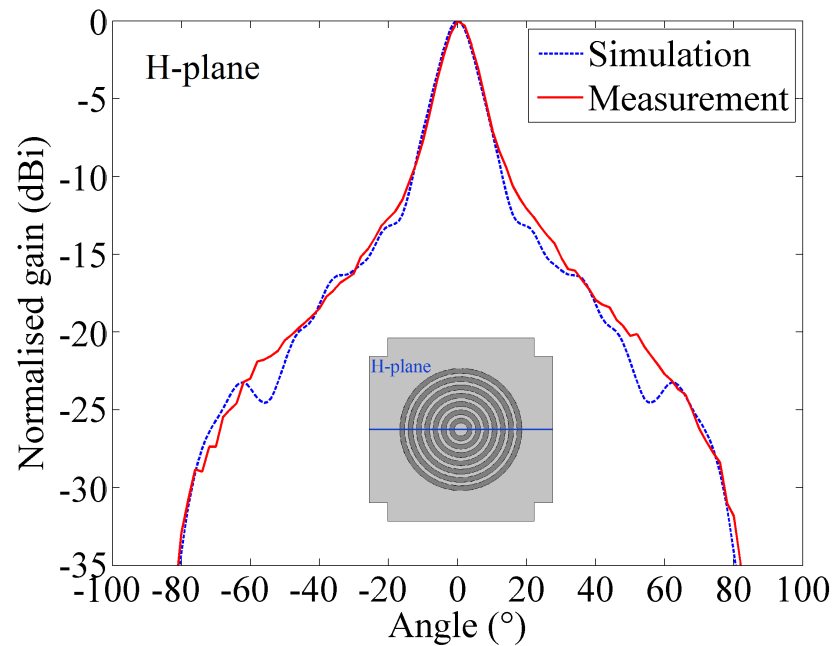
The E-plane radiation pattern simulation is close agreement with the measurement results. The error is smaller than 2.7 dB from -80° to $+80^\circ$, and smaller than 1.9 dB for the main beam pattern between -8° and $+8^\circ$. Similarly, the H-plane radiation pattern is in close agreement with error smaller than 3.4 dB. In particular, the H-plane radiation pattern measurement shows additional lobes at -23 dBi at $\pm 64^\circ$. The overall behaviour of the fabricated antenna shows the robustness of this Bull's eye antenna operating at 60 GHz to typical manufacturing tolerances. From conversations with commercial antenna manufactures, it was established that a single high gain antenna typically requires side lobes below 20 dB to be competitive in the market place. Since the targeted applications require tight space constraints, the current sidelobe level of 13 dB is considered to be an acceptable compromise.

Figure 4.4 shows the fabricated Bull's eye antenna integrated onto a 2U Cube-Sat chassis. It illustrates the low-profile of the structure, leaving a large amount for available payload. Even though the rectangular waveguide feed is well suited for laboratory measurement, an alternative feed structure is desirable for compactness and cost reduction.

4.1 Bull's eye antenna operating at 60 GHz



(a) E-plane (along the short side of the subwavelength aperture) radiation pattern.



(b) H-plane (along the long side of the subwavelength aperture) radiation pattern.

Figure 4.3: Measured and simulated, E-plane (a) and H-plane (b) radiation pattern ©2014 IEEE [64].

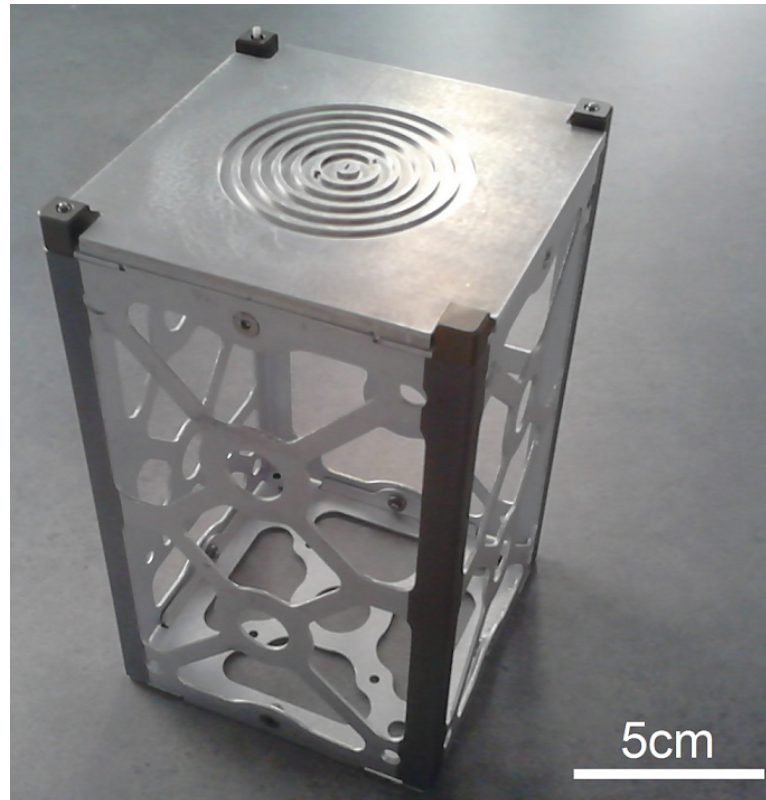


Figure 4.4: Fabricated 60 GHz Bull's eye antenna on the face of a 2U CubeSat chassis ©2014 IEEE [64].

4.2 Alternative feeding structure

A seven ring Bull's eye antenna operating at 60 GHz and fed by a standard WR-15 rectangular waveguide was presented in the previous Section. Due to the high fabrication cost of standard waveguide connectors, Bull's eye antennas fed by a standard WR-15 rectangular waveguide may be less attractive for lost cost and high volume production. In this Section, a more versatile feeding technique is introduced. The proposed structure is based on a microstrip-to-waveguide transition to allow straightforward and inexpensive integration on chip of the Bull's eye antenna. The transition consists of a microstrip line supporting a TEM mode that coupled to the TE_{10} mode of a hollow waveguide through a resonant patch square. It is expected to allow for straightforward integration of a Bull's eye antenna with a monolithic microwave integrated circuit (MMIC) or other feed network that is implemented using standard planar circuit technologies [78].

The basic characteristics of microstrip lines are recapped, then the design and simulation results of the microstrip-based feed for Bull’s eye antennas are presented. The fabrication process and measurement data are then discussed.

4.2.1 Microstrip

A microstrip is a planar transmission line based on PCB technology. The concept was first developed in 1952 by Grieg and Engelmann [79]. It was then intensively studied and used for decades [80] because of its low cost for modern microwave applications. Coplanar waveguides (CPWs) are more efficient and usually preferred for applications for millimetre-wave design but microstrip technology was chosen for the sake of design and fabrication simplicity. As illustrated in Figure 4.5, a microstrip consists of a line of a conducting material (the ‘strip’) of width w suspended above a ground plane by dielectric material (the ‘substrate’) of relative permittivity ϵ_r and of thickness h . Because of the asymmetry of the design, with the substrate permittivity being larger than that of air, a microstrip cannot support a pure TEM mode. Instead, the supported electromagnetic mode is a so-called quasi-TEM mode with non-zero longitudinal components.

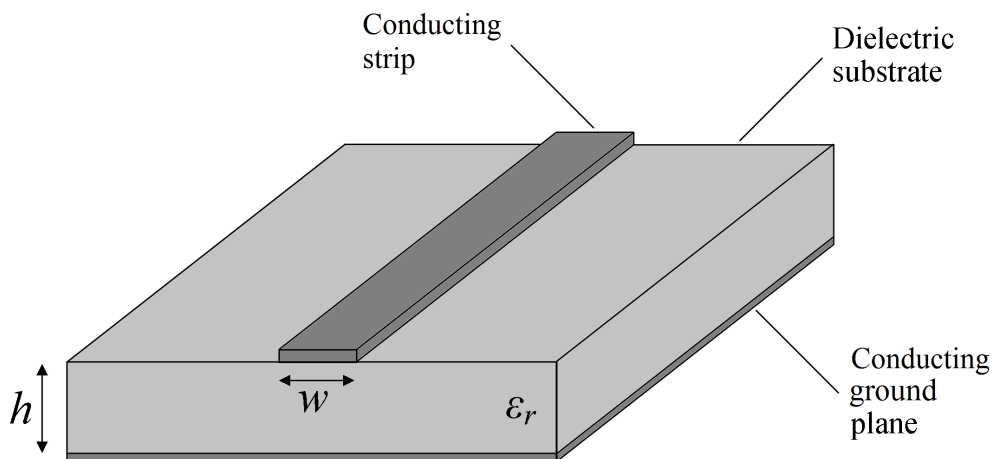


Figure 4.5: Perspective view of a microstrip where w is the width of the conducting strip, h is the thickness of the dielectric substrate, and ϵ_r is the relative permittivity of the dielectric substrate.

Analytical equations are available to assist with the design. According to Wheeler and Hammerstad [81, 82], the width w of a microstrip can be expressed

as a function of the thickness h of the substrate, the relative permittivity ε_r of the substrate and the line impedance Z_0 with:

if $Z_0 \geq (44 - 2\varepsilon_r)\Omega$,

$$\frac{w}{h} = \left(\frac{\exp(A)}{8} - \frac{1}{4 \exp(A)} \right)^{-1}, \quad (4.1)$$

where

$$A = \frac{\pi Z_0 \sqrt{2(\varepsilon_r + 1)}}{377} + \frac{1}{2} \left(\frac{\varepsilon_r - 1}{\varepsilon_r + 1} \right) \left(\ln \frac{\pi}{2} + \frac{1}{\varepsilon_r} \ln \frac{4}{\pi} \right), \quad (4.2)$$

or, if $Z_0 < (44 - 2\varepsilon_r)\Omega$,

$$\frac{w}{h} = \frac{2}{\pi} \left[B - 1 - \ln(2B - 1) + \frac{\varepsilon_r - 1}{2\varepsilon_r} \left(\ln(B - 1) + 0.293 - \frac{0.517}{\varepsilon_r} \right) \right], \quad (4.3)$$

where

$$B = \frac{377\pi}{2Z_0\sqrt{\varepsilon_r}}. \quad (4.4)$$

At $Z_0 = 44 - 2\varepsilon_r\Omega$, the width of the microstrip calculated with Equations 4.1 and 4.3 agrees to better than 4.7% with a notional microstrip using a 0.127 mm thick substrate of relative permittivity $\varepsilon_r = 2.2$. However these equations only provide guidelines and the dimensions usually need to be refined to achieve the required characteristic line impedance Z_0 .

4.2.2 Design and simulation

The proposed microstrip-feed design is based on a succession of segments allowing the coupling between a microstrip line and hollow waveguide, necessary to excite the surface wave launched by the Bull's eye subwavelength aperture. These individual segments are:

1. A microstrip, supporting a quasi-TEM mode;
2. A resonant square patch, supporting a TM_{01} ;

3. A hollow waveguide, supporting a TE_{10} mode, which feeds the Bull's eye subwavelength aperture.

Figure 4.6 illustrates the successive modes, from the quasi-TEM mode supported by the microstrip (1) to the TE_{10} mode supported by the custom waveguide (2), through the TM_{01} mode of the resonant square patch (3).

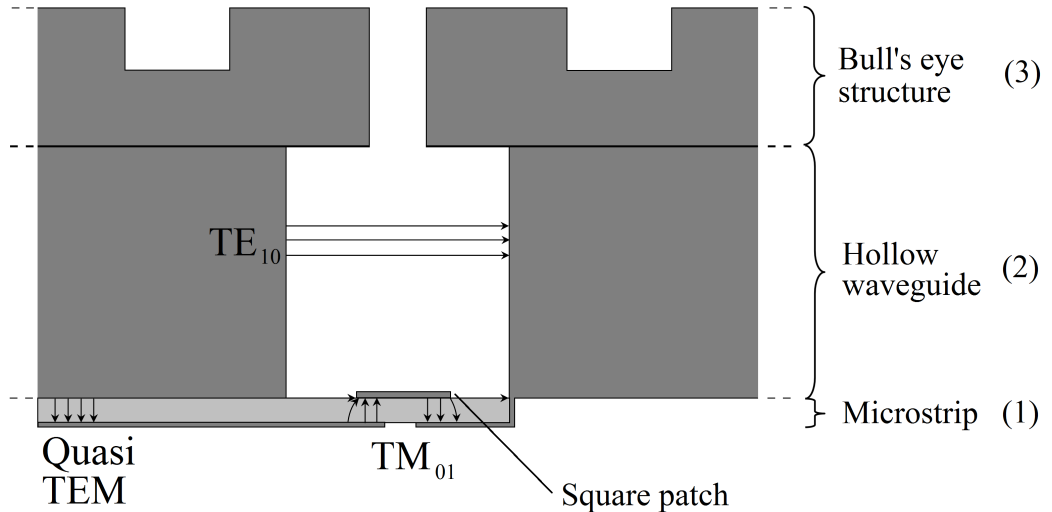


Figure 4.6: Schematic side view (cut away) of the microstrip-based feed providing coupling from the microstrip (quasi-TEM mode) to the Bull's eye structure through a hollow waveguide (TE_{10} mode) and a resonant square patch (TM_{01} mode).

The proximity coupling structure between the microstrip and the resonant square patch was based on the design proposed by Iizuka *et al.* [83], but modified and scaled to operate at 60 GHz. It uses a 0.127 mm thick Rogers RT/duroid 5880 substrate from Rogers Corporation. This substrate has a relative permittivity of $\epsilon_r = 2.2$ and a dielectric loss of $\tan \delta = 0.0009$ at 10 GHz, which minimised the dielectric loss, particularly important at the high frequency of interest. To illustrate the impact of the dielectric properties on the performance of a microstrip, the total attenuation which consists of the sum of the dielectric loss, the conductor loss and the radiation loss was calculated for three common Rogers laminates: R04350B, R04003C, and RT/duroid 5880. The tool MWI-2016 developed by Rogers Corporation was used to compute the values for a 0.508 mm thick microstrip line of 50Ω impedance. Figure 4.7 shows results as a function of frequency, between 1 and 60 GHz. It suggests that the RT/duroid 5880 laminate performs at least three times better than the R04350B at 60 GHz with total attenuation lower than 0.15 dB/cm.

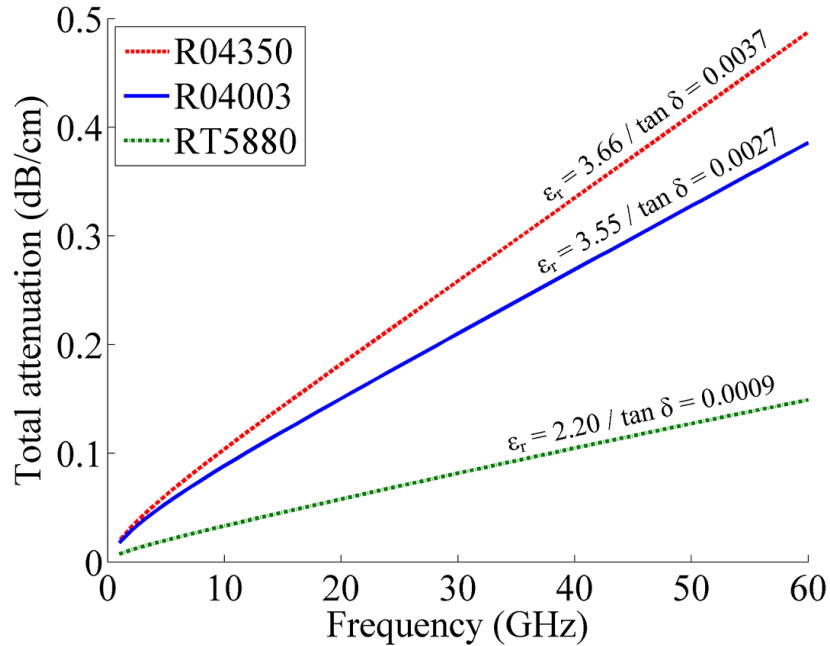


Figure 4.7: Plot of the calculated specific attenuation (dB/cm) for a 0.508 mm thick microstrip of $50\ \Omega$ impedance using the R04350B, R04003C, and RT/duroid 5880 laminates.

The length of the substrate L has been chosen to be 30 mm and the width W to be 25 mm, in order to accommodate a feeding port at the edge of the structure, essential for measurement purposes. The theoretical width of the microstrip $W_L = 0.39$ mm was calculated with Equation 4.1 and was adjusted during the simulation phase to $W_L = 0.37$ mm to better match the input impedance of $50\ \Omega$. The resonant square patch has a width and length of $L_p = 1.495$ mm to support a TM_{01} mode. All millimetre dimensions of the microstrip feed design are summarised in Table 4.3 and illustrated in Figure 4.8.

Table 4.3: Millimetre dimensions of the microstrip to waveguide feed transition ©2016 IEEE.

L	R	W	d	c	L_p	L_a	W_a	h	g	a	W_L
30.0	2.0	25.0	11.0	15.0	1.495	4.0	2.0	0.563	0.11	0.5	0.39

Figure 4.9 shows an exploded view of the full structure and the inset plot shows S_{11} as a function of the waveguide transition thickness w_t . The hollow waveguide, which is the transition between the square patch and the Bull's eye antenna, is manufactured with chamfered corners. This allows a cheaper and

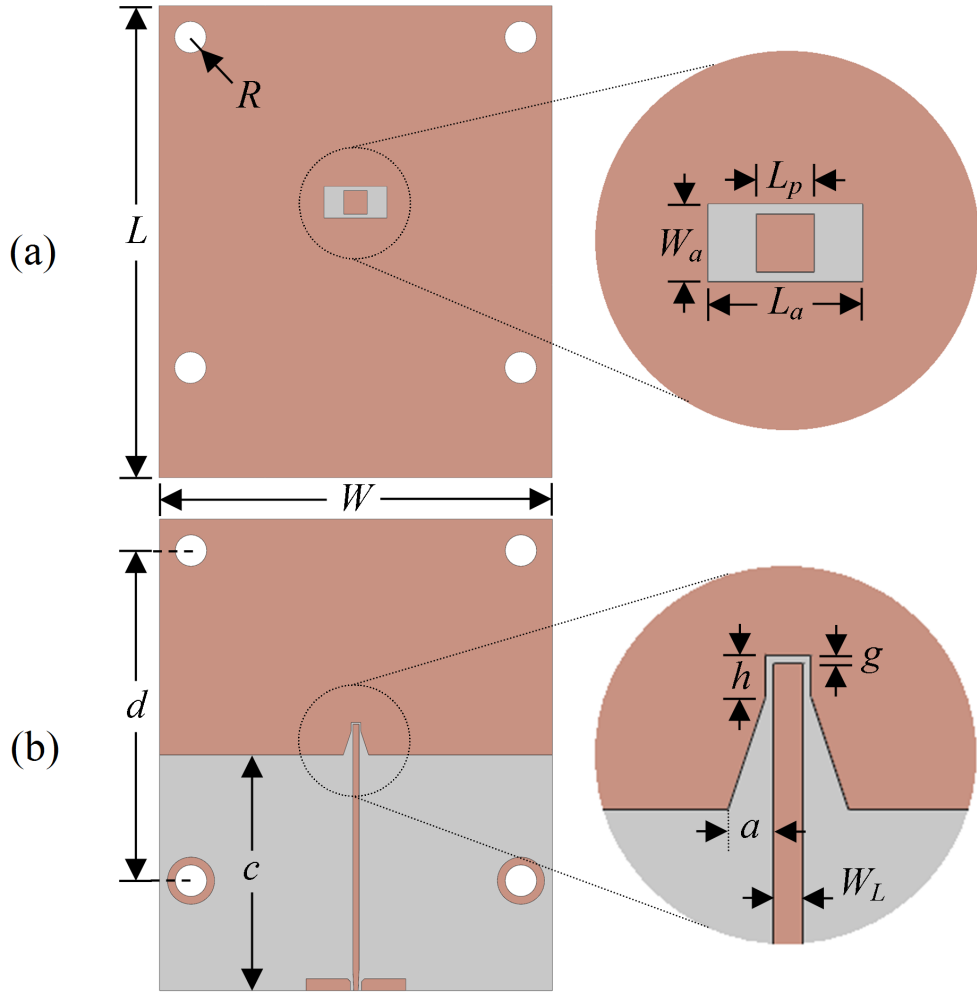


Figure 4.8: Millimetre dimensions of the microstrip transition from the top (a), and bottom (b). The top view has an inset showing an enlarged view of square patch, while the bottom view, the tapered ground under the patch ©2016 IEEE.

more straightforward fabrication processes, using only one milling or EDM tool. The thickness of the hollow waveguide w_t is 2 mm and was optimised in order to obtain best return loss at 60 GHz for the thinnest possible structure as shown by the inset plot in Figure 4.9.

The full structure comprises three parts manufactured separately: the microstrip board, the custom waveguide and the Bull's eye antenna. A $25 \times 25 \text{ mm}^2$ V-band Bull's eye antenna with two indented rings was designed, similar to the one presented in Section 4.1. The overall dimensions and the number of rings of the Bull's eye are chosen to be quicker to fabricate as well as to illustrate the flexibility of the Bull's eye design with a moderate gain. The number of rings can be

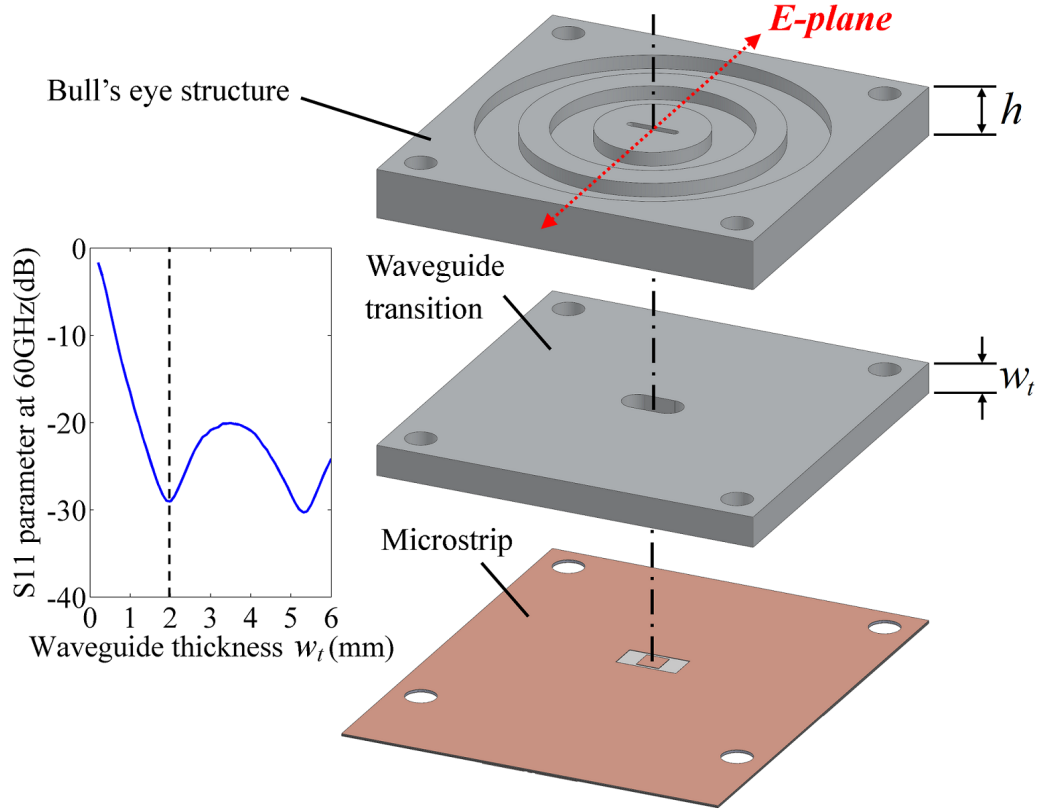


Figure 4.9: Exploded 3D view the Bull's eye antenna with microstrip-to-waveguide transition with inset of S_{11} values as a function of waveguide transition thickness ©2016 IEEE.

adjusted depending on the required maximum gain and the desired application, without modification of the feed structure. Hence higher gain antennas such as that in Table 4.2 can be fed with a similar structure at the expense of the overall size.

S_{11} for the simulated Bull's eye, fed separately by a standard WR-15 waveguide and by the proposed microstrip structure, are plotted Figure 4.10.

The minimum value of S_{11} had shifted slightly by 0.3 GHz, from 60.1 GHz at -46.9 dB, for the reference waveguide fed Bull's eye antenna, to 59.8 GHz at -29.0 dB. The -10 dB bandwidth decreases from 4.37 GHz (7.3%) to 3.41 GHz (5.7%) but the -20 dB bandwidth increases by 430 MHz. Those simulation results illustrate the potential performance of the proposed feed technique.

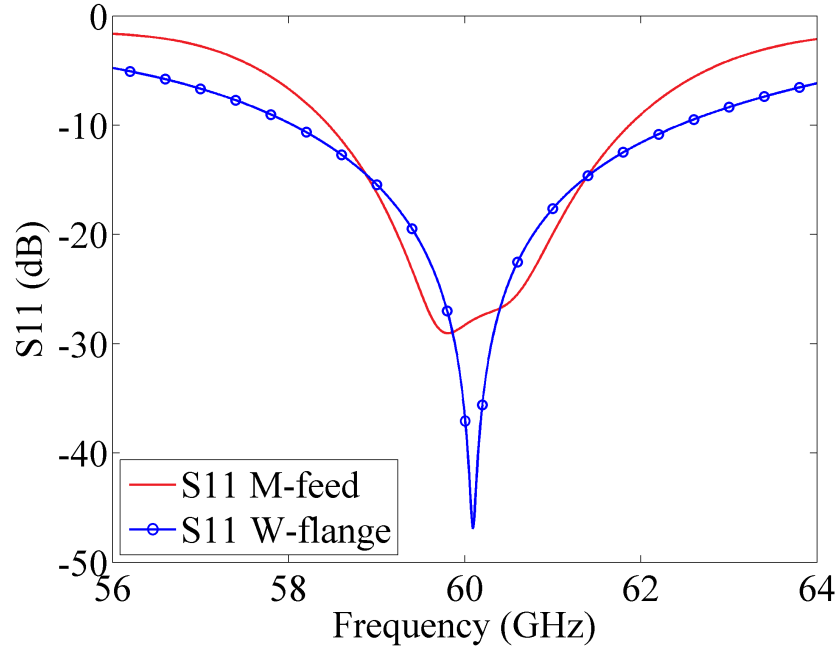


Figure 4.10: Plot of simulated S_{11} of the Bull's eye antenna fed with the microstrip-to-waveguide transition (M-feed, solid red line) and with a WR-15 waveguide (W-flange, blue circle markers) ©2016 IEEE.

4.2.3 Fabrication and measurement

The microstrip was fabricated with a 0.127 mm Rogers RT/duroid 5880 substrate, clad on both faces with 35 μm copper (1 oz/ft²), using a wet etch process. The precise fabrication steps of the photolithography process, introduced in Chapter 3, were as followed with each sides treated successively:

- Application of AZ4562 positive photoresist on the surface by spin-coating at 4000 rpm for 60 sec to obtain a 6.2 μm thick resist layer;
- Baking in an oven for 6 min and 20 sec at 100 °C;
- Alignment of the chrome on glass photomask with a Süss MA6 system;
- Photolithography exposure with a 350 W mercury lamp at a wavelength of 365 nm for 25 sec;
- Development using a quarter dilution of AZ-400 developer and deionized water for 2 min and 30 sec;
- Rinsing in deionized water for at least 30 sec;

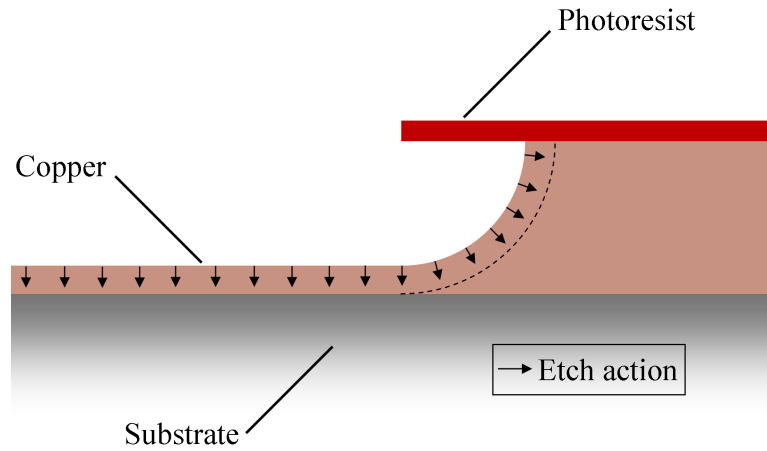
- Plasma (O_2) ashing for 2 min at $120^\circ C$;
- Hard baking on a hot plate for 10 min $120^\circ C$;
- Copper wet etching using ferric chloride ($FeCl_3$);
- Removing the remaining photoresist by soaking the sample in acetone for 1 min and blow drying with a nitrogen gun.

The undercut caused by the isotropic wet etch process, had to be accounted for during the design of the photomask, because the thickness of the copper was $35\ \mu m$ and the smallest features were $110\ \mu m$ gaps. To do so, preliminary etch tests were conducted on the substrate in order to estimate the size of the undercut. Figure 4.11(a) illustrates the concept of undercut during an isotropic wet etch process and Figure 4.11(b) shows a scanning electron micrograph (SEM) of the test sample after treatment. It shows the substrate after the etch on the left part of the figure, and the remaining copper on the right. This picture, taken with a SEM, allows estimation of the size of the undercut to be about $30\ \mu m$. The photomask had hence been modified accordingly, by increasing the outer section by the same amount.

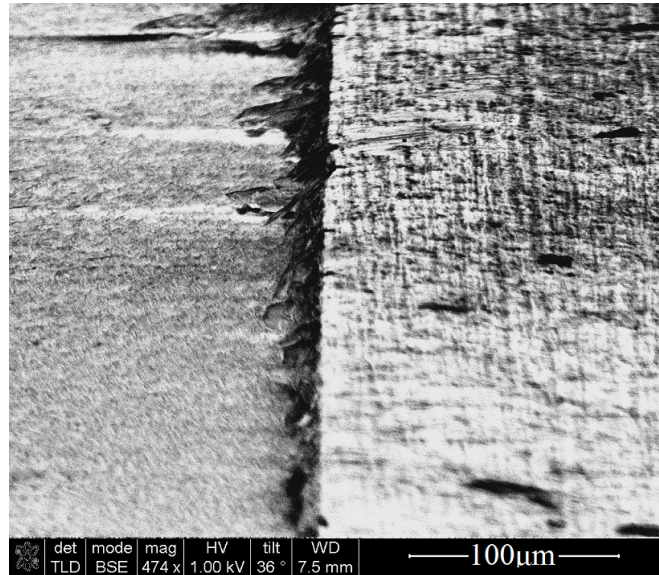
The waveguide transition and the Bull's eye structure were milled in aluminium with a CNC milling machine. The subwavelength aperture was fabricated at the Open University using an EDM process describes in the previous Chapter. The three elements were bolted together with four M2 screws. A 1.85 mm end launch connector (Southwest Microwave model 1892-03A-5) was mounted on the microstrip board to allow connection with a VNA for the measurements. The fully assembled microstrip-fed Bull's eye antenna is shown in Figure 4.12.

To provide the E- and H-plane radiation patterns, S_{21} was recorded at 60 GHz, from -60° to $+60^\circ$ every 2° , with a 500 Hz IF bandwidth and an averaging of 10 points per sample. Figure 4.13 shows the simulated and measured far-field radiation patterns of the studied structure.

The agreement between measured and simulated data is relatively poor, due to a number of factors, including mechanical stress on the microstrip adapter when rotating the Bull's eye antenna during the measurement process and parasitic reflections induced by the end-launch connector. However, the central portion of the E-plane radiation pattern between $\pm 10^\circ$ (Figure 4.13(a)) is in close agreement



(a) Diagram showing the undercut arising during the wet etch process.



(b) Test sample picture taken with a scanning electron microscope.

Figure 4.11: Illustration of the undercut concept under an isotropic wet etch process and micrograph showing a perspective view of the test sample showing the substrate after the etch (left part of the picture) and the remaining copper (right part of the picture).

and the overall trend for the H-plane radiation pattern (Figure 4.13(b)) is broadly consistent with the measurement results.

The fabrication of this part of the work was done as a favour to the project, so the resource was not available to iterate and refine the design. Nonetheless the principle has been shown to work within the limits imposed by the available

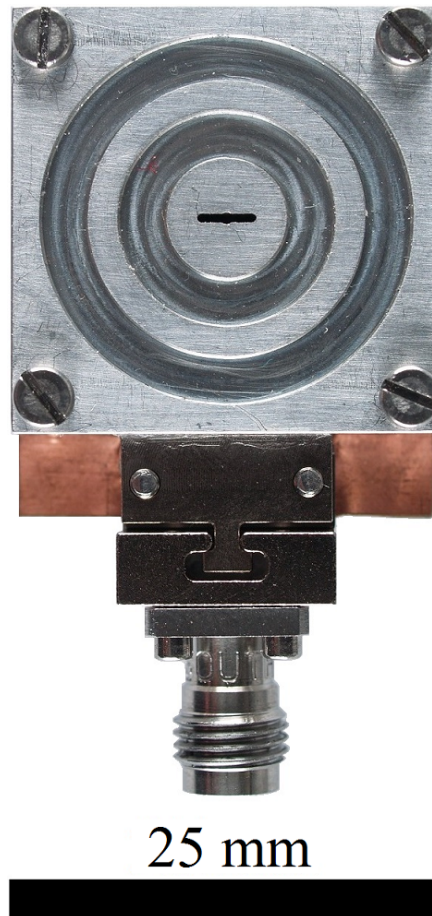
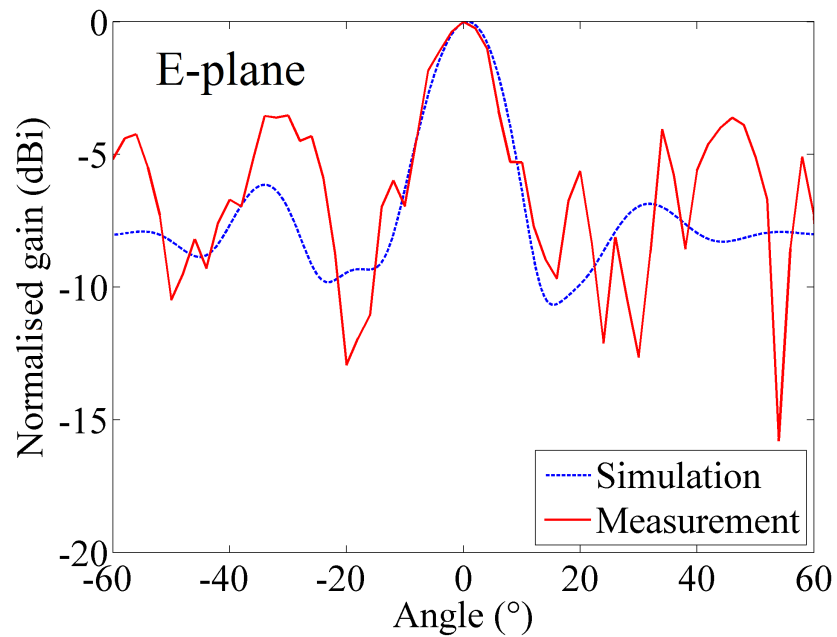


Figure 4.12: Photograph of the fabricated Bull's eye antenna mounted on the microstrip to waveguide transition ©2016 IEEE.

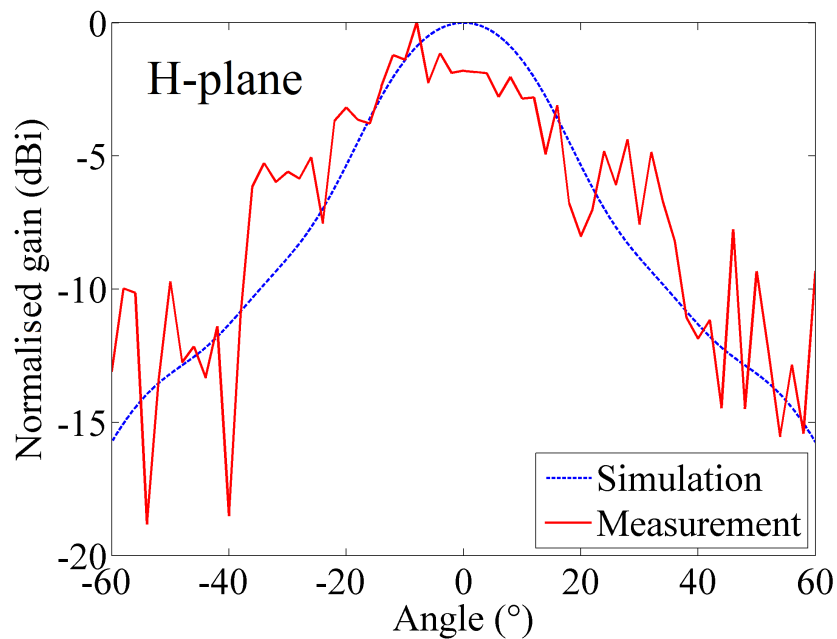
fabrication and gives confidence that future work could be successfully carried out if sufficient resources was allocated to implement the transition to industry standards.

4.3 Chapter summary

In this Chapter, the design of a corrugated Bull's eye antenna operating at 60 GHz was described. In the first Section, the full-wave simulation, the fabrication and the measurements of a seven ring Bull's eye antenna give confidence in the robustness of the design to manufacturing tolerances with a close agreement between the simulated and measurement results. The addition of indented rings increases asymptotically the gain of the antenna, reaching 19.1 dBi for seven indented rings



(a) E-plane radiation pattern.



(b) H-plane radiation pattern.

Figure 4.13: Simulated and measured E-plane (a) and H-plane (b) normalised radiation pattern at 60 GHz for Bull’s eye antenna fed with the microstrip-to-waveguide transition structure ©2016 IEEE.

with the design presented in this Chapter, illustrating the versatility of this antenna. In the second Section, a microstrip-based feed is proposed to tackle the

high manufacturing cost of standard rectangular waveguide and to extend the range of applications for upcoming wireless technologies. This solution allows coupling between a microstrip line and the Bull's eye antenna, via a resonant square patch and a custom waveguide. The necessary custom waveguide, transition between the square patch antenna the Bull's eye, is designed with chamfered internal corners to facilitate fabrication while maintaining a low insertion loss of 0.15 dB. Taken together, this provides a versatile solution to upcoming 60 GHz applications requiring low-profile and directive antennas. Now that a 60 GHz Bull's eye antenna has been experimentally validated, design enhancements can be considered.

Chapter 5

Bull's eye antenna improvements

In the previous Chapter, the design of a Bull's eye antenna operating at 60 GHz was described. As terrestrial and space applications may require flexibility in terms of relative position of the transmitter and the receiver, the main beam should be able to be directed in a direction away from the boresight. Examples include constellations of small satellite where the sides of the members are not directly facing each other. Additionally, it may be desirable to establish simultaneous communication with more than two parties, which would require two or more beams. In other cases, active steering is desirable to accommodate infrequent changes in the relative positions of the transmitter and the receiver. All of these requirements are targeted in this Chapter. After explaining that a one dimensional grating model is sufficient to predict the deflection angle with minimal computational effort and reasonable accuracy, it is shown that independent grating designs on each side of the aperture allows the deflection of separate beams by equal or different amounts. While a number of mechanical steering schemes are possible for the Bull's eye antenna, many are likely to be mechanically impractical. A straightforward solution based on a rotating plate divided into three different sectors, and a mask to prevent unwanted alteration of the radiation pattern, is designed, fabricated and measured. Then, the design of a conformal Bull's eye antenna, based on the modulation of the grating period is investigated. It shows that the Bull's eye is suitable for tight integration on a non-planar surface while preserving a high gain and a directive main beam.

5.1 Fixed beam deflection

In this Section, the effect of shifting the raised rings in one or more directions is investigated.

5.1.1 Single direction shift concept

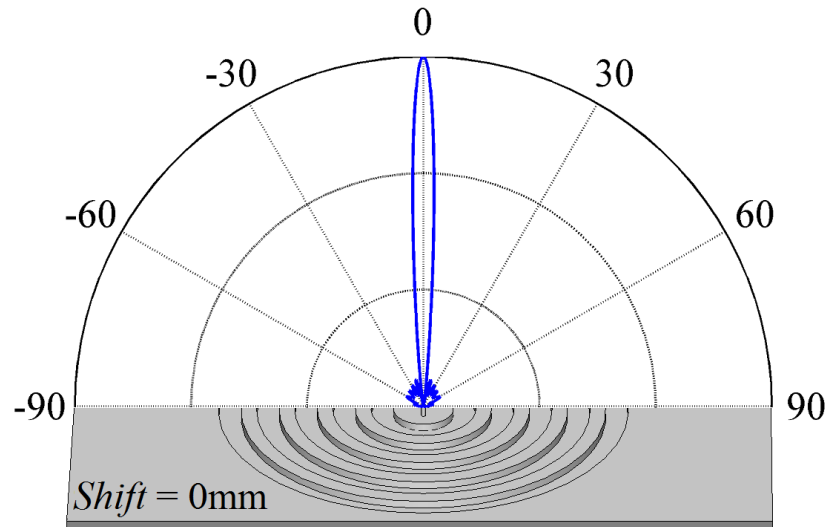
For a periodic LWA, the optimum coupling angle of a guided wave into free space is related to the period of the grating, as indicated by the grating equation presented in the Chapter 2. In order to systematically take advantage of this property for deflecting the beam of a Bull’s eye antenna, it is helpful to define a straightforward scheme for adjusting the grating period. This possibility has already been reported by shifting the centre of the rings at optical frequencies [84] and at millimetre-wave frequencies [64, 85, 86]. The initial aim is to design a Bull’s eye antenna at 60 GHz allowing beam deflection in a single direction, so the shift scheme is limited to only one direction, either along the E-plane or the H-plane.

The proposed shifting scheme is based on the Bull’s eye antenna design presented in the previous Chapter and is as follow. The centre of the n^{th} raised ring from the centre is shifted by $n \times Shift$, where $Shift$ is the offset of the innermost raised ring. The value $Shift$ is bounded such that the rings can be produced in a conventional milling machine. For the basic design detailed in the previous Chapter, this limits the value of $Shift$ to $R_{indented}$, which is 2.67 mm. This approach is preferable to the opposite approach where the size of the indented rings stays the same size and the size of the raised ring is adjusted. This alternative scheme reduces the degree of shift, reduces the gain and introduces unwanted side lobes in the radiation pattern, as shown in Appendix B.

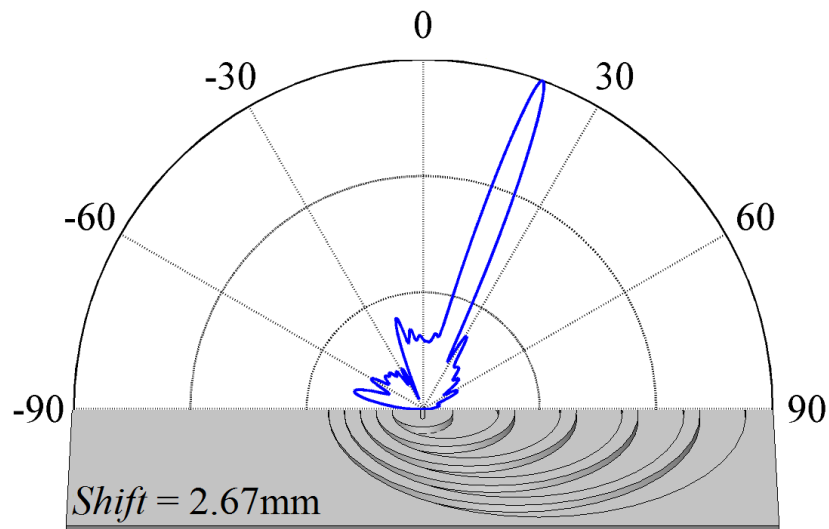
As a start, the far-field radiation patterns are plotted in Figure 5.1, using the shifting scheme previously described, for $Shift = 0.00$ and 2.67 mm in the form of normalised linear gain as a function of angle, with a perspective view of half of the associated Bull’s eye structure. This figure aims to illustrate the link between ring shift and the direction of deflection in the main beam.

A more complete parametric study was then carried out for a structure with shifted rings within the E-plane for $Shift$ ranging from 0.00 mm to 2.67 mm, in seven steps (0.00, 0.50, 1.00, 1.50, 2.00, 2.50, 2.67 mm). As shown in Table 5.1,

the shift values increased monotonically, as expected. For the sake of clarity in the far-field radiation patterns, only a subset of the results is plotted (0.00, 1.00, 2.00 and 2.67 mm).



(a) Standard design with unshifted rings yielding a single main beam directed along the boresight (maximum gain of 18.1 dBi).



(b) Design with shifted rings along the E-plane that deflects the single main beam by 20.0° (for a maximum gain of 13.5 dBi).

Figure 5.1: Illustration of how the Bull's eye antenna's main beam is deflected by shifting the centre of the rings along the E-plane (short side of the subwavelength aperture). Each subfigure shows a polar plot of linear gain above a perspective view of half of the antenna ©The Institution of Engineering and Technology 2016.

The E-plane radiation patterns are plotted in Figure 5.2. The deflection

Table 5.1: Angle deflection and gain for shifts in the E-plane.

Ring shift (mm)	0.00	0.50	1.00	1.50	2.00	2.50	2.67
Deflection angle (°)	0.00	5.10	9.90	12.7	15.4	18.4	20.0
Gain (dBi)	18.1	18.4	17.9	16.5	16.6	13.4	13.5

angle is approximately proportional to the *Shift* value, but the gain reduces from 18.1 dBi to 13.5 dBi due to a slight increase in power radiated by side-lobes, rather than a change in the beamwidth. Any secondary lobes remain below -10 dB, except when *Shift* = 2.0 mm in Figure 5.2, structure C, where an extra lobe at -25° rises at -6.8 dB. This is caused by a higher harmonic ($n = -2$) and can be predicted to occur at -27° with Equation 2.29. A similar phenomenon occurs at a smaller scale for structure D with an extra lobe at -17° and predicted to occur at -18° .

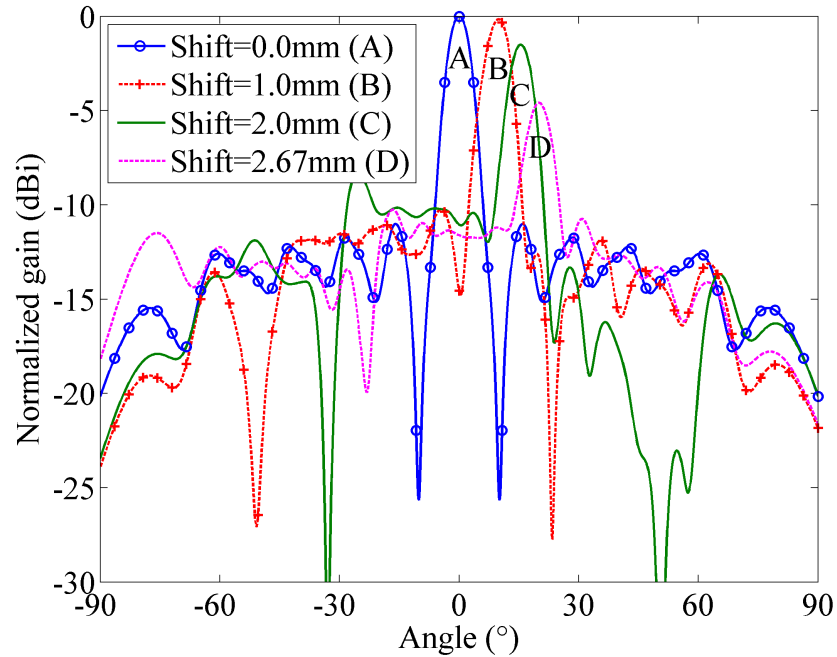


Figure 5.2: Plot of E-plane radiation patterns for an E-plane single shift ring structure for shifts of: 0.00 mm (A), 1.00 mm (B), 2.00 mm (C) and 2.67 mm (D)
 ©The Institution of Engineering and Technology 2016.

The H-plane shift has also been investigated. The corrugated structure remains the same, but the central region containing the aperture changes such that the direction of the shift is rotated by 90° . The radiation patterns for *Shift* = 0.00, 1.00, 2.00 and 2.67 mm is shown in Figure 5.3. The maximum

gain and the angle of deflection are listed in Table 5.2 as a function of the ring shift. These results show the flexibility of the antenna, in that shifts are possible in both the E-plane and H-plane. This also allows either polarisation to be used for a given beam deflection. At the maximum shift, the E-plane deflection is 3.9° larger than the H-plane, but at the penalty of 1.6 dBi. The differences in the E- and H-plane performance arise because the surface currents are not evenly distributed across the corrugated surface. This characteristic is further described and used in Section 5.2.

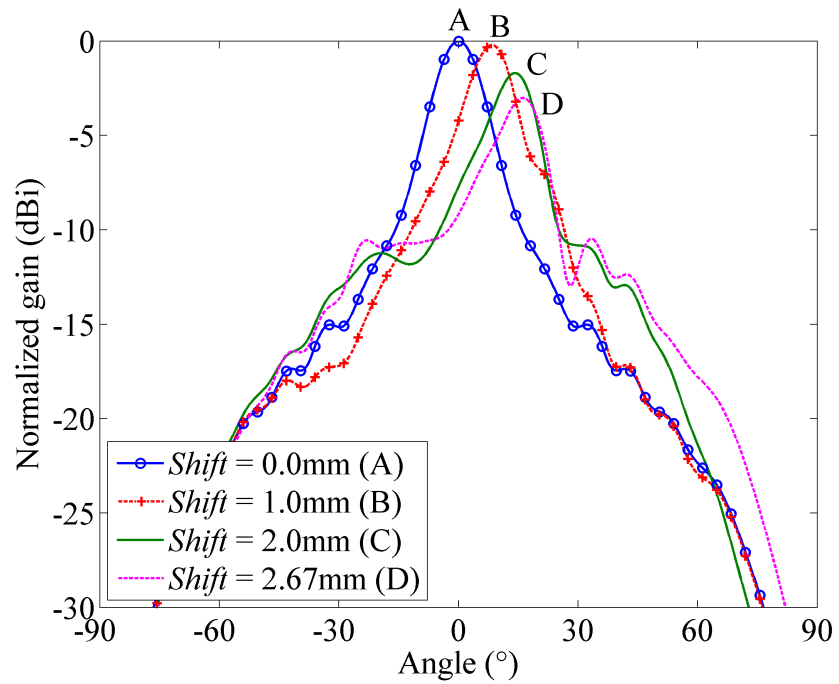


Figure 5.3: Plot of H-plane radiation patterns for H-plane single shift ring structure for shifts of: 0.00 mm (A), 1.00 mm (B), 2.00 mm (C) and 2.67 mm (D).

Table 5.2: Angle of deflection and gain according to single H-plane ring shift.

Ring shift (mm)	0.00	0.50	1.00	1.50	2.00	2.50	2.67
Deflection angle ($^\circ$)	0.00	3.40	8.40	11.8	14.2	15.6	16.1
Gain (dBi)	18.1	18.0	17.9	17.2	16.4	15.5	15.1

5.1.2 One dimensional grating model

The analysis was then extended to:

1. test how good a one-dimensional grating model is at predicting the performance of a Bull's eye antenna;
2. show the effect of the grating profile and filling factor (FF) on the coupling angle and;
3. demonstrate how close the local radiation angle, defined by the grating equation, is to the direction of the far-field beam.

To do so, two antennas are considered, including one with 50% FF pattern and period of 5.00 mm corresponding to the wavelength at 60 GHz, and another with the optimised values identified in Chapter 4. This allows separation of the effect of the optimisations from those intrinsic to the variations of the grating parameters. The canonical Bull's eye antenna refers to a Bull's eye antenna with a grating period equal to the wavelength, and the modified Bull's eye antenna is the optimised Bull's eye antenna studied in the previous Chapter.

Figure 5.4 shows a plot of the deflection angle from a canonical (unoptimised) and a modified (optimised) Bull's eye antenna, their equivalent one-dimensional gratings, and the deflection angle predicted for a grating of the same period using 2.29. The free space wavenumber is the black line, the canonical grating and antenna are the black markers, and the modified grating and antenna are the white markers. All five sets of results follow qualitatively the same trend. To emphasise the uniting role that leaky waves plays in governing all the results that are presented in Figure 5.4, the guided wave phase constant β is plotted using a colormap as a function of the effective grating period Λ , defined as the initial period Λ_0 plus the parameter *Shift* ($\Lambda = \Lambda_0 + Shift$), and the incident angle, by using the grating equation.

The guided wave (non radiative) has a phase velocity slightly lower than for free space ($\beta > k_0$ and $\beta \approx k_0$). The one-dimensional canonical grating (simulated by RCWA) is close to the free space wavenumber. The (unoptimised) canonical Bull's eye antenna with $\Lambda_0 = 5.00$ mm and FF = 0.50 to 0.33 (black circles) has a similar trend while showing discrepancies ranging from 0.7 to 3.0°, with an increasing trend visible from $\Lambda = 5.25$ to 6.50 mm, which is consistent with the loss of rotational symmetry. The deflection angle of the modified (optimised) grating with $\Lambda_0 = 4.53$ mm and FF = 0.41 to 0.26 (white square markers), and the deflection angle of the modified (optimised) Bull's eye antenna

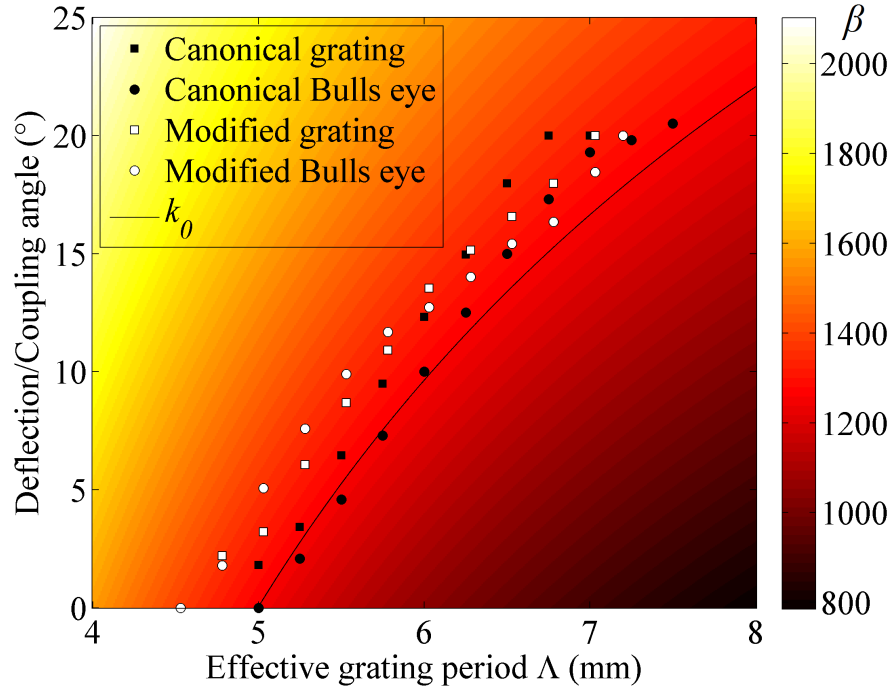


Figure 5.4: Plot comparing the simulated deflection angle of optimised (modified) and unoptimised (canonical) Bull’s eye antennas to the coupling angle of the associated one dimensional rectangular profile gratings, as a function of the effective grating period $\Lambda = \Lambda_0 + Shift$. The solid black line is the free-space wavenumber, and the colourmap shows how the coupling angle and the grating period relate to the surface wave phase constant ©The Institution of Engineering and Technology 2016.

with $\Lambda_0 = 4.53\text{mm}$ and $FF = 0.41$ to 0.26 (white circle markers) are plotted as white markers. The modified grating’s filling factor ranges from 0.41 to 0.26 , creating narrower ridges with higher spatial harmonics than the canonical structure. It is understood that β can vary slightly when the grating profile contains a significant amount of higher spatial harmonics [87], and this is expected to begin to strain the analogy to the one-dimensional gratings at smaller shift values. The reduction of the filling factor tends to increase the surface wave phase constant and consequently increase the deflection angle. This simplified analysis is a useful way to understand the operation of the antenna, and gives an efficient approach to predicting the performance of a Bull’s eye antenna, prior to optimising the structures using numerical simulations of the whole structure.

5.1.3 Multiple symmetrical beams

The possibility of generating multiple main beams with a Bull’s eye antenna is explored in this Section. This allows greater flexibility in future millimetre-wave communications systems where more than one link may be required simultaneously, yet with each individual link benefiting from a directive beam for power efficiency. Two schemes using independent ring patterns designed on each side of the antenna are investigated: symmetrical shift patterns that steer both beams equally, and asymmetrical patterns that deflect each beam by a different amount.

Two symmetrical structures have been investigated with rings shifted along the E- and H-planes. The first structure has its ring centres shifted within the E-plane for $Shift = 0.00, 1.00, 2.00$ and 2.67 mm. The simulation results are shown in Figure 5.5. Figure 5.5(1) shows the creation of two primary separate lobes, with deflection angle ranging from 0° to 18.6° .

The gain of each beam drops by 3 dB from 18.1 dBi for the single beam in the previous Section to 15.1 dBi for each of the two beams here. This is expected because the power is split equally between the two main beams, and the full efficiency is maintained overall. The secondary lobes stay below -8 dBi. Table 5.3 shows the deflection angle, the maximum gain and the -3 dB beamwidth within the E-plane as a function of $Shift$.

Table 5.3: Deflection angle, gain and beamwidth according to double E-plane ring shift ©The Institution of Engineering and Technology 2016.

Ring shift (mm)	0.00	1.00	2.00	2.67
Deflection angle ($^\circ$)	0.00	9.30	16.1	18.6
Gain (dBi)	18.1	15.3	15.6	15.1
-3 dB beamwidth ($^\circ$)	6.70	8.90	7.30	5.10

The H-plane double shift structure for $Shift = 0.00, 1.00, 2.00$ and 2.67 mm was then investigated. Figure 5.6 shows the radiation pattern for the structure.

Two main lobes are still created, but the separation is not as obvious as for the E-plane until $Shift \geq 2.00$ mm. Table 5.4 shows the deflection angle, the maximum gain and the -3 dB beamwidth within the H-plane according to the shift of the rings. Hence, the E-plane is preferable if double lobes are required.

Since it was previously established that the shifted half of the E-plane pattern predominantly determines the beam properties, it is expected that two different patterns can be combined to create beams that are deflected by different amounts.

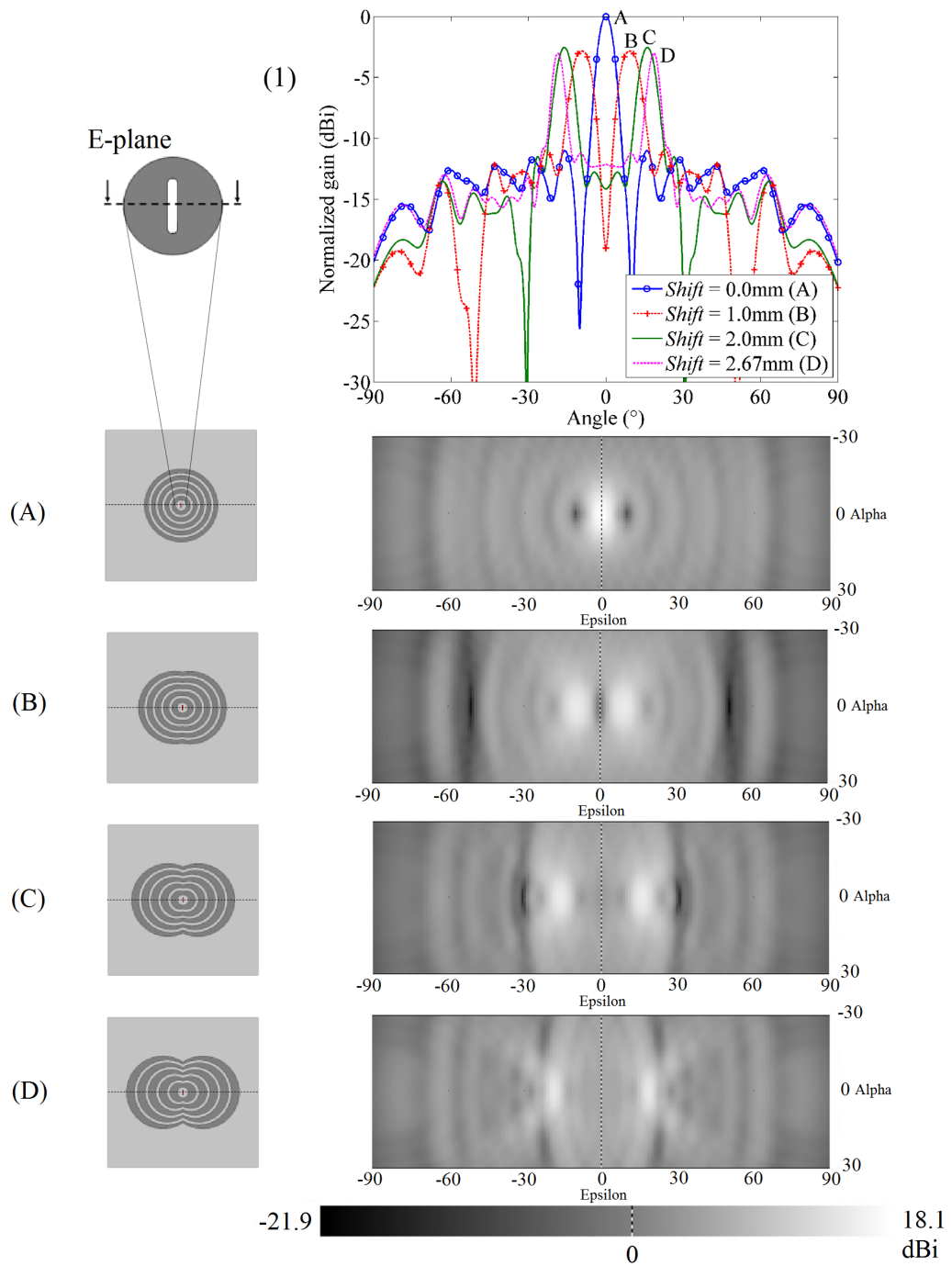


Figure 5.5: Plot of the E-plane radiation patterns (1); and E-plane double shift rings structure with corresponding 2D radiation pattern for shifts of 0.00 mm (A), 1.00 mm (B), 2.00 mm (C) and 2.67 mm (D) ©The Institution of Engineering and Technology 2016.

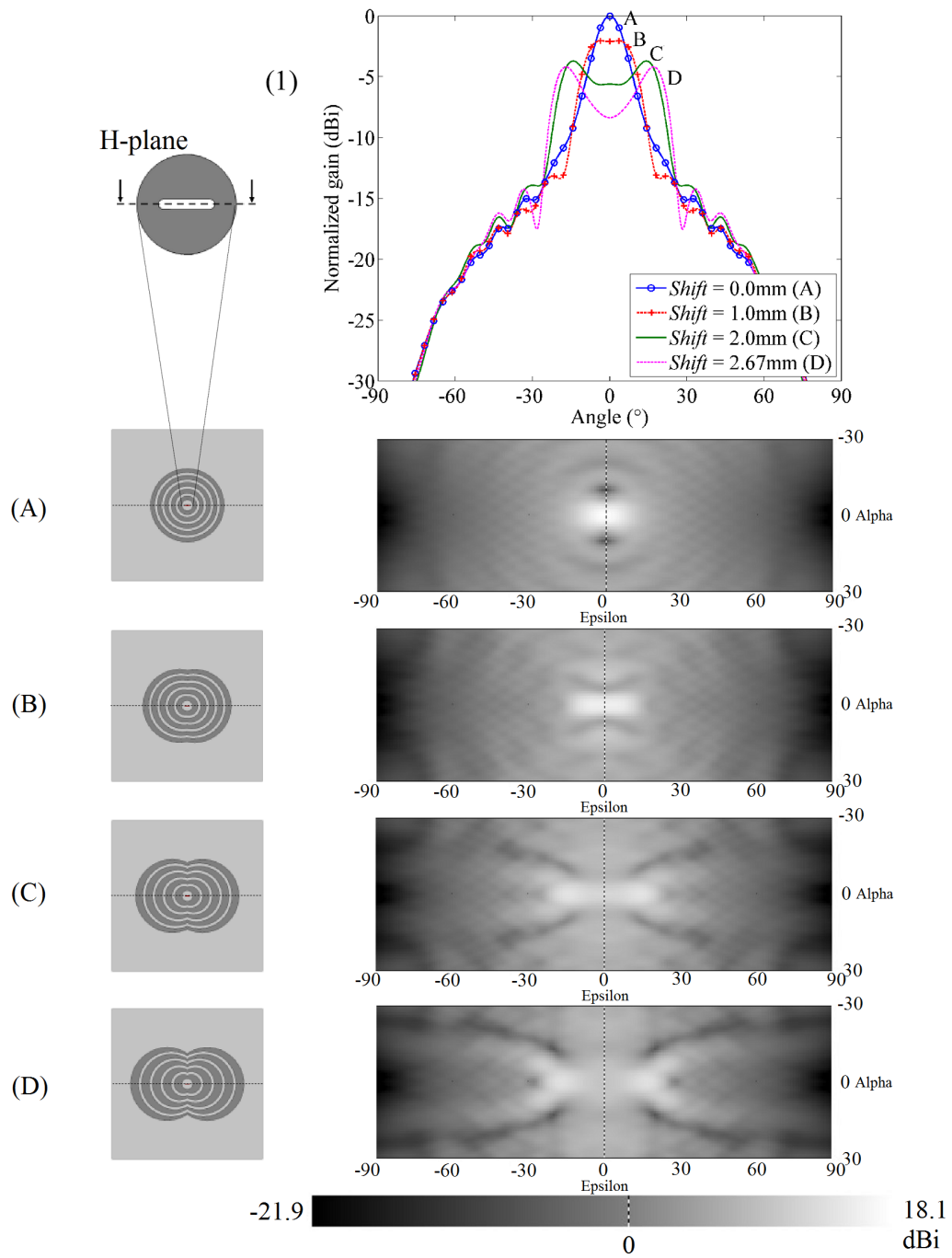


Figure 5.6: Plot of the H-plane radiation patterns (1); and H-plane double shift rings structure with corresponding 2D radiation pattern for shifts of 0.00 mm (A), 1.00 mm (B), 2.00 mm (C) and 2.67 mm (D) ©The Institution of Engineering and Technology 2016.

Table 5.4: Deflection angle, gain and beamwidth according to double H-plane ring shift ©The Institution of Engineering and Technology 2016.

Ring shift (mm)	0.00	1.00	2.00	2.67
Deflection angle (°)	0.00	3.30	14.3	17.0
Gain (dBi)	18.1	16.0	14.4	13.9
−3 dB beamwidth (°)	13.2	22.1	40.3	15.2

In other words, for E-plane shifts, each half of the pattern interacts with a different region of the surface current so it is expected the beam deflection to be independently adjustable. This is desirable because it simplifies the design of an antenna to meet an arbitrary specification. For example, the independence of the two beams is illustrated keeping one beam along the normal direction ($Shift = 0.00$ mm) and deflecting the other beam progressively, with offsets of $Shift = 0.00, 1.00, 2.00$ and 2.67 mm. Figure 5.7 shows the radiation patterns and plan view schematics of the ring patterns. The E-plane radiation patterns in Figure 5.7(1) show the deflection of the shifted lobe ranges from 0° to 21° . For the maximally shifted lobe at $Shift = 2.67$ mm, the maximum gain reduces to 10.1 dBi. On the other hand, the boresight lobe remains directed at angles between -0.5° and 1.6° . The gain of the lobe at boresight also drops from 18.1 dBi to 11.6 dBi, as shown in Figure 5.7(1). This is attributed to an interaction of the currents on each side of the aperture. This design was not further optimised, but there may be some value in investigating whether interactions between the two sides of the antenna are indeed the cause, and if so, to reduce them by blocking their path with small unpatterned guard bands, or trenches, between the two gratings.

5.1.4 Measurements

An E-plane double shift Bull’s eye antenna with $Shift = 2.00$ mm was manufactured to experimentally demonstrate that multiple beams can be created. The S_{21} parameter data was acquired with averaging of 10 points per sample and a 500 Hz IF bandwidth. Figure 5.8(a) shows a picture of the fabricated E-plane shift Bull’s eye antenna with $Shift = 2.00$ mm and Figure 5.8(b) shows the simulated and measured E-plane radiation patterns, after normalisation. It was expected that the lobes would be at $\pm 16^\circ$ from the boresight. Figure 5.8(b) shows close

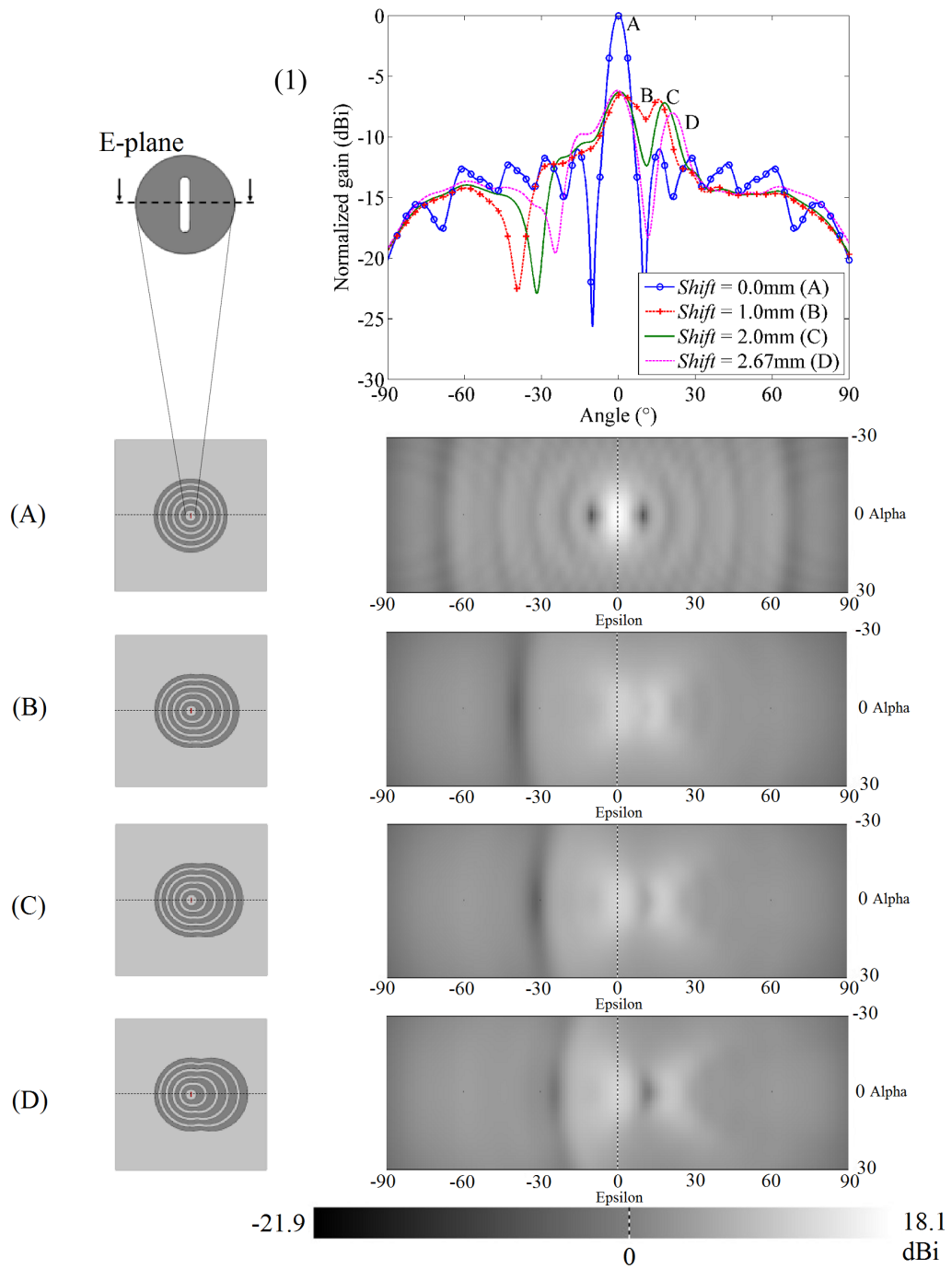


Figure 5.7: Plot of the E-plane radiation patterns (1); and E-plane asymmetrical shift rings structure with corresponding 2D projection radiation pattern for shifts of 0.00 mm (A), 1.00 mm (B), 2.00 mm (C) and 2.67 mm (D) ©The Institution of Engineering and Technology 2016.

agreement between the two normalized E-plane radiation patterns. The measured main lobe on the negative angle side is offset by -2° from the simulation, while there is close agreement in the location of the secondary lobes at $\pm 39^\circ$, $\pm 52^\circ$, $\pm 64^\circ$ and $\pm 80^\circ$, and nulls at $\pm 30^\circ$. The shift in the main lobe on the negative angle side is attributed to a systematic misalignment error in the measurement plane of the Bull's eye antenna.

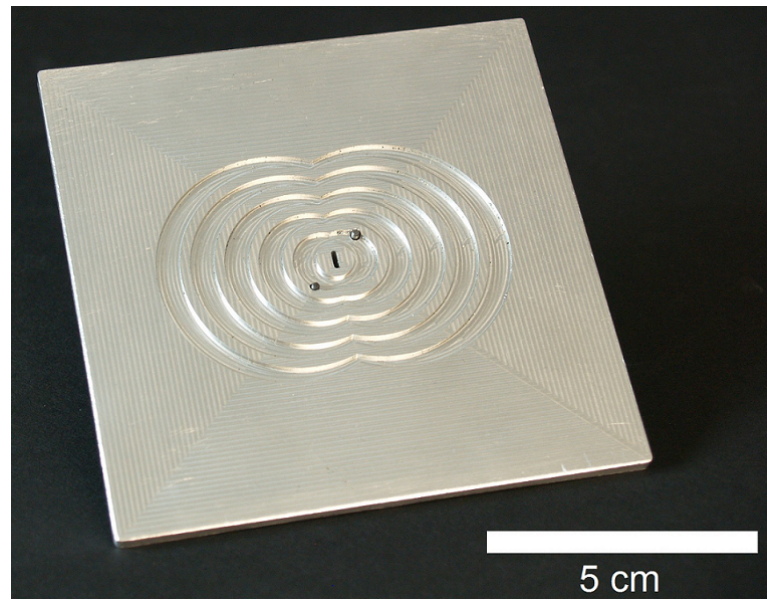
5.2 Sectorial Bull's eye antenna

This Section builds on the insights obtained so far, and explores the possibilities for beam steering achieved by mechanical means. Some millimetre-wave applications may require change in the main beam direction mainly to avoid interference and to increase the link budget by steering a narrow beam in a preferred direction so as to create an optimal RF link between a transmitter and receiver, which may be moving. The concept of a mechanical steering scheme based on sectorial division of the Bull's eye antenna's active area is first presented. Then, the simulation and measurement results of a three pair sectorial Bull's eye antenna are discussed.

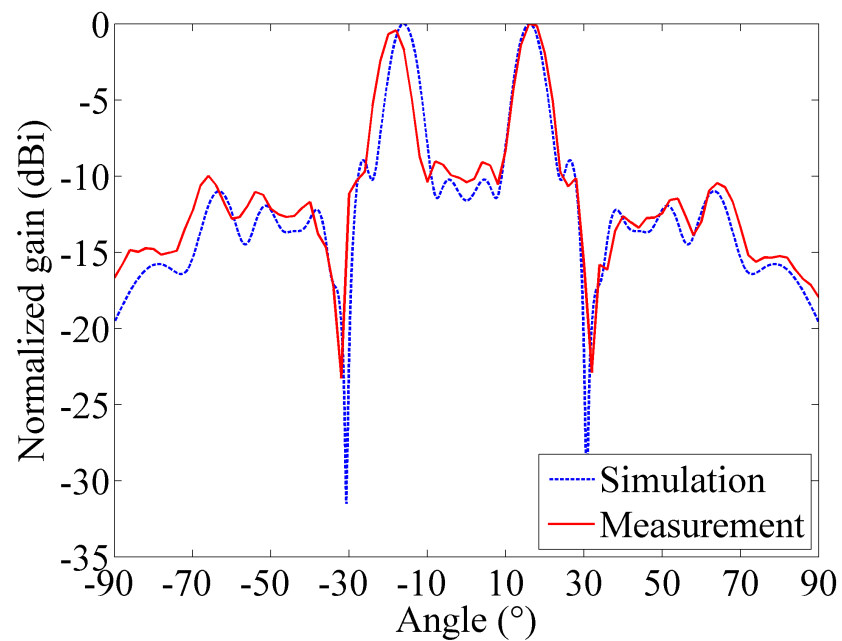
5.2.1 Steering concept

Having noted that surface current density was not uniform, an investigation was carried out to quantify the contribution of an angular sector to the radiation performance of the antenna, as a function of the angle subtended by the sector. The basic Bull's eye antenna with seven indented rings, described in the previous Chapter, was simulated with two additional masks placed on top of the corrugated surface. These masks were arranged in such a way that the uncovered active area was along the E-plane and parametrised with the variable α , being the angle subtended by the uncovered sector.

Figure 5.9 plots the simulation results for a Bull's eye antenna in which the surface area has been partially covered, such that the uncovered surface consists of two symmetrical circular sectors. Figure 5.9(a) shows the distribution of the electric field at the surface of the structure. Thus it appears as an uncovered but shaded region, the masked area is shown in transparency, highlighting the



(a)

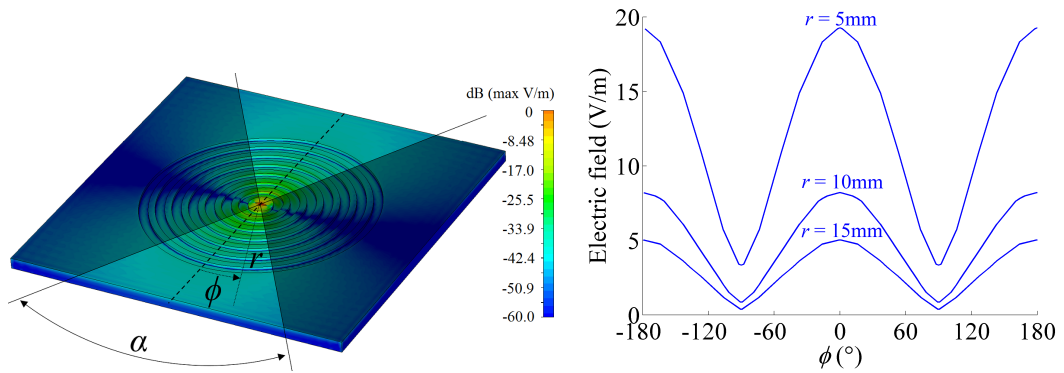


(b)

Figure 5.8: (a) Fabricated 2.00 mm E-plane double symmetrical shift Bull's eye antenna, (b) Normalized simulated and measured E-plane radiation pattern. The shift in the main lobe on the negative angle side is attributed to a systematic misalignment error in the measurement plane of the Bull's eye antenna. ©The Institution of Engineering and Technology 2016.

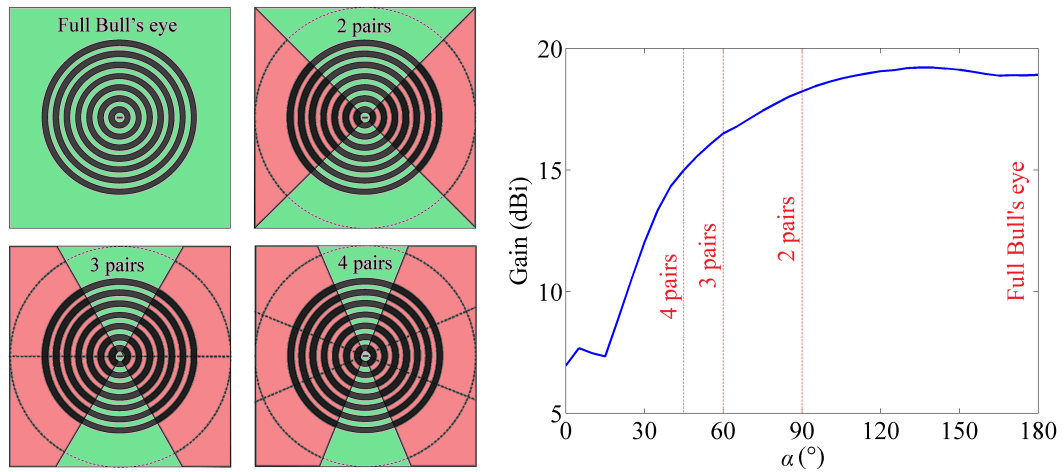
5.2 Sectorial Bull's eye antenna

uncovered sector defined with the variable α . The cylindrical coordinate system is defined with ϕ as the azimuthal coordinate and r as the radial coordinate.



(a) Plot of the distribution of the electric field at the surface of the structure. The covered area appears shaded because the covering mask has been made transparent so the currents electric field underneath can be evaluated.

(b) Plot of the electric field magnitude (V/m) as a function of ϕ , for $r = 5, 10$ and 15 mm.



(c) Top view of possible divisions of the surface area of a Bull's eye antenna in pairs symmetrical to the E-plane (two, three and four pairs), with active paired-sectors in green, and inactive paired-sectors in red.

(d) Gain of a Bull's eye antenna as a function of α , with particular values of gain for two, three and four pair divisions marked with vertical lines.

Figure 5.9: E-field distribution and gain (dBi) versus α ($^\circ$) representing the angular active area, for a Bull's eye antenna with seven indented rings.

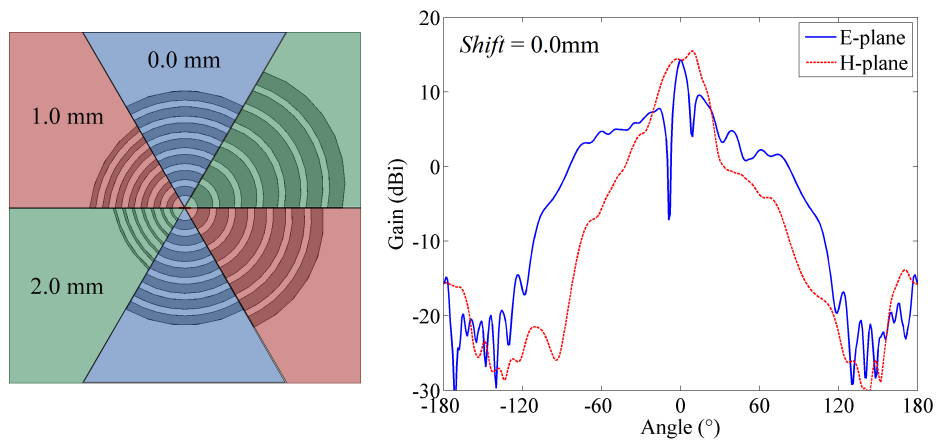
Figure 5.9(b) shows the electric field intensity as a function of ϕ for $r = 5, 10$ and 15 mm. Figure 5.9(c) illustrates possibilities for dividing the corrugated

area of a Bull's eye antenna into two, three or four pairs of patterns. For two pairs, the uncovered region subtends $\alpha = 90^\circ$, for three $\alpha = 60^\circ$ and for four pairs $\alpha = 45^\circ$. Figure 5.9(d) shows the gain of the antenna as a function of α , and highlighting the particular values for the full Bull's eye antenna, and for two, three, four and five pairs divisions. The intermediate values of α are plotted to confirm the overall behaviour is monotonic, but they would not be used in practice.

As shown in Figure 5.9(a,b), the electric field distribution at the surface of the antenna suggests that maximum intensity occurs along the E-plane, which is the area adjacent to the long sides of the sub-wavelength aperture ($\phi = 0^\circ$) whereas nulls occur along the H-plane ($\phi = 90^\circ$). In Figure 5.9(d), the gain increases with the angle subtended (α), reaching about half (-3 dB) of the maximum gain (19.2 dBi) when $\alpha \geq 60^\circ$. The gain ranges from 7.0 dBi for $\theta = 0^\circ$, corresponding to the gain of the subwavelength aperture alone, to 18.9 dBi for $\alpha = 180^\circ$, corresponding to the full, uncovered Bull's eye antenna. For two ($\alpha = 90^\circ$), three ($\alpha = 60^\circ$), and four ($\alpha = 45^\circ$) angular sectors, the gain is respectively 18.2, 16.5 and 15.0 dBi.

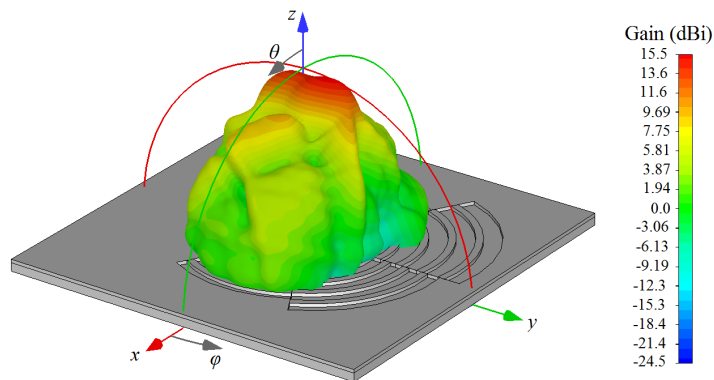
This possibility of dividing the corrugated zone in several different paired sectors is now considered. To illustrate this, the design of a sectorial Bull's eye antenna with three different paired sectors with single shift of $Shift = 0.0, 1.0$ and 2.0 mm was simulated in position $Shift = 0.0$ mm and the results are plotted in Figure 5.10. Figure 5.10(a) shows the plane-view of the corrugated area with the three sectors, Figure 5.10(b) shows the E- and H-field radiation pattern and Figure 5.10(c) shows the 3D far-field radiation pattern.

The asymmetrical corrugation pattern, with regard to the E-plane, alters the gain and the directivity for the radiation pattern, with a shift of the main beam direction in the H-plane radiation pattern by 9° , as shown in Figure 5.10(b). This can be solved by using a mask to ensure that the two unused paired sectors do not influence the beam pattern and therefore that full independence is achieved in a design with three different paired sectors. This solution is presented in the next Section and is implemented for the design of a steerable Bull's eye antenna.



(a) Top view schematic of the sectorial Bull's eye antenna in position $Shift = 0.0\text{ mm}$.

(b) Plot of the E- and H-plane far-field radiation pattern.



(c) Plot of the 3D far-field radiation pattern.

Figure 5.10: Simulation results for a Bull's eye antenna in position $Shift = 0.0\text{ mm}$ with three different paired sectors with single shift of $Shift = 0.0, 1.0$ and 2.0 mm .

5.2.2 Design and simulation

The design and simulation of a mechanically steerable Bull's eye antenna with three different sectorial pairs is presented in this Section. The antenna comprises four components, as shown in Figure 5.11. The bottom layer is a plate with sufficient thickness (5 mm) to accept the two UNC 4-40 threaded screws used to secure to the WR-15 waveguide flange. A straight-through waveguide section of $4 \times 2\text{ mm}^2$ cross section with 1 mm radius corners is milled into this plate, similar to the hollow waveguide presented in Chapter 4. The layer above is a 3.2 mm

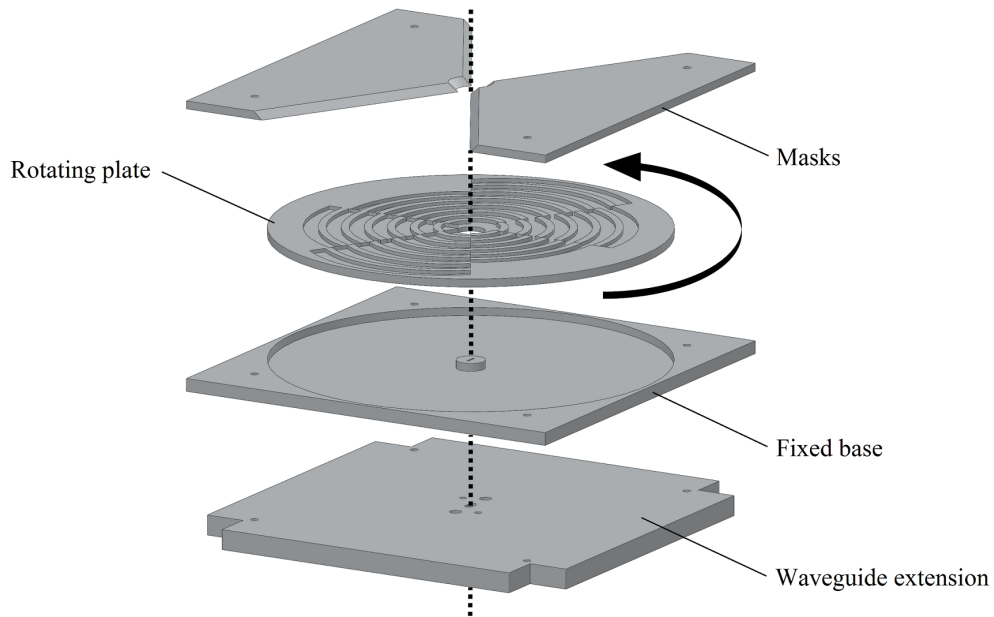


Figure 5.11: Exploded view the mechanically steerable sectorial Bull's eye antenna with three pairs of sectors showing from bottom to top: a waveguide extension, a fixed base, a corrugated rotating plate with three paired sectors and mask plates.

thick square plate that is hollowed out by a cylinder of inner radius 3.56 mm and outer radius 48 mm to a depth of just over 1.2 mm so as to accept the rotating corrugated plate. The corrugated plate is 1.2 mm thick, and divided into three pairs of opposing sectors, each subtending an arc of 60° . The top layer is a 1 mm thick mask. This thickness was chosen because it is the best practical compromise between rigidity, low profile and material availability of the masks. To illustrate the capabilities of the concept, a design with three pairs of sectors is proposed to produce a pattern with $Shift = 0.0$ mm to give a single beam along the boresight (0°); a double shift ($Shift = 1.0$ mm) for two beams, at $\pm 8^\circ$; and a double shift ($Shift = 2.0$ mm) for two beams, at $\pm 15^\circ$.

The prototype is rotated by hand, but the design was conceived to be readily mechanised. Further details of the motorised schemes are omitted because such as design is outside the scope of the Section.

5.2.3 Fabrication and measurements

All parts of the antenna were fabricated in 6082 aluminium alloy with a CNC milling machine at the mechanical workshop of the University of Glasgow. Figure 5.12 shows a photograph of the fabricated and assembled three-pair sectorial Bull's eye antenna in position $Shift = 2.0$ mm

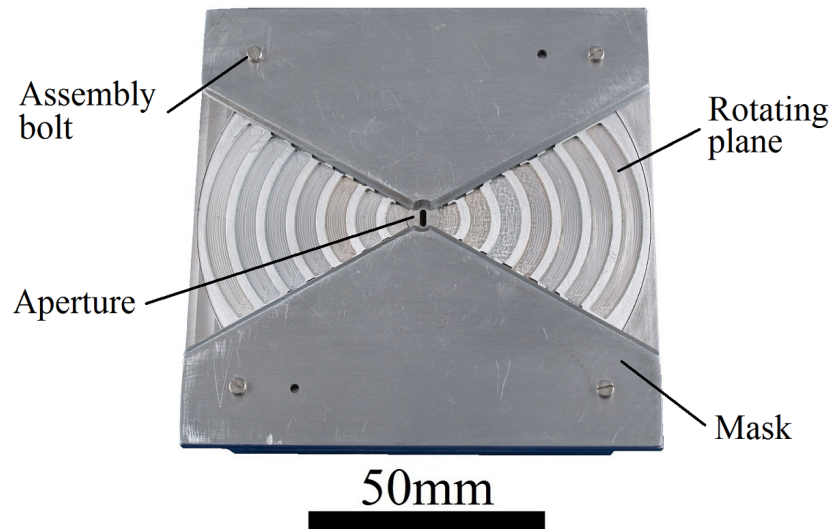
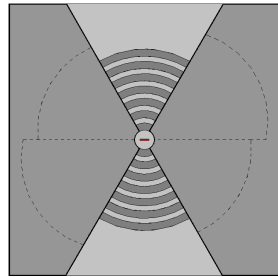


Figure 5.12: Top view of the fabricated and assembled three-pair sectorial Bull's eye antenna in position in $Shift = 2.0$ mm.

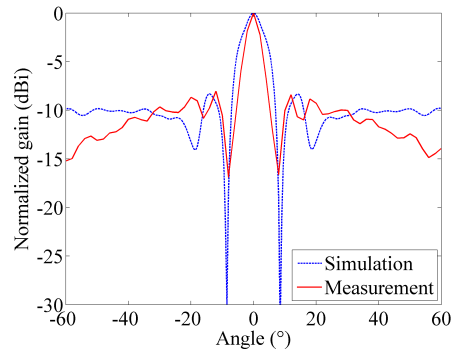
The radiation patterns from each of the three different pairs of sectors ($Shift = 0.0, 1.0$ and 2.0 mm) were recorded separately, from -60° to $+60^\circ$ in steps of 2° . Between each measurement, the mask was left in the place, and the corrugated plate was rotated by hand. Figure 5.13 shows the measured and simulated E-plane radiation patterns with top view of the corresponding sectorial Bull's eye antenna for $Shift = 0.0, 1.0, 2.0$ mm.

The simulated steering angle are $0^\circ, \pm 8^\circ$ and $\pm 15^\circ$, and the corresponding maximum gains are 16.3, 15.0 and 15.2 dBi for $Shift = 0.0, 1.0$ and 2.0 mm. The -3 dB E-plane beamwidths are $8.6^\circ, 6.7^\circ$ and 5.7° . The simulation and measurement results are in close agreement, except for two particular discrepancies. First, in Figure 5.13(a,b,c), the discrepancy of the secondary lobe level is attributed to the fabrication constraints, especially the width W of subwavelength aperture. A gain error of 5.62 and 2.48 dB at boresight for $Shift = 1.0$ and 2.0 mm is visible at boresight in Figure 5.13(b,c). The negative main lobe suffers from a shift toward negative angles of -3° for $Shift = 1.0$ mm and -2° for $Shift = 2.0$ mm.

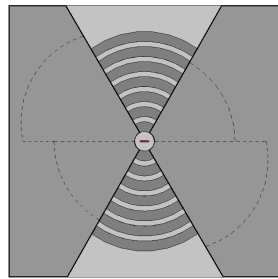
5.2 Sectorial Bull's eye antenna



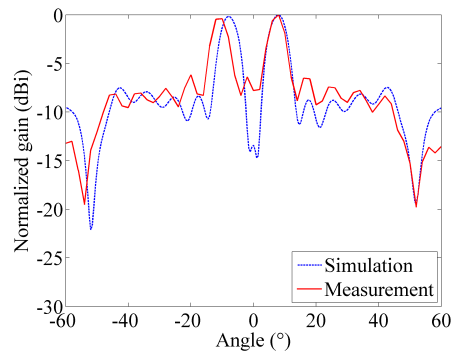
(a) Top view of the structure for $Shift = 0.0$ mm.



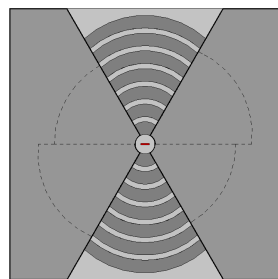
(b) E-plane radiation pattern for $Shift = 0.0$ mm.



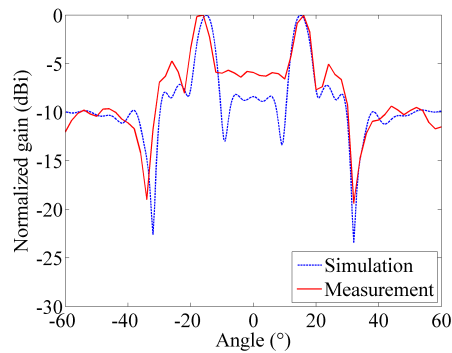
(c) Top view of the structure for $Shift = 1.0$ mm.



(d) E-plane radiation pattern for $Shift = 1.0$ mm.



(e) Top view of the structure for $Shift = 2.0$ mm.



(f) E-plane radiation pattern for $Shift = 2.0$ mm.

Figure 5.13: Simulation and measurement E-plane radiation patterns for three different configurations ($Shift = 0.0, 1.0$ and 2.0 mm) of the sectorial Bull's eye antenna. The shift in the main lobe on the negative angle side is attributed to a systematic misalignment error in the measurement plane of the Bull's eye antenna.

This is attributed to a systematic misalignment error in the measurement plane of the Bull's eye antenna, but is not a limitation of the design, as could already be seen in Figure 5.8.

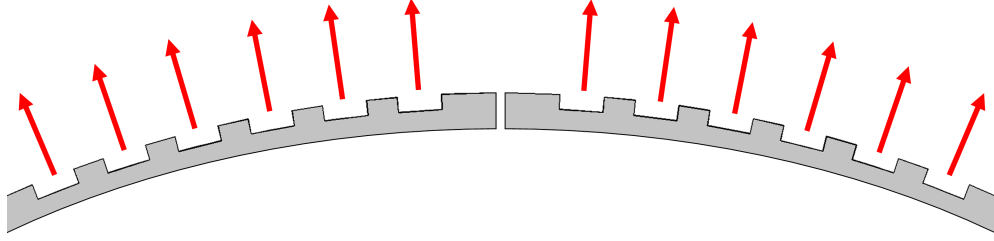
5.3 Conformal Bull's eye antenna

Some specific applications such as radar antennas in wings and nose cones may require conformal antennas to match curved surfaces, saving space and making them less visually invasive. Conformal leaky-wave antennas [88] are particularly adapted for automotive or defence applications where the aerodynamic drag has to remain minimal. Design rules are proposed in this Section for convex conformal implementations of the design presented in Chapter 4. A loss of directivity is expected to arise from a curved Bull's eye antenna with constant grating because each corrugation contributes to the radiation pattern with a different angle with respect to the boresight. This notional behaviour is illustrated in Figure 5.14 for a curved Bull's eye antenna showing the direction of a leaky wave emitted from a curved surface with a constant grating and an adjusted grating.

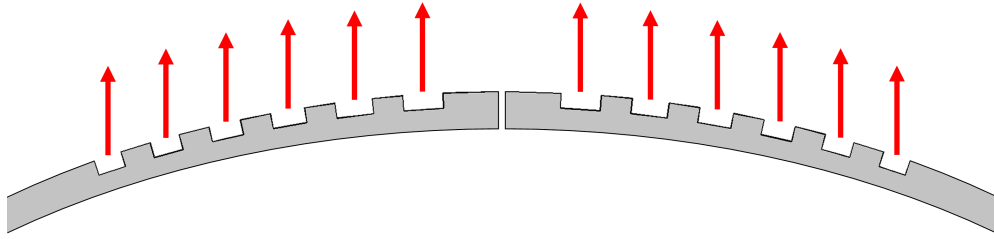
5.3.1 Conformal Bull's eye antenna with constant grating

To highlight the effect of the surface curvature on the Bull's eye antenna's performance, a first structure with six indented rings and constant grating period with $\Lambda = 4.53$ mm was simulated. This structure was designed so as to conform with a cylindrical curved surface of radius $R = 75$ mm along the E-plane. This plane was chosen because this is where the electric field distribution is strongest. Figure 5.15(a) shows a top view of the conformal Bull's eye antenna with constant grating and Figure 5.15(b) shows the simulated E- and H-plane radiation patterns.

The E-plane -3 dB beamwidth of the conformal Bull's eye antenna with constant grating is as high as 22.0° which reflect the loss in directivity of the antenna. This results in a peak gain of 13.1 dBi, which is about 6 dB lower than a flat Bull's eye antenna with six indented rings, as reported in Table 1 of Chapter 4.



(a) Schematic illustrating the direction of the waves leaking from a Bull's eye antenna with a constant grating.



(b) Schematic illustrating the diverging direction of the waves leaking from a curved Bull's eye antenna with an adjusted grating.

Figure 5.14: Cut view showing the parallel direction of a leaky wave emitted from a curved Bull's eye antenna with (a) a constant grating and (b) an adjusted grating.

5.3.2 Model for a conformal Bull's eye antenna with adjusted grating

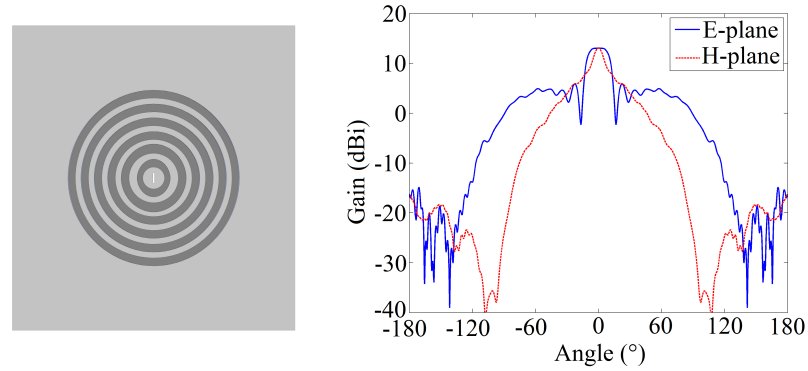
The model for adjusting the grating dimensions of a Bull's eye antenna with a curved cylindrical surface along one plane is now introduced. The grating equation, giving the relationship between surface wave phase constant β , the radiation angle θ_{rad} , and the period of the grating Λ of the n^{th} harmonic, can be locally written as:

$$\beta = k_0 \sin(\theta_{rad} - \theta_{zn}) + \frac{2\pi}{\Lambda_n}, \quad (5.1)$$

where θ_{zn} is the angle formed between the boresight of the antenna and the normal of the antenna surface at the n^{th} period, as shown in Figure 5.16.

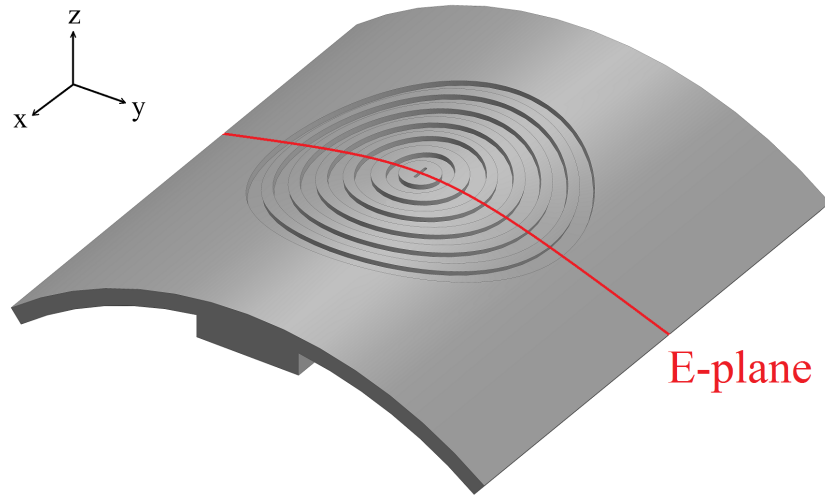
The surface wave propagates along the curved surface, as it would a planar surface. Therefore, for a radius of curvature R of the outer layer, each of the n^{th} corrugation periods Λ_n can be adjusted according to the desired radiation angle θ_{rad} . All the segments that constitute the model are either tangential or normal to the curves as shown in Figure 5.16. The depth of the corrugations is h and

5.3 Conformal Bull's eye antenna



(a) Plan view of a conformal Bull's eye antenna with constant grating dimensions.

(b) Radiation pattern for a conformal Bull's eye antenna with constant grating dimensions.



(c) Perspective view of the conformal Bull's eye antenna with constant grating dimensions.

Figure 5.15: Illustration of the loss of directivity for a conformal Bull's eye antenna with constant grating $\Lambda = 4.53$ mm along the E-plane.

the radius of aperture corrugation is $D_c/2$. The arc of radius $R_{avg} = R - h$ is defined as the arc that is concentric to the outer layer of curvature R . The path of length s_n along the curve of radius R_{avg} is defined as the sum of the radius of aperture corrugation $D_c/2$ and the subsequent grating periods Λ_n :

$$s_n = \frac{D_c}{2} + \sum^n \Lambda_n, \quad (5.2)$$

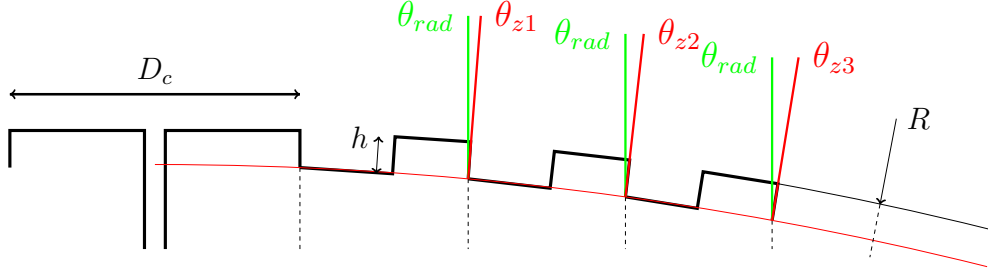


Figure 5.16: Schematic view of the conformal Bull's eye antenna dimensions for the model.

The pattern of the n^{th} transition between an indented and a raised ring on the curved surface is defined as a projected ellipse of major axis a_n and minor axis b_n on the curved surface. The dimensions of the n^{th} ellipse marking the transition between two periods (from raised to indented, in this order) are given by

$$a_n = R_{avg} \sin \left(\frac{s_n}{R_{avg}} \right), \quad (5.3)$$

with

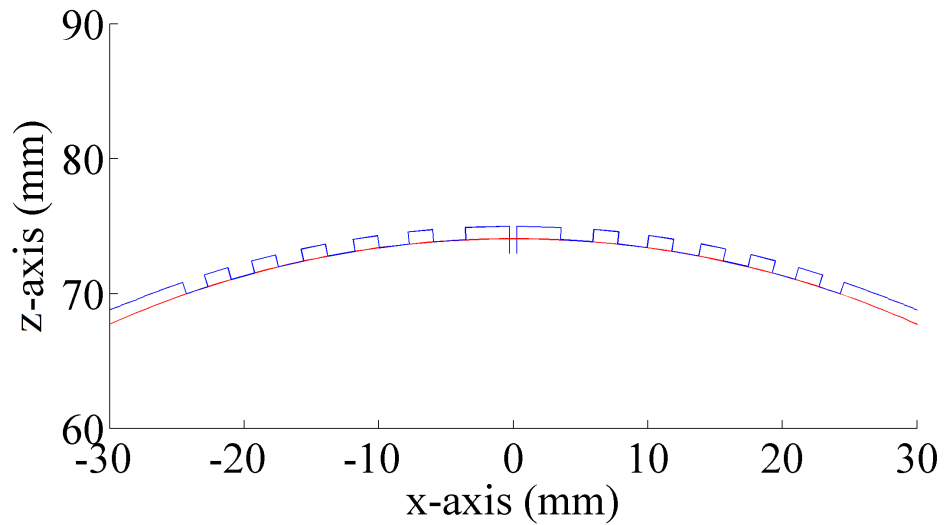
$$s_n = \frac{D_c}{2} + \sum_{n=1}^n \Lambda_n, \quad (5.4)$$

where s_n is the curved path length from the centre of the Bull's eye antenna to the n^{th} period,

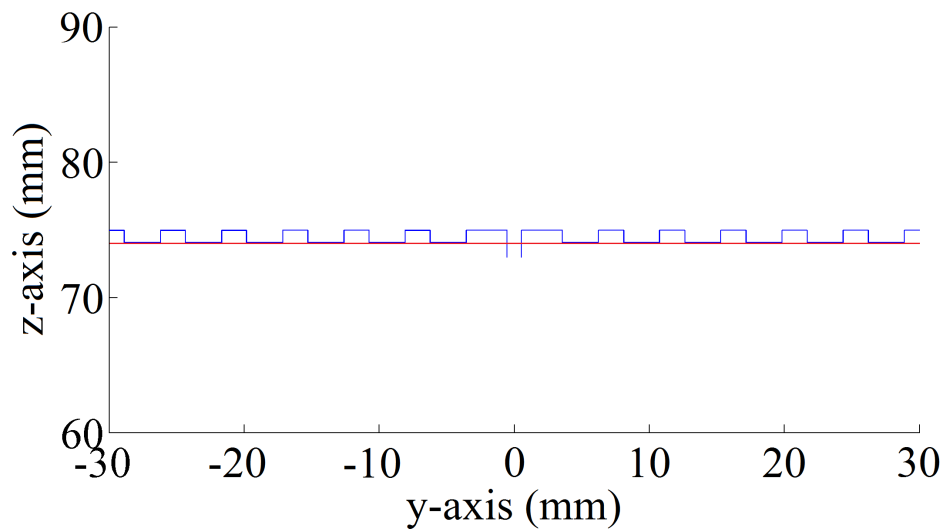
$$b_n = \frac{D_c}{2} + \sum_{n=1}^n \Lambda_0, \quad (5.5)$$

where $\Lambda_0 = 4.53$ mm.

The period Λ_n as a function of the angle θ_{zn} is determined according to the simulation results from Section 1.1.2. The adjustment of the grating profile follows the same scheme which consist of keeping the raised ring dimensions identical and adjusting the indented ring dimensions. The model was implemented to calculate the grating dimensions of a conformal Bull's eye antenna with six indented rings and with a cylindrical curvature R along the E-plane of 75 mm. The periods of the adjusted successive grating were calculated to be, outer to inner: 4.30, 4.11, 3.94, 3.79, 3.66 and 3.55 mm. Figure 5.16(a,b) shows the cut view of the Bull's eye antenna obtained with the model described in this Section.



(a) Schematic cut of the E-plane profile model.

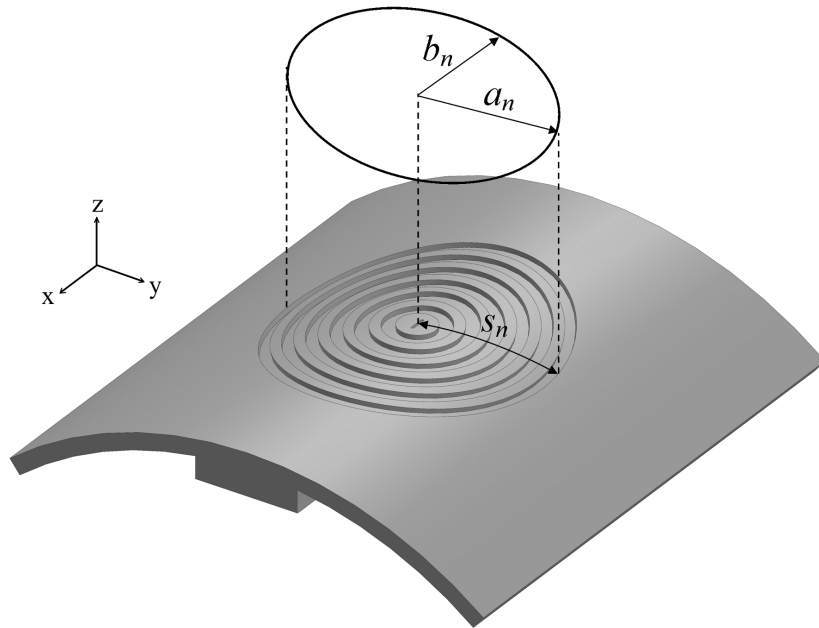


(b) Schematic cut of the H-plane profile model.

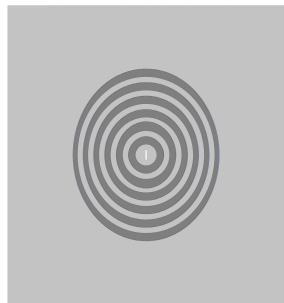
Figure 5.17: Modelled cut view of a conformal Bull's antenna model with a radius of curvature $R = 75$ mm.

The design of the Bull's eye antenna was then simulated and the results for the E-plane and H-plane radiation patterns are plotted in Figure 5.18(b,c).

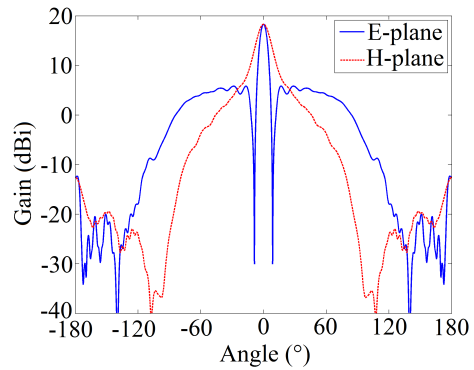
The Bull's eye antenna with an adjusted grating reaches 18.3 dBi which constitutes an improvement of 5.2 dB compared to the version with constant grating dimensions, and only a decrease of 0.8 dB compared to a flat Bull's eye antenna. The E-plane -3 dB beamwidth is improved by 15.6° at 6.4° which illustrate the gain in directivity induced by adjusting the grating period following the proposed



(a) Perspective view of the conformal Bull's eye antenna with adjusted grating dimensions illustrating the projection of ellipse of major axis a_n and minor axis b_n on the curved surface.



(b) Plan view of the conformal Bull's eye antenna with adjusted grating dimensions.



(c) Radiation pattern for the conformal Bull's eye with adjusted grating dimensions.

Figure 5.18: Illustration of the convex conformal Bull's eye antenna with adjusted grating dimensions along the E-plane for the $R = 75$ mm, and simulated E- and H-plane radiation patterns.

model.

This clearly illustrates the effect of adjusting the grating period along the curved plan to maintain a high directivity.

5.4 Chapter summary

This Chapter explored the enhancements of the 60 GHz Bull's eye antenna design presented in the previous Chapter. First, beam deflection was investigated using a straightforward ring shift scheme. The effect of shifting the rings was consistent with the expected coupling angle between a surface wave travelling on a periodic grating and free space, where the period is modified according to a specific ring shift scheme. The study was then extended to designs giving multiple deflected beams. The rings are split and shifted in more than one direction, exploiting the localised nature of the leaky waves. A dual beam antenna was designed, fabricated and measured. Then, a mechanically steerable Bull's eye antenna was designed, fabricated and measured. The antenna relied on a rotating plate containing different ring patterns, which is selectively masked by a fixed overplate, so that one set of rings is exposed at a time. This approach is desirable for communications in slowly-varying environments where the link budget is tight, and maximum efficiency is required so as to meet range or signal-to-noise requirements. Subsequently, a conformal Bull's eye antenna was presented which could achieve 18.3 dBi when deformed on a radius of 75 mm. The key developments in this Chapter are highlighted in Figure 5.19. Since our expected applications will most likely use line of sight links, a mean of enhancing the spectral efficiency is investigated next.

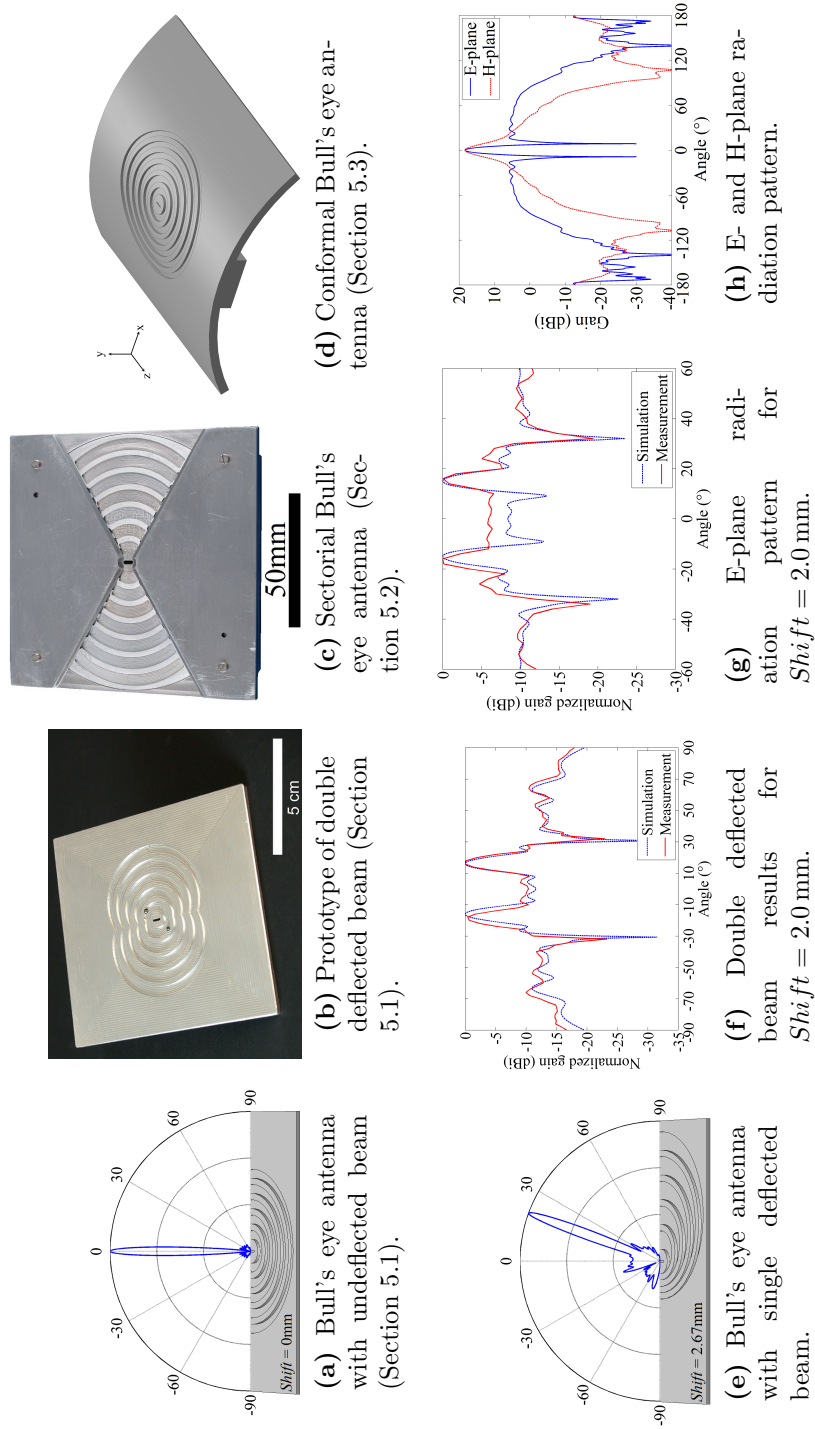


Figure 5.19: Summary of the results presented in Chapter 5.

Chapter 6

Orbital angular momentum generated by Bull's eye antenna

Orbital angular momentum (OAM) modes received considerable attention in the optical domain, where they facilitate applications such as optical tweezing [89] and enhanced communication data rates [90]. A similar benefit is expected to be obtained at radio frequencies, within the limits imposed by the nature of the OAM modes. Linear and circularly polarised signals, where circular polarisation can be viewed as spin angular momentum (SAM), can be detected at a single point, whereas OAM is only apparent when sampled over a non-singular sized aperture.

OAM modes can be mutually orthogonal, so it is possible to multiplex signals and hence, obtain enhanced spectral efficiency by sending multiple channels in the same frequency domain. For example, recent investigations using four OAM modes already showed millimetre-wave transmission at 32 Gbit/s over a distance of 2.5 m [91]. As a beam carrying non-zero OAM inevitably diverges when propagating, the receiving aperture can become particularly large at radio frequencies. This feature makes the advantage of using OAM multiplexing over other multiplexing methods still debatable [92]. Nonetheless, OAM multiplexing is still worth investigating for short distance applications using the 60 GHz band. To achieve OAM multiplexing designs at millimetre-wave frequencies, two main areas of improvement were identified to advance the state of the art:

1. Develop directive, low profile, and versatile OAM antenna designs for multiple, orthogonal OAM mode generation.
2. Improve receiving schemes for OAM multimode by using partial apertures that are discretely sampled.

In this Chapter, the properties of electromagnetic waves carrying non-zero OAM are first described in terms of Laguerre-Gaussian (LG) modes. The generation of electromagnetic waves carrying OAM with a low profile OAM Bull's eye antenna is then investigated. A novel design, based on a circular travelling-wave resonator surrounded by a corrugated leaky wave structure, and generating two simultaneous OAM modes, is proposed. Then an improved version of this design is presented, allowing the generation of four simultaneous and orthogonal OAM modes. After studying orthogonality conditions for a continuous receiving aperture, a specific scheme based on discrete receivers arranged along a partial aperture is proposed.

6.1 Orbital Angular Momentum

An electromagnetic wave can carry energy but also linear and angular momentum. The angular momentum can be decomposed in two parts: spin angular momentum (SAM) and orbital angular momentum (OAM). SAM is related to the state of circular polarisation and can only take two values of opposite sign corresponding to the left or right hand circular polarisation. OAM is related to the spatial distribution of the electromagnetic wave and has an azimuthal phase dependence of $\exp(il\phi)$, where l is an integer corresponding to the OAM state, or OAM mode number, and ϕ is the transverse azimuthal angle. The typical spatial distribution of an electromagnetic wave carrying a non-zero OAM mode ($|l| > 0$) is illustrated in Figure 6.1 and shows a distinct helical wavefront along the direction of propagation with a phase singularity on boresight.

More specifically, the field distribution of a beam carrying OAM can be represented with a Laguerre-Gaussian (LG) modal decomposition in a cylindrical coordinates system (r, ϕ, z) , with a radial mode index p and azimuthal mode

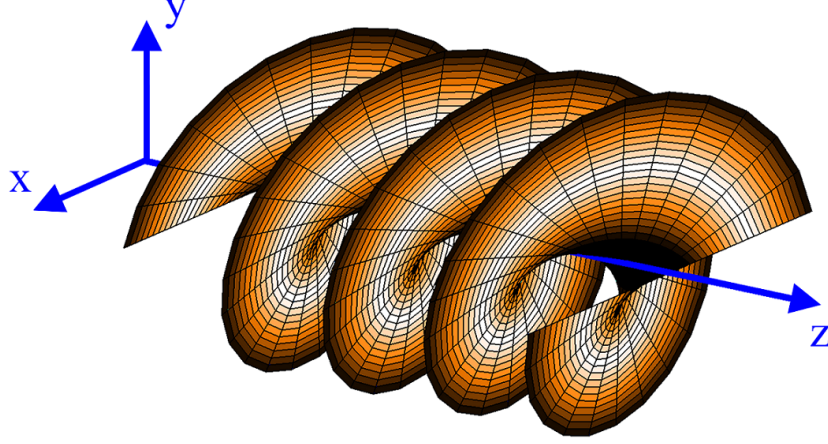


Figure 6.1: Illustration of the helicoidal wavefront of an electromagnetic wave travelling along the z -axis and carrying OAM mode $|l| > 0$.

index l [93]:

$$\begin{aligned}
 LG_p^l(r, \phi, z) &= \frac{C}{\sqrt{1 + (z^2/z_R^2)}} \left(\frac{r\sqrt{2}}{w(z)} \right)^{|l|} L_p^{|l|} \left(\frac{2r^2}{w^2(z)} \right) \\
 &\times \exp \left(\frac{-r^2}{w^2(z)} \right) \exp \left(\frac{-ikr^2z}{2(z^2 + z_R^2)} \right) \exp(il\phi) \\
 &\times \exp \left(i(2p + |l| + 1) \arctan \frac{z}{z_R} \right), \tag{6.1}
 \end{aligned}$$

where C is a constant, $z_R = \frac{\pi w_0^2}{\lambda}$ is the Rayleigh length, w_0 is the beam waist, $w(z)$ is the beam radius, and $L_p^{|l|}(x)$ are the generalised Laguerre polynomials expressed as:

$$L_p^{|l|}(x) = \sum_{i=0}^p \binom{p + |l|}{p - i} \frac{(-x)^i}{i!}, \tag{6.2}$$

where $L_p^{|l|}(x) = 1$ for a single radial mode ($p = 0$).

Figure 6.2 illustrates the magnitude and phase calculated with Equation 6.1 on an $80 \times 80 \text{ mm}^2$ plane, at $z = 50 \text{ mm}$ above the source, for OAM modes $l = 0$ (a,c), $+1$ (b,d) and $+2$ (e,f) at 60 GHz. Figure 6.2(a,b) shows the electric field magnitude and phase for an electromagnetic wave with a zero OAM. Figure 6.2(c,e) shows the typical annulus shape of the electric field magnitude for a electromagnetic wave with a non zero OAM. Figure 6.2(d,f) shows the helical

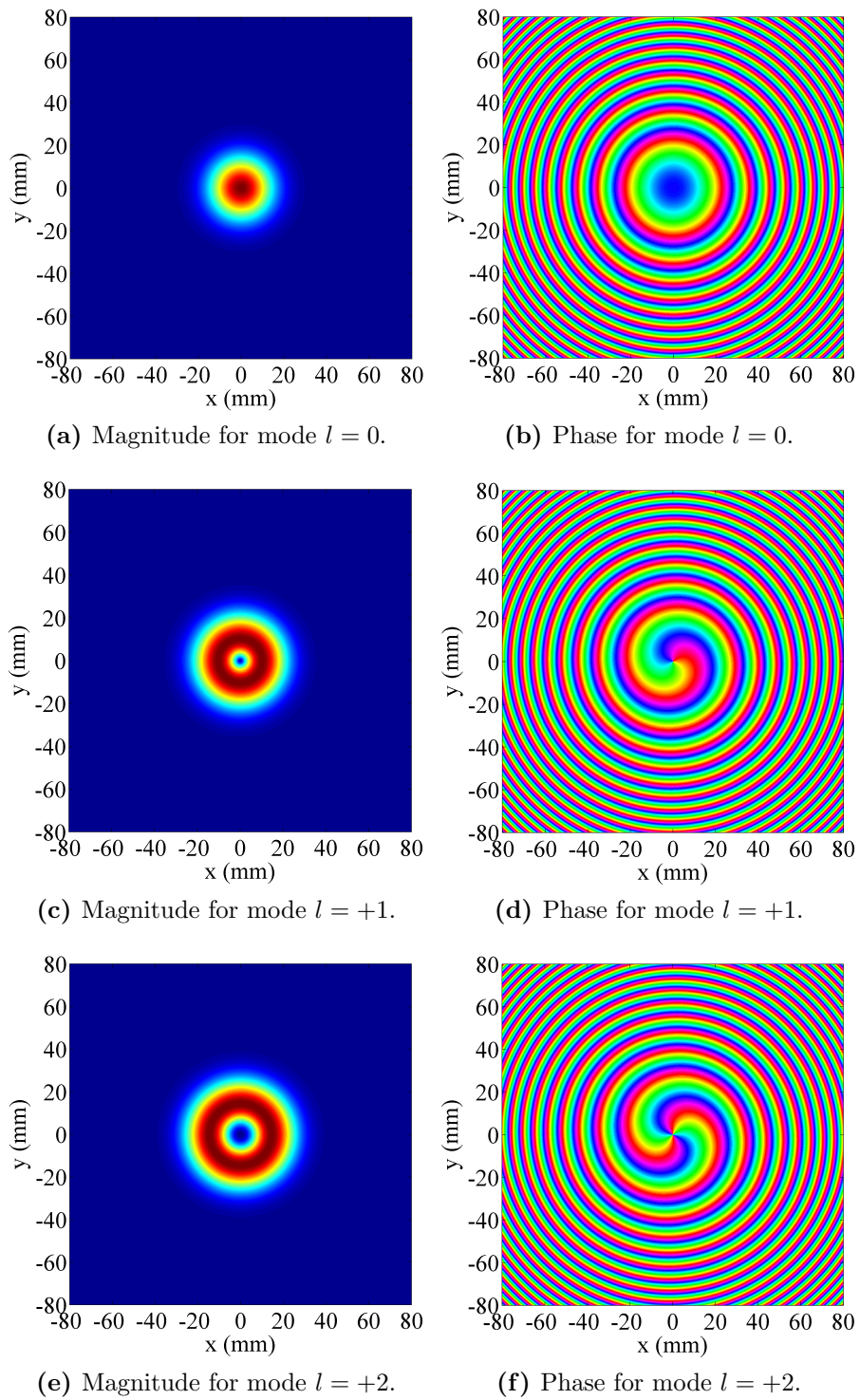


Figure 6.2: Magnitude and distribution of the electric field on a $80 \times 80 \text{ mm}^2$ plane, 50 mm above the source, for OAM modes $l = 0$ (a,b), $+1$ (c,d) and $+2$ (e,f) at 60 GHz.

phase front for $l = 1$ and $l = 2$ showing the accumulation of $2\pi l$ of phase around boresight.

The use of OAM modes can theoretically provide an infinite number of states into which information can be encoded because the OAM mode value l is unbounded. For these reasons, using OAM modes as a multiplexing method can increase the number of available channels and the overall throughput capacity.

6.2 Bull's eye antenna for OAM generation

The design of a low profile and high directivity antenna generating electromagnetic waves carrying non zero OAM is key for versatile use in short distance OAM multiplexing applications. The Bull's eye antenna is attractive for OAM mode generation because it is lower profile than existing alternatives. These include methods of the Spiral Phase Plate (SPP) [94], the Pitch-Fork hologram [95] and the Q-plate [96]. At millimetre-wave frequencies, these methods are often applied in conjunction with a horn antenna which results in a bulky system. In this Section, the design of an OAM Bull's eye antenna based on a circular travelling-wave resonator, producing two simultaneous OAM modes, is first presented. Then, a stacked version of the OAM Bull's eye antenna is designed so as to produce multiple, orthogonal OAM modes.

6.2.1 Single OAM Bull's eye antenna

The OAM Bull's eye antenna presented here has a similar corrugated structure to the one studied in Chapter 4, but the feed is modified to produce electromagnetic radiation carrying non-zero OAM modes. Hui *et al.* [97] generate OAM modes with a circular travelling-wave resonator, fed with two orthogonal waveguide ports with a 90° phase shift. The same circulating resonator is reused here, optimised and adapted to take advantage of the very low profile of the corrugated Bull's eye structure operating at 60 GHz. The average radius r_{avg} of a circular travelling wave resonator can be calculated as:

$$r_{avg} = \frac{|l|}{\pi \sqrt{\left(\frac{2}{\lambda}\right)^2 - \left(\frac{1}{a}\right)^2}}, \quad (6.3)$$

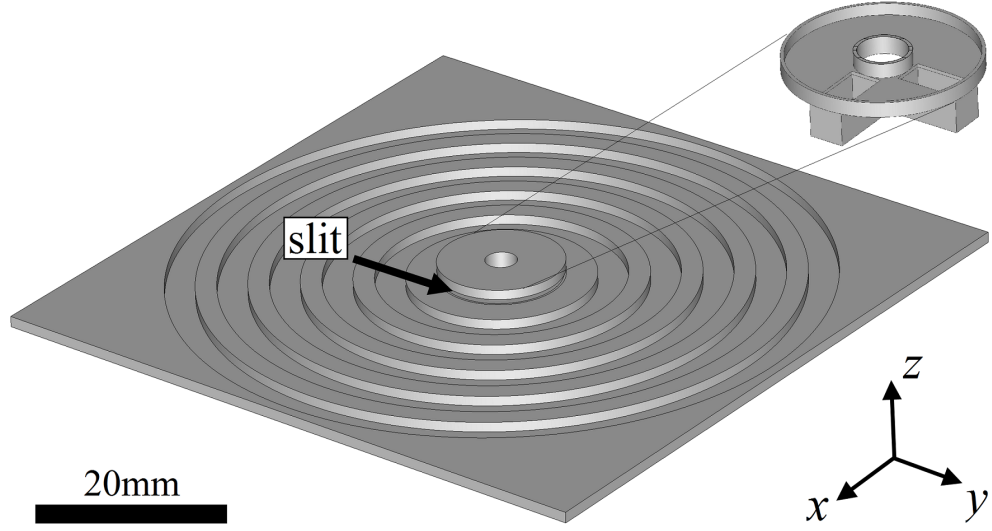
6.2 Bull's eye antenna for OAM generation

where l is the OAM mode to generate, λ is the wavelength and a is the width of the waveguide. For a frequency of operation centred about 60 GHz, the width a and the height b of the circular travelling wave resonator are chosen to be identical to the dimensions of standard WR-15 waveguide with $a = 3.76$ mm and $b = 1.88$ mm. The OAM modes then leak from the circular travelling wave resonator via a continuous slit in its narrow outer wall of height s . The inner radius is expressed as $r_{in} = r_{avg} - a/2$, and the outer radius as $r_{out} = r_{avg} + a/2$. These dimensions constrain the minimum possible OAM mode to $|l| \geq 3$ because r_{in} becomes too small otherwise. Hence, $|l| = 3$ was chosen for the design of the OAM Bull's eye antenna. As presented by Hui *et al.* [97], a waveguide 90° hybrid coupler is designed to generate the two opposite OAM modes $\pm l$ when the two input ports are excited simultaneously. The design of this part is not investigated further in this Section.

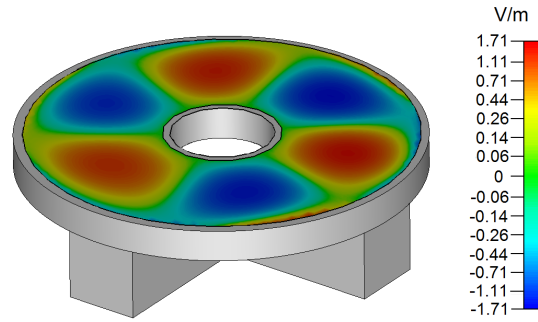
The circular travelling wave resonator is surrounded by a Bull's eye antenna which is made of a corrugated surface following the dimensions described in Chapter 4 so as to radiate ideally on boresight. The first indented ring is placed at a distance l_{off} from the outside wall of the resonator. A perspective view of the design with five indented rings is shown in Figure 6.3(a). The travelling wave ring and the electric field distribution are showed in detail in Figure 6.3(b), highlighting the three wavelengths along the circular transverse path for OAM modes $l = \pm 3$.

The simulation of the proposed design was carried out with CST MWS's time domain solver as already introduced in Chapter 3. The open boundaries were spaced 50 mm (about 10λ) from the structure, so as to visualise the electromagnetic field distribution. The dimensions of the circular travelling wave resonator were first calculated with Equation 6.3 for $l = \pm 3$, then optimised with simulations to obtain best performance at 60 GHz. The optimised dimensions were expected to slightly vary from the one calculated from Equation 6.3 because the slit affects the frequency of resonance of the structure. The simulated model of the circular travelling wave resonator has an inner radius of $r_{in} = 1.62$ mm, an outer radius of $r_{out} = 5.38$ mm, an height of $b = 1.88$ mm and a slit of $s = 0.5$ mm. It is fed by two WR-15 waveguide ports so as to create two orthogonal OAM modes of $l = \pm 3$. The resonator is surrounded by a Bull's eye antenna, with the first indented ring spaced by $l_{off} = 2.71$ mm. These dimensions are illustrated in Figure 6.4 and summarised in Table 6.1.

6.2 Bull's eye antenna for OAM generation



(a) Perspective view of the full OAM Bull's eye structure ©2016 The Institution of Engineering and Technology.



(b) Cut away view of the circular travelling wave resonator showing the magnitude of the E-field (z-component).

Figure 6.3: Perspective view of an OAM Bull's eye antenna with cut-away view of the central resonator for OAM mode $l = \pm 3$.

Table 6.1: Dimensions (mm) of the circular travelling wave resonator and surrounding Bull's eye antenna.

a	b	r_{in}	r_{out}	s	l_{off}	Λ	r_{ind}
3.76	1.88	1.62	5.38	0.5	2.71	4.53	2.67

The number of indented rings directly dictates the peak gain, and the null width defined as the angular distance between two gain maxima within a plane orthogonal the surface of the antenna. The simulated results for the OAM Bull's eye antenna for $l = \pm 3$ with zero to five indented rings are shown in Figure 6.5. For the OAM Bull's eye antenna with no rings, the maximum gain reaches 6.0 dBi

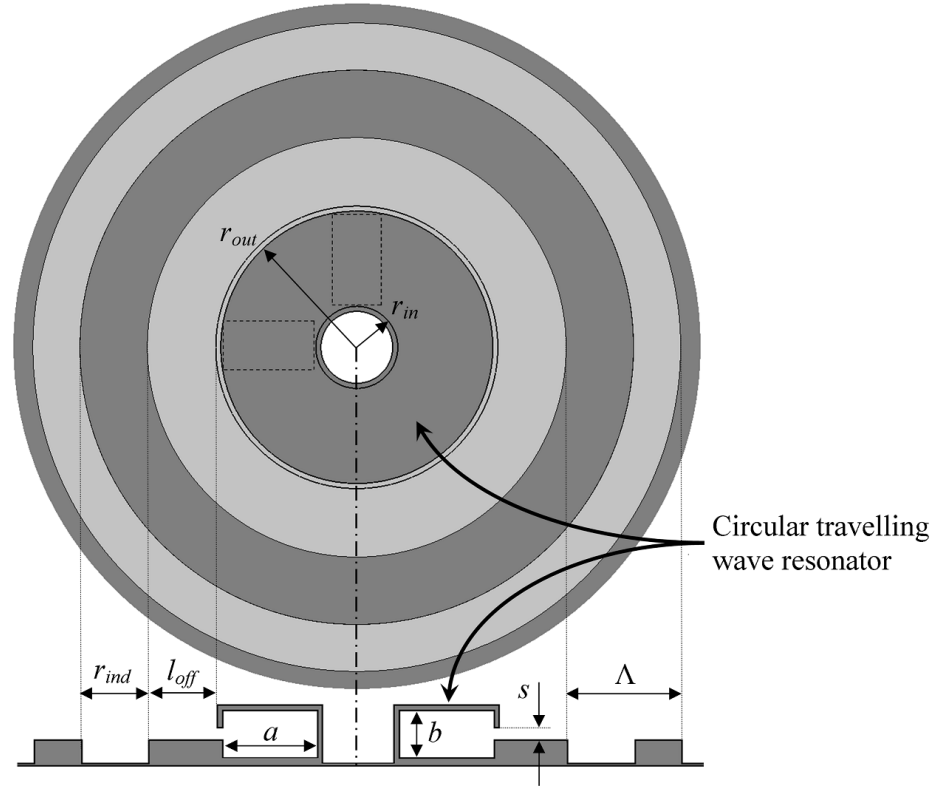


Figure 6.4: Dimensions of the circular travelling wave resonator and surrounding Bull's eye antenna.

and the null width is 52.8° . For five rings, the gain increases to 13.5 dBi and the null width decreases to 22.6° .

Figure 6.6 shows the magnitude of the electric field on a $160 \times 160 \text{ mm}^2$ plane, 50 mm above the surface of the antenna. It shows the characteristic null on boresight, which is expected due to the expression $\left(\frac{r\sqrt{2}}{w(z)}\right)^{|l|}$ in Equation 6.1 for $l \neq 0$. The asymmetry in the electric field intensity is caused by the quadrature position of the waveguide feeds.

The impedance bandwidth is 2.4 GHz, with the S_{11} parameter being lower than -10 dB between 58.9 GHz and 61.3 GHz. The far-field radiation pattern is shown in Figure 6.7, with a perspective view in Figure 6.7(a). The characteristic null is present on boresight, and the peak gain of 13.5 dBi occurs $\pm 11^\circ$ off boresight. Figure 6.7(b) shows an offset of 2.3 dB between the two peaks caused by the choice of cut and the asymmetry in the position of the feeds.

Compared to an eight-element array such as presented by Bai *et al.* [98], the far-field pattern of the proposed structure is smoother as it does not produce char-

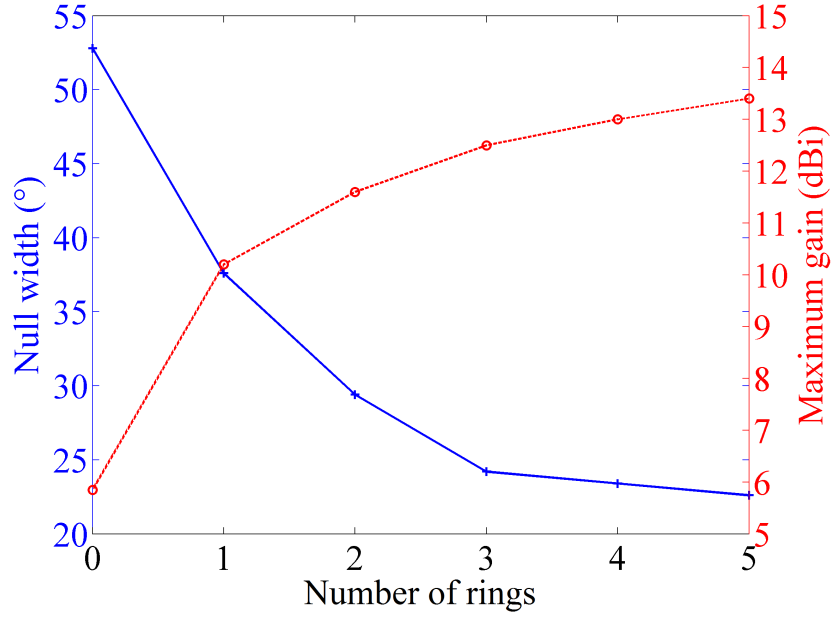


Figure 6.5: Plot of the simulated null width ($^{\circ}$) and maximum gain (dBi) as a function of the number of rings of an OAM Bull's eye antenna for $l = \pm 3$.

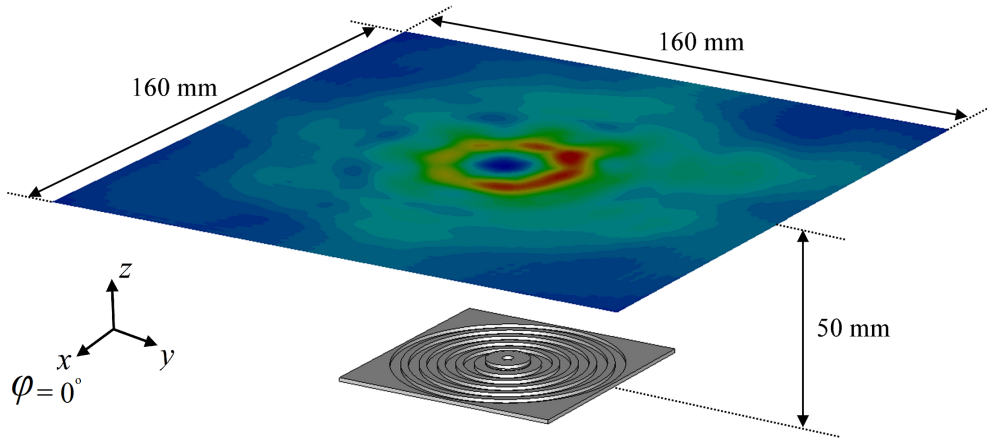


Figure 6.6: Perspective view of radiating top side with projected absolute electric field on a $160 \times 160\text{mm}^2$ plane, 50 mm above the surface the antenna.

acteristic sidelobes. The plot in Figure 6.7(b) compares the far-field pattern for $\varphi = 0^{\circ}$ of the proposed Bull's eye antenna, and the far-field of a simulated eight-element circular array of radius 3λ , and made of open-ended WR-15 waveguides. Plane cuts were taken at $\varphi = 0^{\circ}$ and $\varphi = +22.5^{\circ}$.

A standard, linearly-polarised Bull's eye antenna with a similar diameter reaches a gain of 18 dBi [64] compared to 30 dBi for a parabolic antenna of this diameter [43]. However, the parabolic antenna used for OAM mode generation,

6.2 Bull's eye antenna for OAM generation

as used for example by Hui *et al.* [99], is approximately 50 mm high which gives it an aspect ratio of 100%. The structure proposed here has an aspect ratio of less than 5%.

Figure 6.8 illustrates the phase of the electric field in a plane 50 mm above the antenna, and shows the helical phase pattern that accumulates 6π of phase in each clockwise rotation about boresight, confirming an OAM mode $|l| = 3$. The phase increasing clockwise indicates a positive mode number $l = +3$. For negative mode $l = -3$, the data are identical but the phase accumulates anti-clockwise about boresight. Figure 6.8(a) shows the theoretical phase distribution plotted according to Equation 6.1 and Figure 6.8(b) shows the simulated results obtained with the proposed OAM Bull's eye antenna.

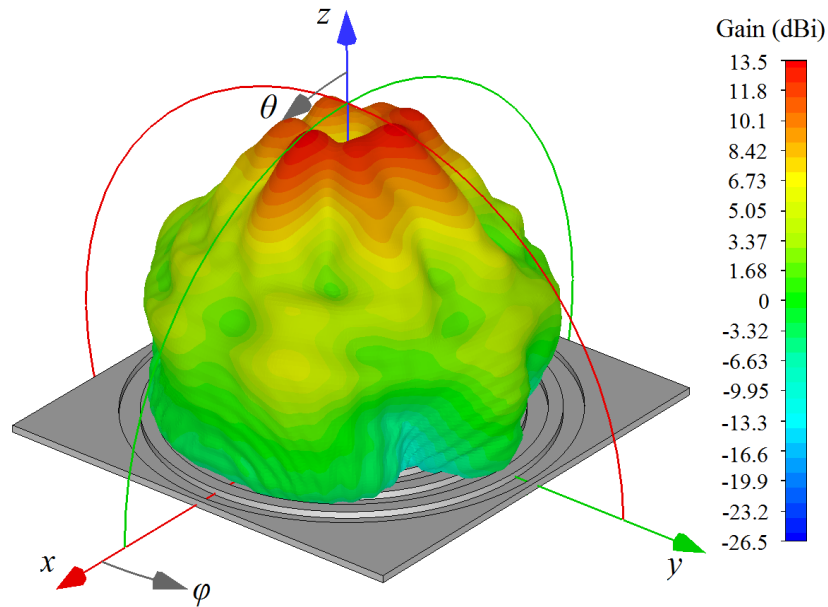
To evaluate the purity of the mode generated by the OAM Bull's eye antenna, an analysis based on a phase gradient method was carried out. It is based on the estimation of the OAM mode from the phase difference between two points along an arc ($\phi_2 - \phi_1$) divided by their angular spacing α as defined in the inset in Figure 6.9. It is expressed as:

$$l = \frac{\phi_2 - \phi_1}{\alpha}. \quad (6.4)$$

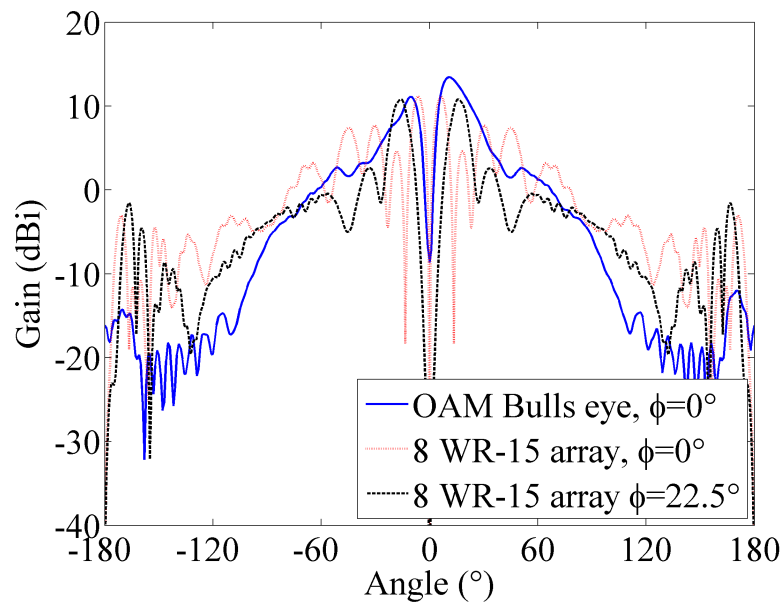
Equation 6.4 was applied as described by Allen *et al.* [100]. The results are shown in Figure 6.9 for three values $\theta = 4^\circ, 11^\circ, 26^\circ$ where θ is the polar angle off boresight. Those angular values θ were chosen because they correspond to peak gain, and -5 dB on each side.

For the three θ values, the error for the estimated OAM mode $l = +3$ is smaller than ± 0.3 when the angular separations between the receive elements are $\alpha > 60^\circ$. It was shown that eight-element arrays generate more accurate modes for small values of α , and so smaller separations between the receive elements can be used [100]. For a fixed size receiving array at $l = \pm 3$, these effects approximately cancel each other, giving the design similar performance but with reduced complexity. For a propagation distance of 10 m, $\alpha = 60^\circ$, and $\theta = 4^\circ$, the receive elements would be separated by 73 cm. For an eight-element array of radius 3λ , a similar gain is reached at $\theta = 10^\circ$, and the receive separation is only $\alpha = 20^\circ$, giving 61 cm separation between the receive elements. However, the proposed OAM Bull's eye antenna can produce simultaneously two modes $l = \pm 3$, has a narrower null, and allows larger receiver element separations if

6.2 Bull's eye antenna for OAM generation

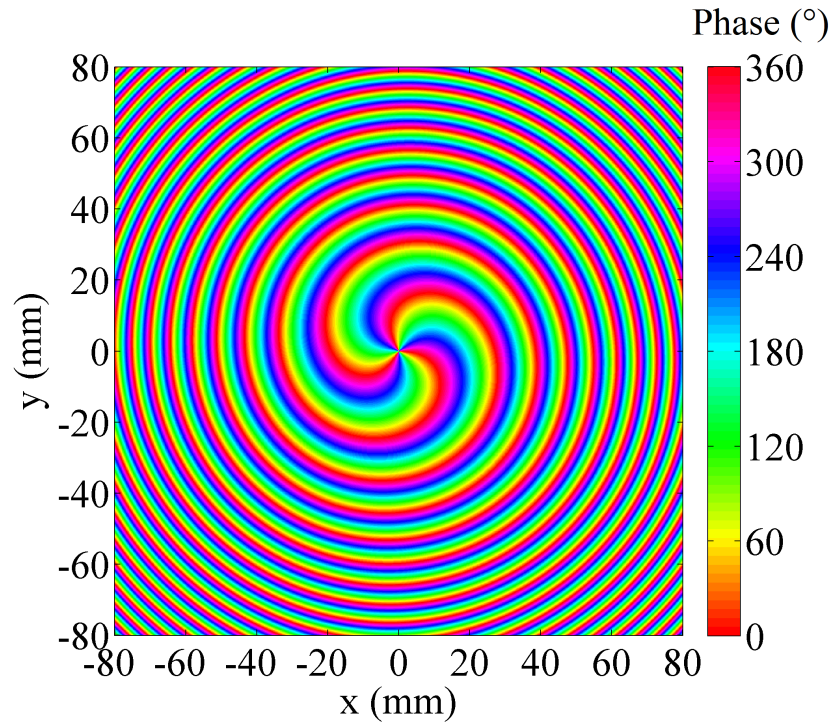


(a) Perspective far-field radiation pattern of the Bull's eye OAM antenna ©2016 The Institution of Engineering and Technology.

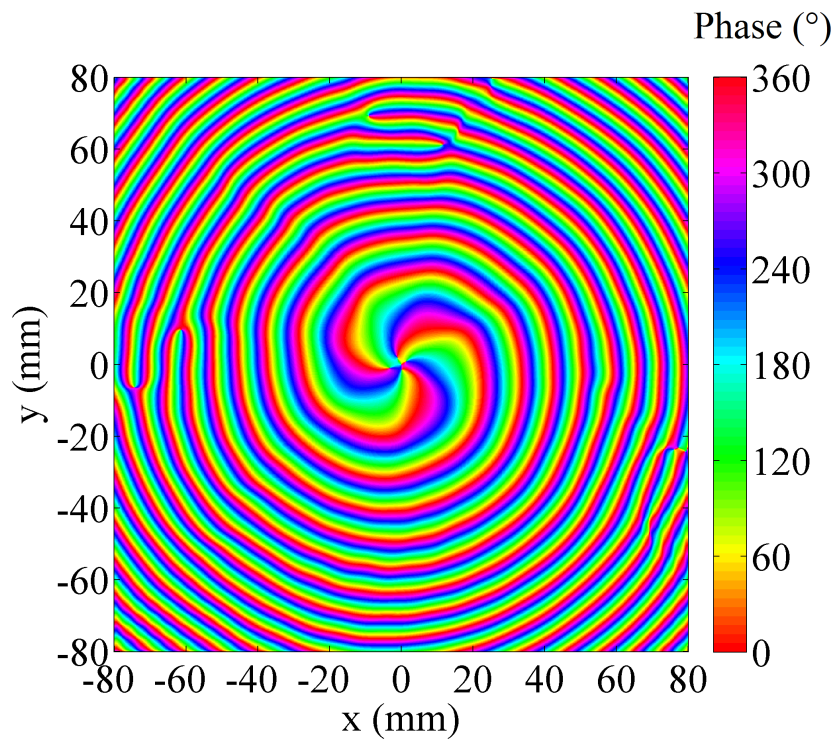


(b) Comparison of far-fields between the five ring OAM Bull's eye antenna for $\phi = 0^\circ$ of five ring OAM Bull's eye antenna, and an eight-element array of diameter $D = 30$ mm made of open-ended WR-15 waveguides for $\phi = 0^\circ$ and for $\phi = 22.5^\circ$.

Figure 6.7: Far-field radiation pattern of the Bull's eye OAM antenna and comparison with an eight-element array of diameter $D = 30$ mm made of open-ended WR-15 waveguides.



(a) Analytical model.



(b) Simulation results.

Figure 6.8: Phase distribution for the E_θ component on a $160 \times 160 \text{ mm}^2$ plane, 50 mm above the antenna.

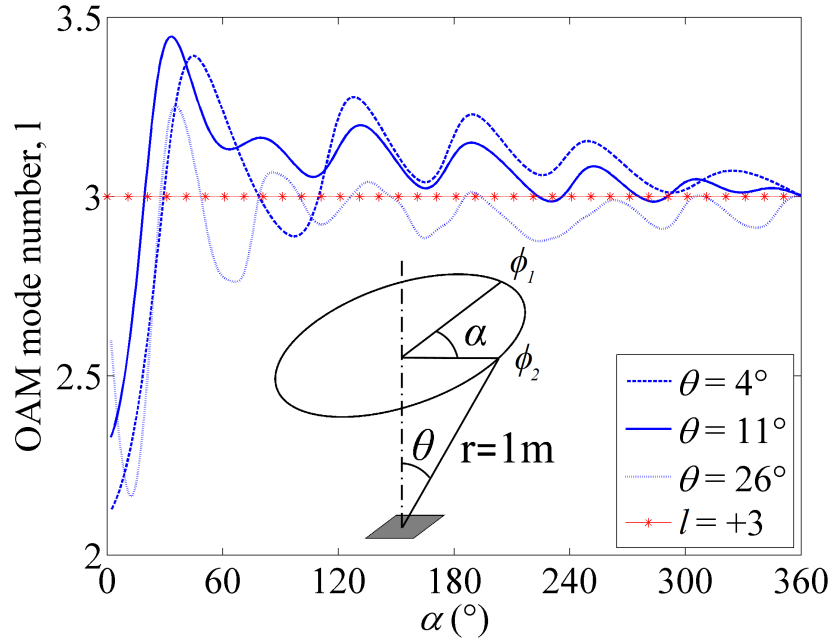


Figure 6.9: Mode purity for three different angles of θ , confirming the mode is $l = +3$. Similar results are obtained for the $l = -3$. The polar angle θ , the angular separation α and the phase difference between two points ($\phi_2 - \phi_1$) are defined in the inset ©2016 The Institution of Engineering and Technology.

required. This larger space parameter can provide an advantage for the design of multi-element receivers [100].

6.2.2 Stacked OAM Bull's eye antenna for multiple modes generation

The generation of multiple, orthogonal, and simultaneous OAM modes is necessary to increase channel capacity when using OAM multiplexing. The idea of stacking multiple OAM Bull's eye antennas can provide a solution to generate multiple orthogonal modes because the generated mode number can be adjusted with the diameter of the circular travelling wave resonator. This concept was implemented to generate two pairs of mutually orthogonal OAM modes. In this configuration, it is possible to find a minimum ring diameter for the higher OAM mode, but large enough to accommodate a smaller OAM Bull's eye antenna on top which produces a smaller OAM mode. The two particular sets of OAM modes $l = (\pm 3, \pm 13)$ were chosen for two reasons:

6.2 Bull's eye antenna for OAM generation

1. the OAM modes $l = (\pm 3, \pm 13)$ are fully orthogonal to each other;
2. the circular travelling wave resonator generating OAM mode $l = \pm 13$ is large enough to accommodate an OAM Bull's eye antenna on top to produce OAM mode $l = \pm 3$.

The proposed design is illustrated in Figure 6.10, showing the two stacked OAM Bull's eye antenna structures. Each antenna is fed independently, with two orthogonal WR-15 waveguide ports with 90° phase shift. The top OAM Bull's eye antenna is designed to produce OAM modes $l = \pm 3$ and is similar to the one presented in Section 6.2.1. It has two indented rings and a total outside radius of 16.4 mm. The bottom OAM Bull's eye antenna is design to produce OAM mode $l = \pm 13$. It has four indented rings and a circular travelling-wave resonator of outside radius of 16.2 mm. The full structure has an overall size of $73 \times 73 \times 5 \text{ mm}^3$.

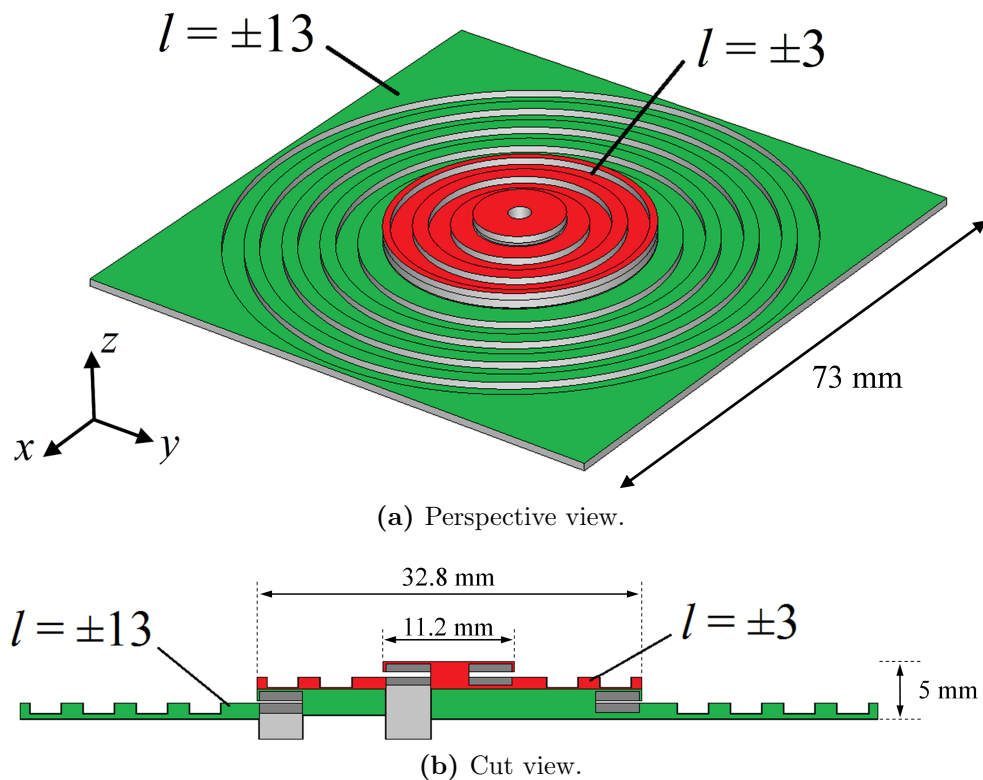


Figure 6.10: Stacked OAM Bull's eye antenna for $l = \pm 3$ and ± 13 , with red for the $l = \pm 3$ structure and green for the $l = \pm 13$ structure ©2016 The Institution of Engineering and Technology.

6.3 Receiving scheme for multi OAM modes

Figure 6.11 shows the projected magnitude and phase distribution of the electric field when two OAM modes, $l = +3$ and $+13$ are generated simultaneously. The plane of projection is $173 \times 173 \text{ mm}^2$ and is 50 mm (10λ) above the OAM stacked Bull's eye antenna. Figure 6.11(a) illustrates the two separate concentric LG distributions for $l = +3$ (inner) and $l = +13$ (outer) and Figure 6.11(b) shows the phase singularity on boresight for $x = y = 0 \text{ mm}$.

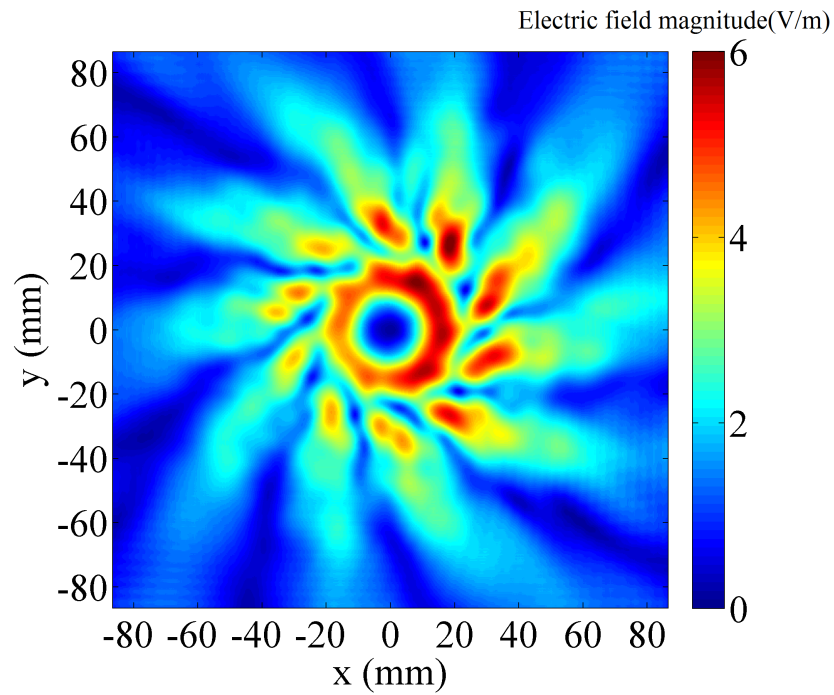
Figure 6.12 shows the results of the mode purity analysis for the OAM mode $l = +3$ and $l = +13$ at $\theta = 15, 30$ and 45° . Those particular values were chosen to illustrate the quality of the two OAM modes $l = +3$ and $l = +13$, and correspondent to the maximum intensity for each of the modes, 13.1 dBi at $\theta = 15^\circ$ for $l = +3$ and 8.1 dBi at $\theta = 45^\circ$ for $l = +13$. In particular, the impedance bandwidth is 2.4 GHz for OAM mode $l = \pm 3$, and 0.6 GHz for OAM mode $l = \pm 13$, which is consistent with the increase of the ring resonator quality factor with mode number [101].

Despite the different peak gain positions for the two mode numbers, there is enough overlap in the two modes to allow both to be detected over an angular range in excess of 30° ($15^\circ < \theta < 45^\circ$). However, a two-element receive array implementing the phase gradient method is unable to be used in this case, because it cannot discriminate between modes of different numbers when both are present, except at the extreme edges of the angular range where one mode is substantially stronger than the other. A multi-mode receiver is preferred, so that it can be placed at a position where the power of both modes is high, and hence maximise the link distance.

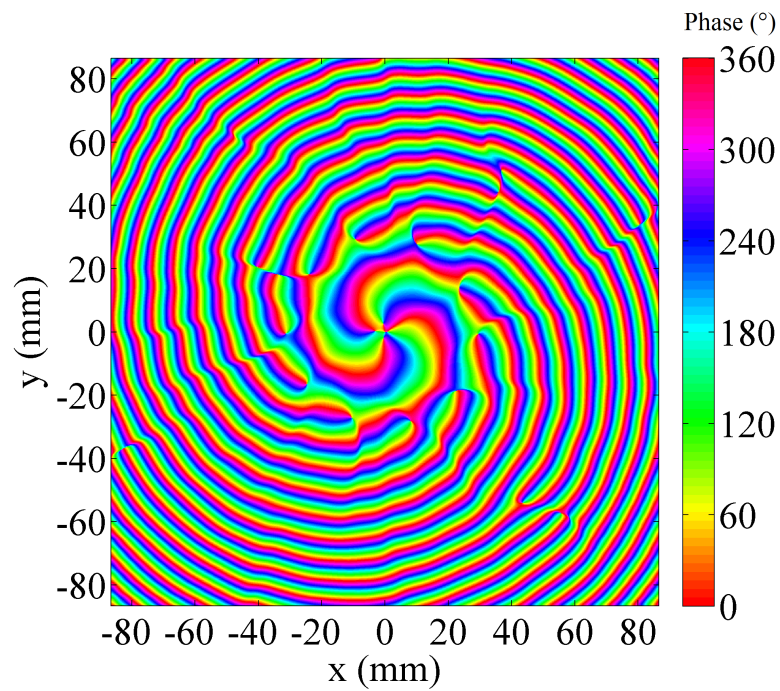
6.3 Receiving scheme for multi OAM modes

The generation of multiple and different simultaneous OAM modes with a stacked Bull's eye antenna design was proposed in the previous Section. In this Section, the study of a receiving scheme for multi OAM mode enabling multiplexing is presented. In particular, the concept of discretely sampled partial aperture receiver, or DSPAR, is investigated, based on a limited number of discrete receivers and providing a good orthogonality between multiple OAM modes. Subsequently, an installation concept is proposed for short-distance applications' implementation.

6.3 Receiving scheme for multi OAM modes

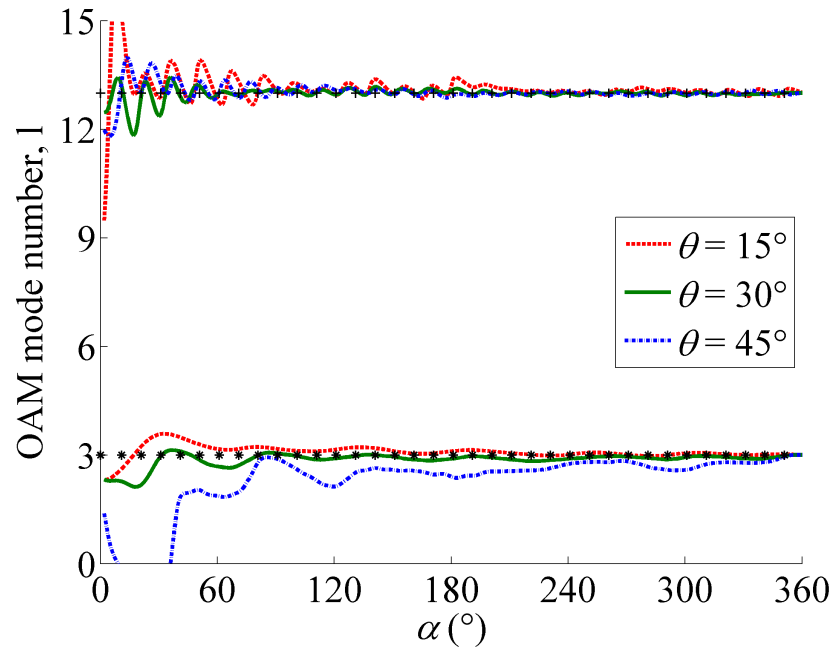


(a) Absolute value of the electric field distribution.

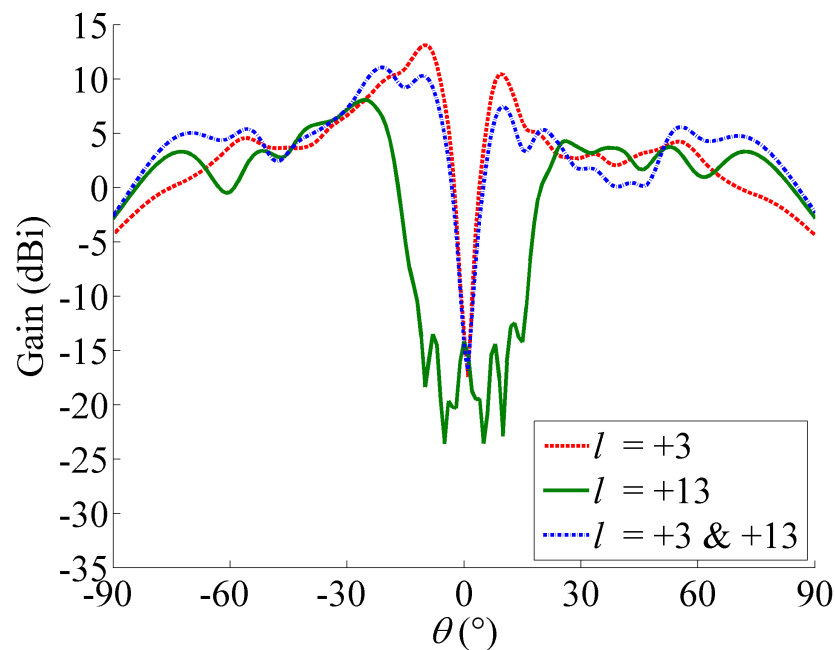


(b) Phase distribution.

Figure 6.11: Magnitude and phase of the electric field distribution on a $173 \times 173 \text{ mm}^2$ plane, 50 mm (10λ) above the OAM stacked Bull's eye antenna.



(a) Mode purity analysis for modes +3, and mode +13, conducted separately but plotted on same graph.



(b) xy -plane far-field cut for OAM stacked Bull's eye $l = (+3, +13)$ and $(+3, +13)$.

Figure 6.12: Simulations of the double ring resonator antenna for modes $l = (+3, +13)$ (results for $l = (-3, -13)$ are similar) ©2016 The Institution of Engineering and Technology.

6.3.1 Partial aperture receivers for multiplexed OAM modes

The relatively limited spread of the OAM mode in optical fibre-based transmission schemes drove the recent work on OAM multiplexing in the optical regime. For example, a multiplexing scheme with two OAM modes $l = \pm 1$ and two linear polarisations was used in conjunction with 4×4 MIMO-DSP processing to recover the data from the four channels after transmission over 5 km of fibre [102]. In this configuration, all OAM modes retain their mutual orthogonality because the whole spatial extent of the mode is used in the de-multiplexing process [103, 104, 105]. Similarly, the concept has been implemented at millimetre-wave frequencies using four spiral phase plates with modes $l = (\pm 1, \pm 3)$ over a 2.5 m distance, and providing cross talk ranging from -12 to -14 dB [91].

However, a whole-aperture receiver is impractical for longer distance links, because the size of the receiving aperture increases with the link distance. A partial aperture receiver is possible and it has been studied in the optical [106] and in the infra-red regime [107]. However it can induce cross talk between modes [108], but a subset of the modes can retain ideal orthogonality [107]. For an angular aperture of $2\pi/n$, the degree of orthogonality $U(l_a, l_b)$ between mode l_a and l_b can be expressed as:

$$U(l_a, l_b) = \frac{n}{2\pi} \int_0^{2\pi/n} e^{j(l_a - l_b)\phi} d\phi = \begin{cases} 1, & \text{if } l_a = l_b \\ 0, & \text{if } l_a - l_b = mn \\ > 0, & \text{otherwise} \end{cases} \quad (6.5)$$

where n and m are integers.

Table 6.2 lists the pairs of mode numbers for $n \in \{2, \dots, 6\}$ and $m \in \{1, \dots, 5\}$ that achieve perfect orthogonality with $U(l_a, l_b) = 0$ such as $l_a - l_b = mn$. The number of supported orthogonal modes is indicated by the location of the ‘ \pm ’ symbol. For example, for $n = 5$ and $m = 1$, the table cell $\pm(3, 8)$ indicates that modes $l_a = 3$ and $l_b = 8$ are orthogonal to each other, and so are $l_a = -3$ and $l_b = -8$. However, $l_a = 3$ and $l_b = -8$ are not orthogonal to each other, nor $l_a = -3$ and $l_b = 8$. This case is referred to as a two-way orthogonality. On the other hand, the notation $(\pm 3, \pm 9)$ means that four-way orthogonality exists. For example, $l_a = \pm 3$ and $l_b = \pm 9$ are mutually orthogonal for $n = 6$ and $m = 1$.

From Table 6.2, at $n = 6$, four-way orthogonality is only possible if the first mode is $l_a = 3$, but not if it is $l_a = 1$. For $n = 2$, four-way orthogonality is

6.3 Receiving scheme for multi OAM modes

Table 6.2: Orthogonal mode pairs for partial apertures of $2\pi/n$, for a selection of starting mode numbers. The number of supported orthogonal modes is indicated by the location of the ‘ \pm ’ symbol. ©2016 The Institution of Engineering and Technology.

n \ m	1	2	3	4	5
6	$\pm(1,7)$ $(\pm 3, \pm 9)$	$\pm(1,13)$ $(\pm 3, \pm 15)$	$\pm(1,19)$ $(\pm 3, \pm 21)$	$\pm(1,25)$ $(\pm 3, \pm 27)$	$\pm(1,31)$ $(\pm 3, \pm 33)$
5	$\pm(3,8)$	$\pm(3,13)$	$\pm(3,18)$	$\pm(3,23)$	$\pm(3,28)$
4	$\pm(3,7)$	$\pm(3,11)$	$\pm(3,15)$	$\pm(3,19)$	$\pm(3,23)$
3	$(\pm 3, \pm 6)$	$(\pm 3, \pm 9)$	$(\pm 3, \pm 12)$	$(\pm 3, \pm 15)$	$(\pm 3, \pm 18)$
2	$(\pm 3, \pm 5)$	$(\pm 3, \pm 7)$	$(\pm 3, \pm 9)$	$(\pm 3, \pm 11)$	$(\pm 3, \pm 13)$

achievable for the five values of m . The Bull’s eye antenna achieves mode purity for $\alpha > 60^\circ$ so these modes combination provides flexibility for the design of the circular travelling wave resonator. As a result, if the first mode pair is $l_a = \pm 3$, the OAM Bull’s eye antenna can achieve four-way orthogonality if the second mode pair is $l_b \in \{\pm 5, \pm 6, \pm 7, \pm 9, \pm 11, \pm 12, \pm 13, \pm 15, \pm 18\}$ when $n = 2, 3$ in Table 6.2. As described in the previous Section, the pair chosen for the stacked OAM Bull’s eye antenna was $l = (\pm 3, \pm 13)$ so as to agree with the physical limitations of the circular travelling wave resonators.

6.3.2 Discrete multi-mode receiver

In the previous Section, it has been shown that ideal orthogonality between different OAM modes can be achieved with partial, continuous-receiving apertures. This Section aims to establish whether multi-mode receivers that consist of multiple discrete receiving elements, called discretely sampled partial aperture receivers, or DSPAR, have the same constraints on orthogonality of modes as continuous partial aperture receivers. Previous work already investigated the bit error rate of 2-OAM and 4-OAM systems using multiple-antenna receivers [106]. However the connection between choice of the mode number and the achievable performance of the system was not established. Subsequently, the benefit of the non-uniform spacing of the receive elements concept is discussed by comparing performance to uniformly sampled partial aperture receivers, or USPAR. The discrete form of Equation 6.5, for a DSPAR or a USPAR with N elements, can be established

6.3 Receiving scheme for multi OAM modes

using a point summation:

$$\begin{aligned}
 U(l_a, l_b) &= \frac{1}{\phi_N - \phi_1} \int_{\phi_1}^{\phi_N} e^{j(l_a - l_b)\phi} d\phi \\
 &\approx \frac{1}{N} \sum_{k=1}^N e^{j(l_a - l_b)\phi_k},
 \end{aligned} \tag{6.6}$$

where ϕ_N is the absolute angular position of the N^{th} receiver, l_a and l_b are two OAM modes with $a, b \in \{1, 2, 3, 4\}$. A number of four receiver ($N = 4$) was chosen because DSPAR with $N < 4$ elements cannot provide a four-way orthogonality, while DSPAR with $N > 4$ requires an additional receiving element but does not significantly outperform. The element positions $[\phi_1, \phi_2, \phi_3, \phi_4]$ of USPAR or DSPAR are disposed along a sub-portion of a circular arc as illustrated in Figure 6.13.

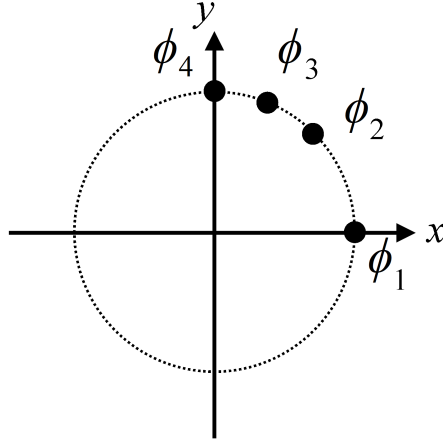


Figure 6.13: Schematic of the element positions $[\phi_1, \phi_2, \phi_3, \phi_4]$ on the receiving plane for DSPAR or USPAR with $N = 4$ elements.

For each UPSAR and DSPAR design, the value of $U(l_a, l_b)$ was calculated using Equation 6.6 for each of the 16 combinations of the four transmitted mode numbers, with the condition that $l_1 = -l_2$ and $l_3 = -l_4$. The result is referred to as the side mode rejection ratio (SMRR) for the 12 combinations that measure unwanted leakage between modes. For an ideal noise-free, fading-free channel,

6.3 Receiving scheme for multi OAM modes

the SMRR between the two modes l_a and l_b is

$$\text{SMRR}(l_a, l_b) = 20 \log_{10} \left(\left| \frac{U(l_a, l_b)}{U(l_a, l_a)} \right| \right), \quad (6.7)$$

where $a, b \in \{1, 2, 3, 4\}$ and $a \neq b$. It is typically admitted that orthogonality is achieved for $\text{SMRR} < -12$ dB [91]. Table 6.3 lists the results for a subset of mode combinations given in Table 6.2. Additionally, the results for USPARs are listed. The angular positions of the DSPAR elements were calculated using a Monte Carlo simulation method with ensemble size of 100,000 for each mode pair. The smallest DSPARs that performed well were chosen and the positions were normalised with respect to the position of the first element ϕ_1 .

Table 6.3: Side mode rejection ratio (SMRR, dB) for a DSPAR (non-uniform spacing) and USPAR (uniform spacing) with $N = 4$ receivers for selected mode pairs from Table 6.2 ©2016 The Institution of Engineering and Technology.

Mode pair ($\pm l_a, \pm l_b$)	n	DSPAR† Position (°)	SMRR (dB): DSPAR/USPAR			
			($-l_a, +l_a$) ($+l_a, -l_a$)	($-l_a, -l_b$) ($+l_a, +l_b$) ($-l_b, -l_a$) ($+l_b, +l_a$)	($-l_a, +l_b$) ($+l_a, -l_b$) ($-l_b, +l_a$) ($+l_b, -l_a$)	($-l_b, +l_b$) ($+l_b, -l_b$)
(3,5)	2	[0,62,80,158]	-13.2/0.0	-17.6/-12.0	-15.8/-12.0	-15.3/-12.0
(3,9)	6	[0,18,31,45]	-21.4/-12.0	-21.4/-12.0	-19.7/-12.0	-13.3/0.0
(3,11)	4	[0,24,37,62]	-19.1/-324	-18.3/-12.0	-17.8/-7.27	-22.4/-7.27
(3,12)	3	[0,22,34,56]	-21.5/-12.0	-17.1/0.0	-12.1/-12.0	-23.1/-12.0
(3,15)	6	[0,17,31,47]	-31.6/-12.0	-16.1/-12.0	-22.1/0.0	-17.8/-12.0
(3,18)	5	[0,27,35,62]	-27.9/-12.0	-18.4/0.0	-12.7/-12.0	-312/-12.0
(3,19)	4	[0,32,40,73]	-22.9/-324	-16.7/-12.0	-22.1/-7.27	-14.7/-7.27
(3,21)	6	[0,21,29,51]	-31.6/-12.0	-22.1/0.0	-13.7/-12.0	-14.9/-12.0
(3,23)*	5	[0,20,27,46]	-20.2/-12.0	-21.2/-12.0	-11.3/-23.1	-14.6/-0.98
(3,27)	6	[0,23,30,53]	-317/-12.0	-19.6/-12.0	-309/-12.0	-301/0.0
(3,28)	5	[0,22,30,51]	-31.6/-12.0	-31.4/-12.0	-17.9/-0.98	-12.4/-23.1
(3,33)	6	[0,15,30,45]	-323/-12.0	-303/-12.0	-315/0.0	-298/-12.0

† The positions of the receivers for USPAR are: [0,60,120,180] for $n = 2$, [0,40,80,120] for $n = 3$, [0,30,60,90] for $n = 4$, [0,24,48,72] for $n = 5$, and [0,20,40,60] for $n = 6$.

* The SMRR of DSPAR is slightly larger than -12 dB for four combinations but remain better than USPAR.

The results show that DPSAR achieves four-way orthogonality for all the mode pair except (3,23) for which SMRR is slightly larger than -12 dB with (-3,-23), (+3,+23), (-23,-3) and (+23,+3). However, USPAR is not capable of achieving orthogonality for any of the mode pairs, which illustrates the benefit of

non-uniformly distributed receivers.

6.3.3 Four element receiver for stacked OAM antenna

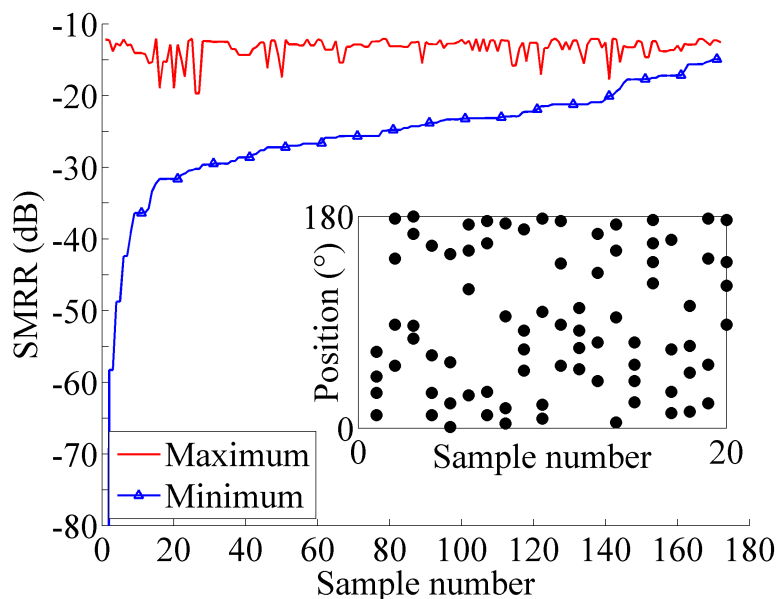
A DSPAR made of $N = 4$ elements with four-way orthogonality was designed for the stacked OAM Bull’s eye antenna with modes $l_{a,b} = (\pm 3, \pm 13)$ presented in Section 6.2.2. It was designed using a similar Monte Carlo approach with ensemble size of 100,000. The partial aperture was set at $n = 2$ (180°) as the upper bound for the search space. A set of 172 candidates with SMRR < -12 dB were found, and were organised and listed as shown in Figure 6.14(a). A design with receivers at positions of $\phi = 10, 43, 61,$ and 94° was chosen, giving us an angular dimension of 84° for the full array. Note that this design is different to the ‘two-pairs’ scheme proposed in [109].

The theoretical SMRR was calculated for OAM modes $(\pm 3, \pm 13)$ with Equation 6.6. Figure 6.14(b) shows the result and illustrates the four-way orthogonality with SMRR < -12 dB for all the mode combinations, but not for USPAR with $n = 2$ and $n = 4$.

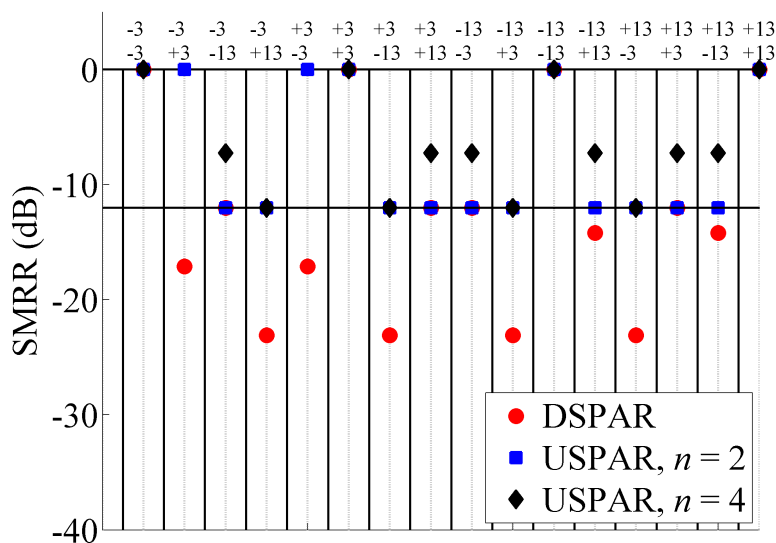
The SMRR was then analysed using simulated far-field data for mode 3 and mode 13 from the stacked OAM Bull’s eye antenna at $\theta = 30^\circ$. In order to test the sensitivity to rotational fading, the receiving elements were progressively offset by 1° rotational increments. The results are plotted in Figure 6.15(a) and show that the SMRR remains better than -8 dB for all positions, with -15 dB on average for orthogonal mode 3 and mode 13. The results are only shown for OAM modes $l = +3$ and $l = +13$ for clarity, because the opposite OAM modes were similar. These results confirm that no particular angular alignment between the mode and the receiver is needed.

An installation concept was then proposed to illustrate the implementation of an OAM link between the stacked OAM Bull’s eye transmitter presented in Section 6.2.2 (Tx), and a DSPAR, with receivers denoted Rx1 to Rx4. Figure 6.15(b) shows that the concept simplifies OAM links over longer distances than implementations using spiral phase plates. The four receivers can be mounted on the face of an opposite building or other infrastructure. Masts can also be considered as a free standing structure if necessary. The size of the antennas are exaggerated for clarity, but the angular positioning of the receivers is to scale.

6.3 Receiving scheme for multi OAM modes



(a) Top 172 results from Monte Carlo simulation with ensemble size 100,000, graded according to best case side mode rejection ratio (SMRR), and inset, the angular position in degrees for the first twenty antennas.



(b) SMRR calculation illustrating the four way orthogonality for modes $l = (\pm 3, \pm 13)$ calculated with point summation (Equation 6.6) for one of the optimised DSPAR. For comparison the results for USPAR with an equivalent partial aperture of $n = 4$, and one with $n = 2$, are shown, neither of which achieves orthogonality.

Figure 6.14: Results of Monte Carlo simulation and illustration of four-way orthogonality for receivers at position $\phi = 10, 43, 61, \text{ and } 94^\circ$ ©2016 The Institution of Engineering and Technology.

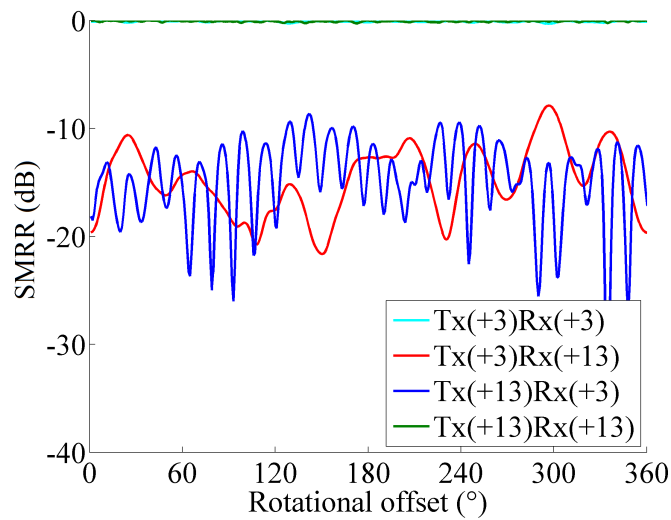
This receive scheme provides advantages over conventional large aperture antennas because it is sparsely populated and hence requires no interstitial structures. This, overall, requires less weight, gives lower windage and costs less to install. The sensitivity to the masts moving was analysed, showing that up to 1° of angular lateral movement provides acceptable performance. This is equivalent to 3 cm over 3 m link distance, and the sensitivity to absolute movement is reduced with increasing link distances.

6.4 Chapter summary

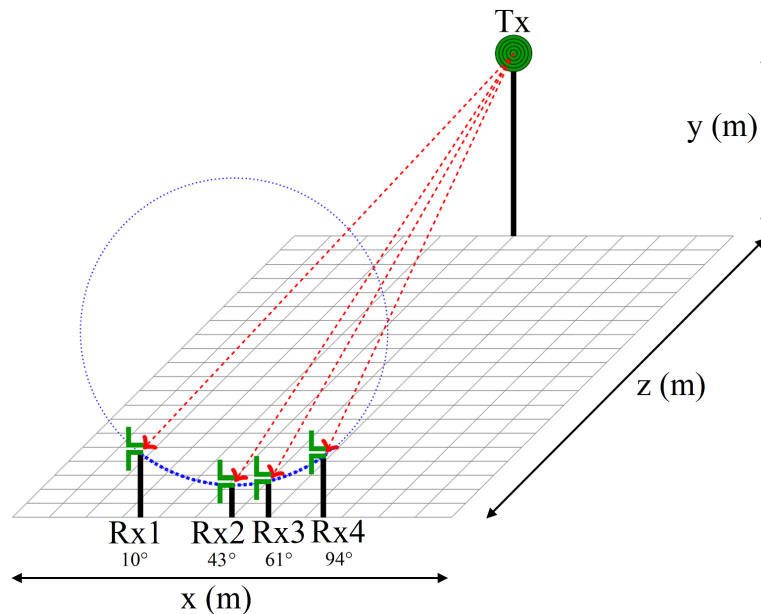
In this Chapter, the design and simulation of two planar millimetre-wave antennas based on a circular travelling-wave resonator, surrounded by a Bull's eye structure were presented. The first design can produce two simultaneous and orthogonal OAM modes $l = \pm 3$, enabling OAM multiplexing. In particular, the proposed OAM Bull's eye antenna operates at 60 GHz and provides a maximum gain of 13.5 dBi at $\theta = \pm 11^\circ$ with five rings.

To take further advantage of OAM multiplexing, an improved structure was then designed and studied. This antenna is based on two stacked OAM Bull's eye structures producing, simultaneously, four OAM modes $l = (\pm 3, \pm 13)$. These particular mode were chosen because full orthogonality can be achieved between all the mode combinations for continuous receivers larger than $\alpha = 180^\circ$.

Moreover, a novel multi-element receiver arrays concept, called discretely sampled partial aperture receivers, or DSPAR, was introduced. It was first demonstrated that partial, discretely set apertures, are capable of achieving perfect orthogonality between pairs of OAM modes. In addition to freedom of mode choice, the main practical benefit of using DSPAR is that it does not require a large solid antenna structure, but instead, only a small number of inexpensive single-element antennas is necessary. Hence, receiving transmissions from the OAM Bull's eye antenna at much larger distances is possible by scaling DSPAR. OAM multiplexing may appear less suitable than other multiplexing methods because OAM beams inevitably diverges over large distances. However it was shown in this Chapter that several key improvements can enable practical implementation of OAM multiplexing for millimetre-wave applications.



(a) SMRR calculation for modes +3 and +13 when all four modes ± 3 , ± 13 are transmitted from the Bull's eye antenna, for the optimal antenna array at each possible ϕ position around the mode.



(b) Perspective view of the installation concept for $l = (\pm 3, \pm 13)$ OAM with four receivers at $\phi = 10, 43, 61,$ and 94° with $\theta = 30^\circ$, showing an architecture over a longer link distance with a transmitting (Tx) OAM antenna and 4 receivers (Rx1, Rx2, Rx3 and Rx4) mounted on masts.

Figure 6.15: Four element receiver array design optimised to suit transmissions from dual stacked OAM Bull's eye antenna ©2016 The Institution of Engineering and Technology.

Chapter 7

Conclusions and future work

This Thesis presented investigations of Bull's eye antenna designs for terrestrial and space applications in the 60 GHz band. The work was constructed around three main parts. First, a Bull's eye antenna was designed and experimentally demonstrated at 60 GHz. A planar feeding technique was then proposed for a cheaper and more straightforward integration onto circuit boards. Second, improved Bull's eye antenna designs were simulated or experimentally demonstrated in order to offer greater flexibility in terms of beam deflection, beam steering and integration onto non-planar surfaces. Third, an existing feeding technique was implemented onto a Bull's eye antenna so as to generate orthogonal orbital angular momentum (OAM) modes. A new receiving scheme enabling easier implementation of OAM multiplexing was then investigated.

The main achievements of this study are as follows:

- The prototype of a Bull's eye antenna operating around 60 GHz was first simulated, fabricated and measured, providing satisfying performance and bringing confidence in the robustness of the concept. The manufactured prototype, adapted for integration onto a face of a CubeSat, had seven indented rings, an impedance bandwidth at -10 dB of 5 GHz and a maximum gain of 19.1 dBi;
- A microstrip-based feeding structure was identified and designed as an alternative to the bulky and expensive coaxial to waveguide adapters. A Bull's eye antenna with two indented ring was manufactured to demonstrate this new type of feed, enabling a directional and efficient Bull's eye antenna

to be used in monolithic microwave integrated circuits (MMICs) or other types of planar board technologies;

- The study of deflecting the radiation beam of a Bull's eye antenna by shifting the rings of the corrugated surface was carried out. A specific shifting scheme was identified, and the possibility of shifting a single beam, or creating multiple beam by exploiting the localised effect of the surface waves was studied. Subsequently, the prototype of a Bull's eye antenna with two separate and symmetrical shifted ring patterns was design and fabricated, resulting in the creation of two deflected beams at $\pm 16.1^\circ$ off boresight;
- The design of a discretely steerable Bull's eye antenna based on the division of the active surface in several paired sectors was presented. Different ring patterns can be allocated to each paired sector, resulting in a discrete mechanically steerable Bull's eye antenna. A prototype based on three paired sectors was designed and fabricated, providing three different symmetrical radiation patterns: a single beam on boresight (0°), two beams at $\pm 8^\circ$ and two beams at $\pm 15^\circ$ off boresight;
- A conformal Bull's eye antenna was presented, showing that the ring patterns can be adjusted to preserve a high directivity while allowing the Bull's eye antenna to be integrated onto a convex surface. A convex conformal Bull's eye antenna with radius of curvature of $R = 75$ mm, with an adjusted ring pattern was simulated following earlier design rules. The results showed that the performance of the proposed antenna are similar to those of the corresponding planar Bull's eye antenna;
- The design of a Bull's eye antenna using a modified feed was proposed to generate non-zero orbital angular momentum (OAM) modes. Based on a circular, travelling-wave ring resonator, an OAM Bull's eye antenna generating two simultaneous OAM mode $l = \pm 3$ was investigated;
- An improvement of the OAM Bull's eye antenna was proposed in order to generate more simultaneous and orthogonal OAM modes. The design was based on two OAM Bull's eye structures stacked on top of each other. This structure was simulated and could generate four simultaneous OAM modes $l = (\pm 3, \pm 13)$;

- A discretely sampled partial aperture receiver, called DSPAR, was proposed to enable OAM demultiplexing with a limited number of sparsely distributed receivers. A Monte Carlo simulation method was used to identify sets of four non-uniformly distributed receivers so as to provide good orthogonality between all OAM mode combinations for $l = (\pm 3, \pm 13)$.

The next Sections summarise the main results and limitations of the work presented through this Thesis, and further investigations are suggested. The CalSat project is then briefly presented and can take advantage of Bull's eye antenna features operating in other frequency bands.

7.1 Bull's eye antenna design and planar feeding technique

The Bull's eye antenna design was proposed by Beruete *et al.* [52] and was the first Bull's eye structure operating at microwave frequencies. The 60 GHz Bull's eye antenna presented in Chapter 4 was a scaled version of the original design, with optimised dimensions to improve the gain and the impedance bandwidth. The prototype was readily manufactured using existing milling techniques with a particular corner-chamfered subwavelength aperture. The effect of adding additional rings to a subwavelength aperture structure was studied and an asymptomatic increase of the peak gain was found. The peak gain was better than 16.7 dBi over the 5.06 GHz of impedance bandwidth (-10 dB). The simulation results were in close agreement with the radiation pattern measurements which were obtained with a fabricated test bench.

In addition, a microstrip-to-waveguide transition based feed for a Bull's eye antenna was designed, simulated and experimentally demonstrated at 60 GHz. This planar feed solution eliminates the need for an expensive and bulky WR-15 waveguide adapter. The microstrip was fabricated using a PCB process, while the hollow waveguide section and the corrugated rings were manufactured with a CNC milling machine. For better accuracy in the fabrication of the subwavelength aperture, an electrical discharge machining (EDM) technique was used to overcome the difficulties faced by a standard milling machine process for high profile ratio drilling. The Bull's eye antenna had two indented rings and covered

a $25 \times 25 \text{ mm}^2$ area, offering a peak gain of 11.8 dBi. The corrugated surface can be expanded to include more indented rings which can readily provide higher gain without altering the feed.

7.1.1 Future work

The choice of a microstrip-based transition was largely supported by the low price and the fabrication facility for prototyping, but advancing to substrate-integrated waveguide (SIW) technology is suggested. SIW is often more efficient and more suited to millimetre-wave applications because it benefits from the advantages of rectangular waveguides (e.g. lower crosstalk) and substrate-based transmission lines (e.g. smaller dimensions). In addition to better mechanical integration of the Bull's eye antenna onto planar structures, this is expected to provide improved flexibility in the implementation of a wireless solution at 60 GHz requiring a directive antenna package.

Antenna packages for CubeSat applications, such as the proof-of-concept reported in Appendix C, could also benefit from this low profile feeding technique. The design is based on a 0.5U structure, and includes a 2.4 GHz planar inverted F antenna (PIFA) for long range, low data rate communications. Additionally, two Bull's eye antennas with orthogonal polarisation-based channels would provide a high data rate, full duplex link. In a mission requiring a constellation of CubeSats, the members would be capable of achieving data rates of 500 Mbps over a distance of 300 m, while relying on a low data rate link in case of a severe misalignment during a major manoeuvre phase. Further investigation is suggested to refine the design in order to provide a more suitable package to suit the CubeSat industry standards.

7.2 Beam deflection and beam steering

A mechanically-steerable Bull's eye antenna based on a rotating corrugated plate with three pairs of opposing sectors was presented and experimentally demonstrated. Each paired sector had a different corrugated pattern which allowed for three different beam patterns in total. The beam steering directions could be selected amongst the three possibilities during operation. The ring patterns

7.3 Orbital angular momentum multiplexing

were chosen so as to give a single beam on boresight (0°), dual beams at $\pm 8^\circ$, and dual beams at $\pm 15^\circ$, with all beams achieving a gain of at least 15 dBi. A close agreement was achieved between measurement and simulation results with minimal discrepancies in the shape of radiation patterns. The main advantage of this approach is that each pair of sectors can be designed independently from the other two. This is achieved by including a mask on the top layer to prevent any stray surface currents from reaching the two pairs of sectors that are not in use (since it would create unwanted contribution to the radiation pattern and decrease the directivity in most cases). As a result, the design of the corrugated plate is not limited to the example presented in this study, and other possibilities can be envisaged. In particular, if three symmetrical ring patterns were chosen in this study, a design with three asymmetric ring patterns can provide six different beam possibilities, including the symmetric-paired pattern where the rotating plate is in a 180° complementary position.

7.2.1 Future work

Mechanically-steered millimetre-wave antennas are important for achieving maximum range in point-to-point communications in slowly-varying environments. In this scenario, the link budget is too tight to absorb the full extent of the insertion loss associated with power dividers, dielectric losses in the feed network, and electronic phase-shifters in phased arrays. Applications such as terrestrial back-haul links and communication within a constellation of CubeSats are envisaged. Future work about the implementation of the full mechanical solution is suggested. For example, it would be possible to use a motorised rotation, with patterning of the edge of the rotating plate with a gear pattern and match it to a motor-driver cog located to one side. This straightforward solution is readily feasible because rotation is required around only one axis.

7.3 Orbital angular momentum multiplexing

The design and simulation of a Bull's eye antenna for simultaneously producing four orbital angular momentum modes $l = (\pm 3, \pm 13)$ was centred about 60 GHz, together with a sparse, partial-aperture receiving scheme. The planar OAM Bull's

7.3 Orbital angular momentum multiplexing

eye antenna is made of two stacked travelling-wave, ring resonators, each producing two modes, for four modes in total. These particular modes $l = (\pm 3, \pm 13)$ were chosen because they achieve four way orthogonality, even for receivers with particular partial apertures. The OAM Bull's eye antenna is straightforward to fabricate in aluminium using conventional computer numerical controlled machines, or three dimensional printers.

A sparsely distributed receiver, called a 'discretely sampled partial aperture receiver', or DSPAR, was presented and is capable of full orthogonality between modes. The main benefit of using DSPAR for OAM multiplexing is that it can be implemented with a small number of compact, low-cost single-element antennas, instead of a large continuous aperture structure. As a result, DSPAR can be scaled to receive OAM multiplexing links from an OAM Bull's eye antenna at much larger distances than existing millimetre-wave OAM links which require continuous receiving apertures.

7.3.1 Future work

The feeding technique is an obvious challenge because the two waveguides are too close to each other for standard WR-15 flanges to be used. To solve this problem, two different approaches are proposed. A first solution could be to use a custom waveguide extension to extend the feed waveguides, separating them so as to allow the use of standard WR-15 flanges. A 3D printing process and a copper depositing could be used for this. A second solution could be to use a microstrip-to-waveguide transition, such as that proposed in Chapter 4. This approach allows for very low profile designs at the expense of bandwidth and higher losses induced by the dielectric substrate.

Subsequently, a key aspect of the circular, travelling-wave resonator is the capability to generate two simultaneous OAM modes $\pm l$ when fed by a waveguide 90° hybrid coupler as proposed by Hui *et al.* [99]. However, using hollow waveguides in order to obtain phase quadrature between the two outputs of the coupler results in a bulky ensemble. Using a microstrip-based 90° hybrid coupler, and microstrip-to-waveguide transition proposed in Section 4.2, could drastically reduce the size of the system to feed the OAM Bull's eye antenna. Figure 7.1 illustrates a proof of concept, with the output ports of the 90° hybrid coupler

connected to the two microstrip-to-waveguide transitions. Additional investigation is necessary to optimise the design and analyse the purity of the generated OAM modes.

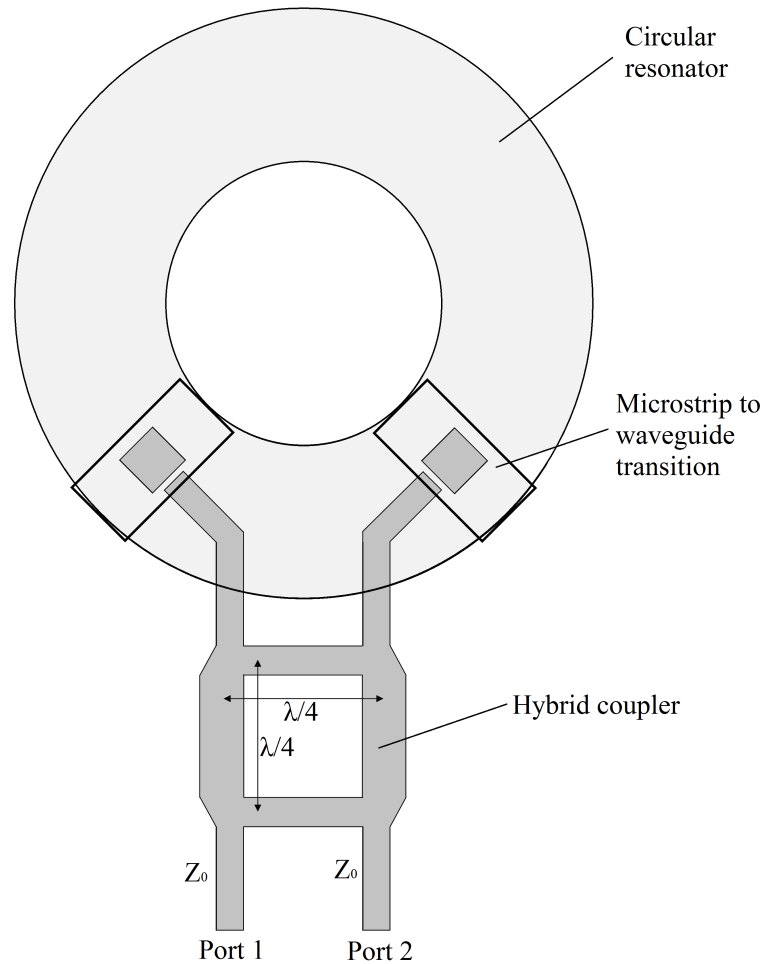


Figure 7.1: Plan view schematic of a microstrip-based, 90° hybrid coupler, and microstrip-to-waveguide transition proposed in Section 4.2.

7.4 CalSat Project

This Section describes the future work related to the improvement of the CalSat payload, that would be based on two Bull’s eye antennas integrated onto a single plate so as to reduce the overall size of the satellite. CalSat is a CubeSat-based satellite developed to offer a controlled calibration space-based platform for the

CMB community. The details of the project have been published by Johnson *et al.* [110].

The cosmic microwave background (CMB) is the electromagnetic radiation of the primordial state of the universe, left after the Big Bang, and characterised by microwave black-body radiation peaking at 160 GHz. Current observation equipment includes satellite and high-altitude, balloon borne, payloads. One of the many challenges for this type of observation relies on the calibration quality of the receivers. A ground-based calibration is excluded due to the difference in the background noise between a receiver pointing toward the horizon and nadir. So far, cosmological objects have been used, for example the supernovae Tau A as noted by [111]. However, those sources are not punctual nor purely polarised, increasing the uncertainty regarding the calibration quality. CalSat can offer an alternative to cosmological objects by providing controlled calibration signals spread across the spectrum of interest. Figure 7.2 shows an exploded view of CalSat.

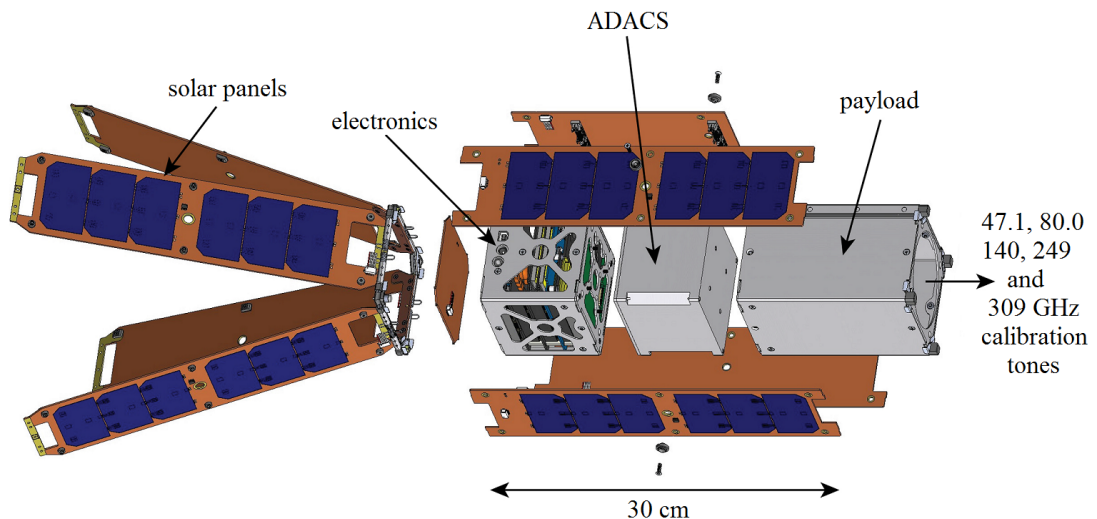
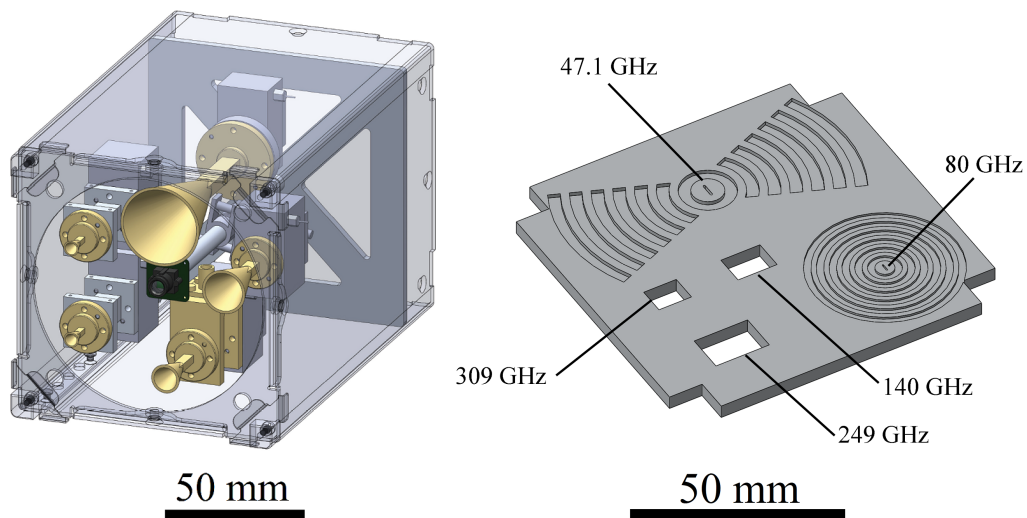


Figure 7.2: Exploded view of CalSat showing the different core elements. The 4 circular horn antennas (47.1, 80, 140 and 309 GHz) are located in the payload
 ©The Authors, Bradley R. Johnson et al, J. Astron. Instrum. 04, 1550007 (2015).

At this stage of the development, the first version of CalSat is based on five standard 20 dBi conical horn antennas operating at 47.1, 80, 140, 249 and 309 GHz. At these frequencies, the length of these antennas are respectively 60 mm, 37 mm, 19 mm, 16.5 mm and 14 mm. The length of the largest antenna (47.1 GHz) constraints the minimal volume of the payload. Replacing the 47.1

and the 80 GHz horn antennas by Bull’s eye antenna structures can save up to 50% of the CalSat payload volume. As shown in Figure 7.3, a single plate solution is particularly attractive and is similar to the design studied in Chapter 4. As investigated in Chapter 5, the design of a 47.1 GHz tone can take advantage of the concentration of the electric field distribution alongside the E-plane. This allows a reduction of the surface required by the corrugated area while keeping a high directivity.



(a) Perspective view of the first version of the CalSat payload using five conical horn antennas ©The Authors, Bradley R. Johnson et al, *J. Astron. Instrum.* 04, 1550007 (2015).

(b) Perspective view of the 47.1 and the 80 GHz Bull’s eye antennas integrated onto a single plate with cut outs for the 140, 249 and 309 GHz rectangular horn antennas.

Figure 7.3: Illustration of the first version version of the CalSat payload, and proposed single plate alternative integrating two Bull’s eye antennas for the 47.1 and 80 GHz tones.

Preliminary simulation results carried out with CST MWS showed a good performance of the Bull’s eye antenna in terms of gain, but a complete and thorough investigation is necessary to evaluate the viability of this option. In particular, it is necessary to meet the strict requirements of the CMB calibration systems, including the polarisation purity and the coupling between the tones. Nonetheless, the poof-of-concept shown in this Section provides a good starting point to investigate more compact and more suitable payload designs based on Bull’s eye antennas for the CalSat project, and for future CubeSat missions in general.

Appendix A

Regulatory policies for frequency spectrum allocation

The use of the electromagnetic spectrum is strictly regulated so as to manage demand and avoid conflict between a large and disparate user base, from consumers to the military [2, 112]. The radio spectrum, ranging from 3 kHz to 300 GHz, is divided into different frequency bands, allocated by international organizations, as shown in Figure A.1.

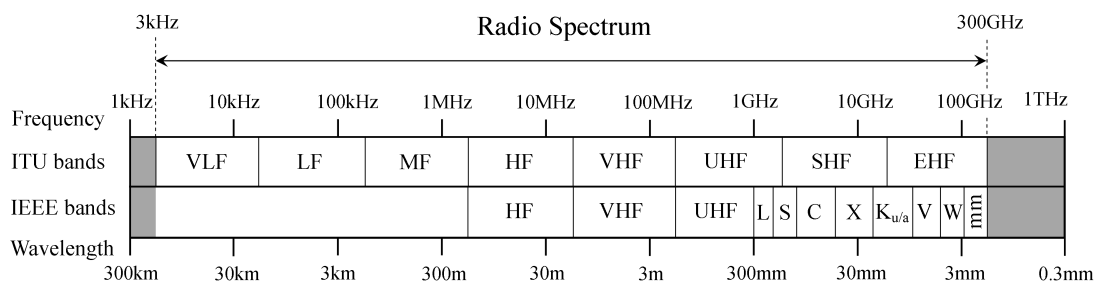
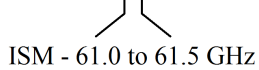


Figure A.1: Distribution of the ITU and IEEE band designations across the radio spectrum (3 kHz-300 GHz).

The International Telecommunication Union (ITU) is the main agency that promotes and organizes the global standardisation around the world. Each of these bands has strict regulations and are classified according to their application purposes. Small disparities exist between continents and countries where local agencies are in charge of the regulation, such as the Federal Communications Commission (FCC) for the USA [113]. The 59 to 71 GHz band is of interest

in this Thesis and is shared between the fixed, mobile, mobile-satellite, radio-location, radio-navigation, earth exploration-satellite, space research and inter-satellite services, as illustrated in Figure A.2.

59.0		59.3		64.0		65.0		66.0		71.0 GHz	
Intersatellite service		Intersatellite service		Intersatellite service		Intersatellite service		Intersatellite service		Intersatellite service	
Earth exploration (passive)	Space research (passive)	Radiolocation		Fixed		Earth exploration (passive)	Space research (passive)	Radio-navigation		Radio-navigation satellite	
								Radio-location		Fixed	
Fixed		Fixed		Mobile		Fixed		Fixed		Fixed	
Mobile		Mobile				Mobile		Mobile		Mobile	



 ISM - 61.0 to 61.5 GHz

Figure A.2: Graphic showing bandwidth allocated to services between 59 and 71 GHz, including the inter-satellite service (ISS), top and the ISM service, bottom.

The inter-satellite service (ISS) is regulated by four recommendations made by the ITU [2]:

1. Recommendation 5.553: in the band 66-71 GHz, the land mobile service may be operated subject to not causing harmful interference to the space radiocommunication services to which these bands are allocated.
2. Recommendation 5.556A: the use of the band 59.0-59.3 GHz by the inter-satellite service is limited to satellites in the geostationary-satellite orbit.
3. Recommendation 5.558: in the bands 59-64 GHz and 66-71 GHz, the land mobile service may be operated subject to not causing harmful interference to the space radiocommunication services to which these bands are allocated.
4. Recommendation 5.559: in the band 59-64 GHz, airborne radars in the radiolocation service may be operated subject to not causing harmful interference to the inter-satellite service.

Recommendation 5.556.A restricts the use of the 300 MHz-wide band from 59.0-59.3 GHz to satellites on geostationary orbits (GEO). The recommendations

5.553, 5.558 and 5.559 protect the use of the 59-71 GHz band for inter-satellite purposes, restricting the use of the other services not to cause interferences to the ISS. Given the severe atmospheric attenuation, it is presently unlikely for land services to interfere with space services. As a results, 11.7 GHz of bandwidth is available for the inter-satellite service as primary user for satellites in the low-earth orbit.

In addition to the regulated services shown in Figure A.2, several countries allocated in the early 2000s large portions of the radio spectrum around 60 GHz for licence exempt, also called unlicensed, terrestrial wireless devices. Those allocated frequency bands have bandwidths ranging between 3.5 and 9 GHz. For example, the unlicensed 57-64 GHz band for the USA is regulated by the Part 15, Section 15.255, of the Commission’s Rules from the Federal Communications Commission (FCC) [9]. The small disparities between Australia, China, the European Union, Japan, North America (Canada and USA), and South Korea are summarised in Figure A.3:

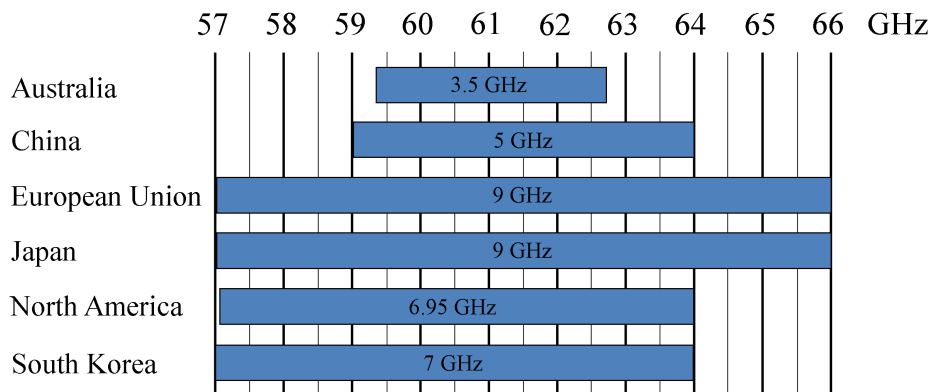


Figure A.3: Frequency bands between 57 and 66 GHz for unlicensed terrestrial wireless devices in the main regulated countries.

In particular, the amount of transmitted power is limited by regulations (e.g. 40 dBm average EIRP in North America [9]) and users need to accept interferences caused by the regulated services.

Appendix B

Ring shifting schemes

Based on the design of the Bull's eye antenna presented in the Chapter 4, two main design schemes to modulate the grating period are considered:

1. A raised ring shift scheme
2. An indented ring shift scheme

For each of those schemes, the type of ring indicated (raised or indented) indicates the type of ring for which the dimensions remain constant. More specifically, the raised ring shift scheme is as described in Section 5.1.1. The limits of the *Shift* value depends on $R_{indented}$, which is 2.67 mm.

The raised shifting scheme retains the same dimensions for the raised rings, but allows the indented portion to change size, as shown in Figure B.1(a,b).

The indented ring shift scheme, illustrated in Figure B.1(c,d), is achieved a similar way. However, the raised ring shift scheme is preferable to the indented ring shift scheme because the latest reduces the degree of beam deflection, reduces the gain, and introduces unwanted side lobes in the radiation pattern, as illustrated in Figure B.2, for $Shift = 1.50$ mm.

Both structures were studied for multiple *Shift* values between 0.00 and 2.67 mm. The comparison between the two structures is shown for one value of shifting ($Shift = 1.50$ mm), but the results are consistent over the entire range of shifting values. The raised ring shift structure (B.1(a,b)) provides better results with a larger maximum gain (+2.81 dB) and lower secondary lobe levels. In particular, high secondary lobe levels can be observed around -43° and 41° on the

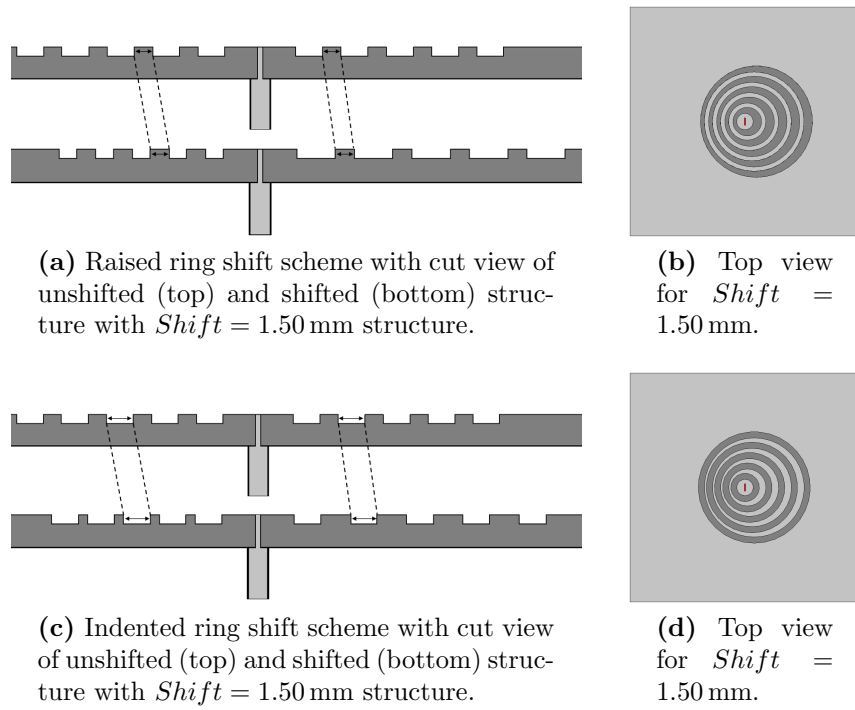


Figure B.1: Schematic view of the raised and indented ring shift schemes.

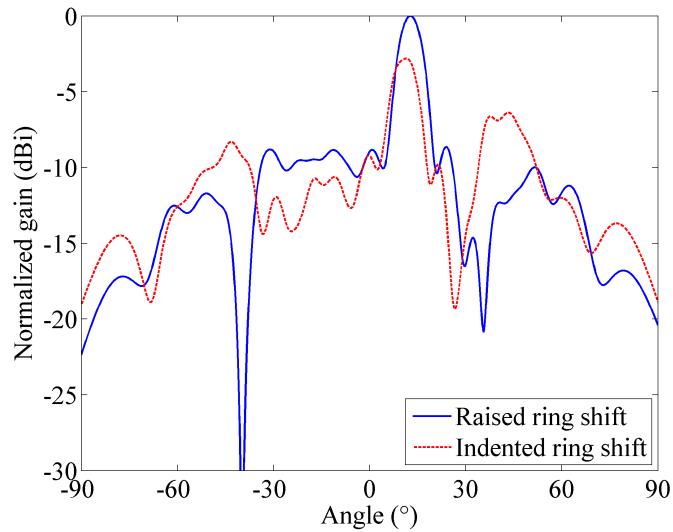


Figure B.2: E-plane radiation pattern for the raised ring shift and indented ring shift schemes with $Shift = 1.50$ mm.

indented ring shift structure. Moreover, the raised ring shift structure exhibits in this case an angle deflection of 12.7° , larger than the 11.4° of the other structure. For those reasons, the raised ring shift scheme appears to be the most efficient

option and hence, served as a reference design for the subsequent investigations.

Appendix C

Low-profile antenna package for inter-CubeSat communication

A double V-band Bull's eye antenna allowing TX and RX links over orthogonal polarisations is presented in this Section [114]. Most of the commercially available 60 GHz modules, developed mainly for terrestrial applications, are only able to transmit or receive. An orthogonal polarisation-based link is a good solution to provide a full-duplex transmission. To do so, a single 0.5U module was designed, comprised of two Bull's eye antennas with two linear polarizations, orthogonal to each other, as shown in Figure C.1. It was decided to limit as much as possible the size of the Bull's eye in order to integrate the two antennas over a 0.5U plate.

All the antennas were modelled using CST MWS. The 60 GHz antennas simulations used the transient solver, and the 2.4GHz antenna the frequency domain solver. As shown in Figure C.2(a,b), each antenna has five indented rings which provide a maximum gain of 18.0 dBi. As shown in Figure C.2(c), the S11 bandwidth at -10 dB is 4.5 GHz and the S11 parameter for both antennas is almost identical. The slight asymmetry in the back lobes due to the position of each of the antennas on the 0.5U plate.

In case of misalignment during manoeuvre phase, or as a low data rate backup link, a 2.4 GHz PIFA antenna was designed and integrated onto the same Bull's eye aluminium plate. This antenna, based on the design described in [115], provides an omnidirectional radiation pattern and is not directly influenced by the 60 GHz antennas' corrugated structure, whose profile is much smaller than the

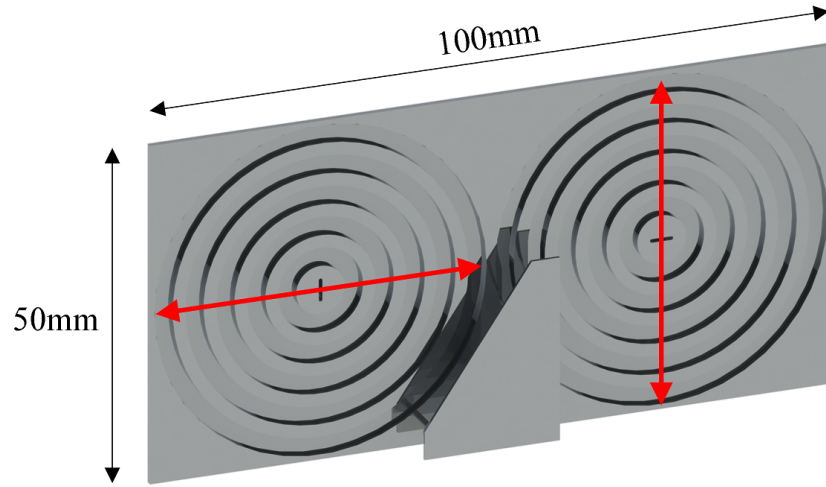


Figure C.1: Antenna package with the two V-band Bull's eye antenna and the S-band PIFA, with polarization planes indicated with a red line.

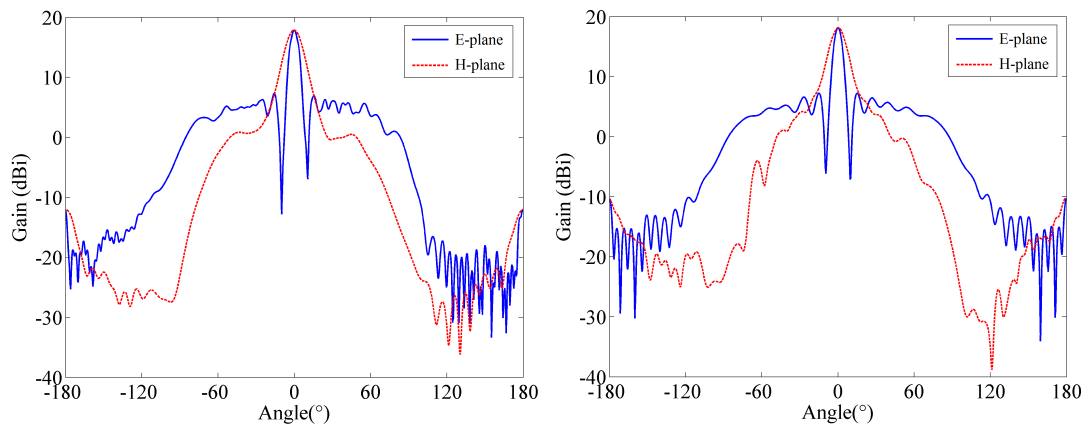
wavelength at 2.4 GHz. Figure C.3 shows the PIFA dimensions, the 3D radiation pattern and S11 parameter between 2.0 and 2.8 GHz.

The 2.4 GHz PIFA provides an omnidirectional pattern, with maximum gain of 4.79 dBi. It is expected that the CubeSat chassis will have only a minor effect on the radiation pattern. The full simulation with the chassis was not run because of the large space domain leads to excessively high memory requirement.

Figure C.4 illustrates the integration of the proposed antenna package on the side of a CubeSat chassis.

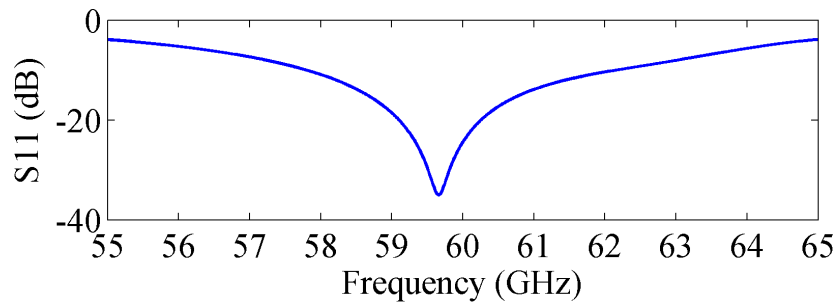
V-band modules are already available for terrestrial application such as the RX and TX waveguide modules from VuBiQ Inc. Based on those modules' features, the maximum expected distance transmission, with a 10 mW transmitter and a 6 dB noise figure receiver, is about 300 m in order to reach a desired bit error rate of 10^{-6} in BPSK modulation, with a potentially achievable data rate of 500 Mbps, as shown in Figure C.5.

The effect of the error in the polarization orientation is only noticeable for values $> 30^\circ$, yet ADCS operate with accuracy $< 1^\circ$, hence it was not taken in account [116]. The maximum distance of 300 m has to be improved in order to suit CubeSat missions such as OLFAR, requiring several kilometres between members of the distributed aperture. Because of the limited available space, the maximum communication distance can be enhanced by increasing the output RF power and using a receiver with a lower the noise figure. For example, a RF



(a) Plot of the E- and H-plane for the left Bull's eye antenna.

(b) Plot of the E- and H-plane for the right Bull's eye antenna.



(c) Plot of the S11 parameter for both Bull's eye antennas.

Figure C.2: Plot of simulated data for each 60 GHz antenna. E- and H-plane for the left (a) and right (b) Bull's eye antenna. S11 parameter is plotted between 55 and 65 GHz identical for both Bull's eye antennas (c).

power of 100 mW and a receiver with a noise figure of 3 dB can help to increase the maximum transmission distance up to 1700 m.

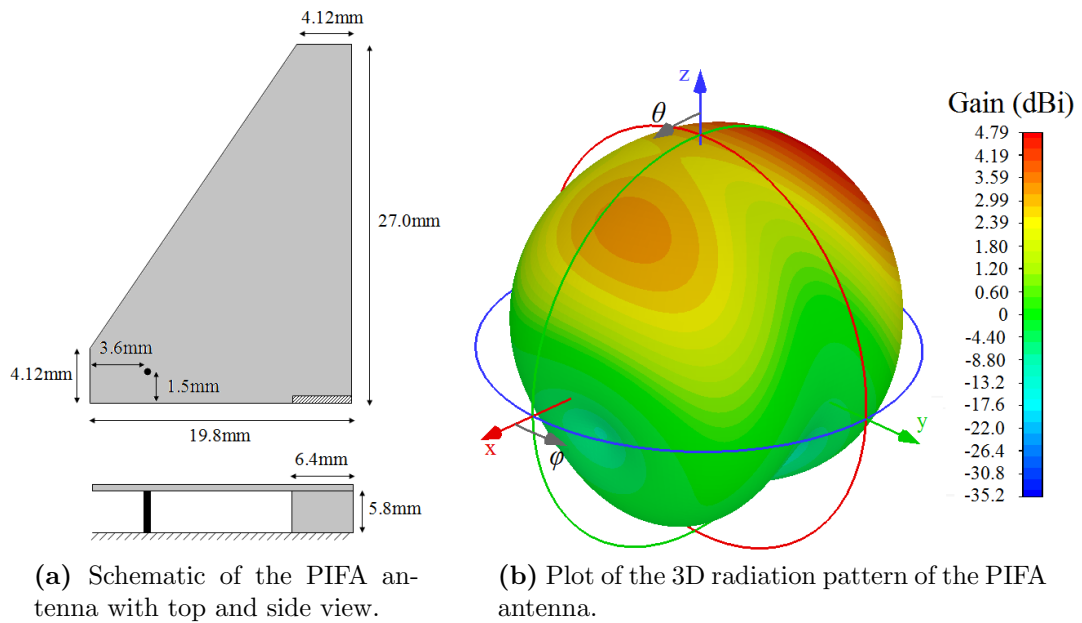


Figure C.3: Plot of simulated data for each 60 GHz antenna. E- and H-plane for the left (a) and right (b) Bull's eye antenna. S11 parameter is plotted between 55 and 65 GHz identical for both Bull's eye antennas (c).

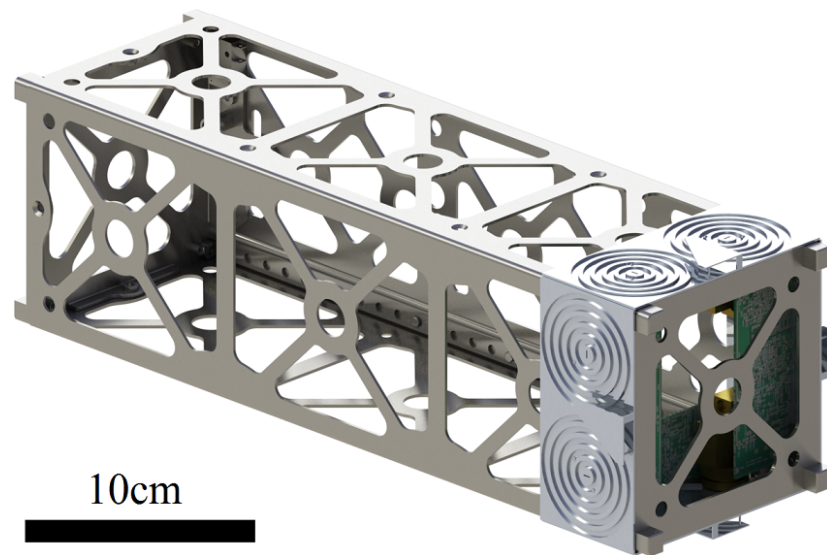
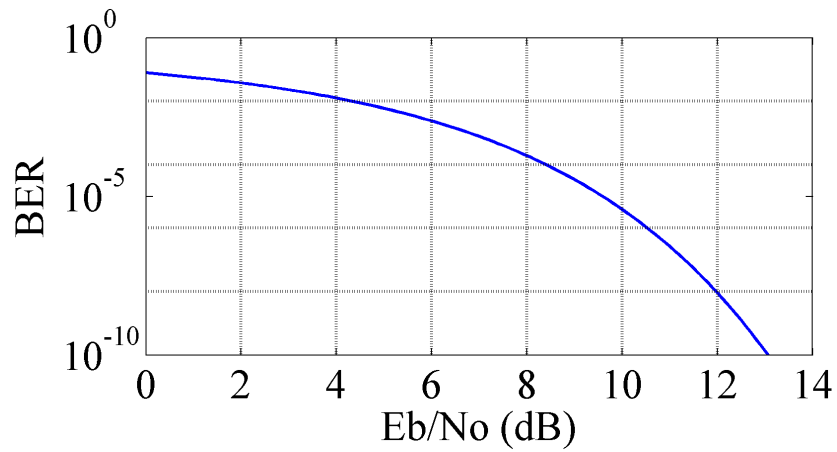
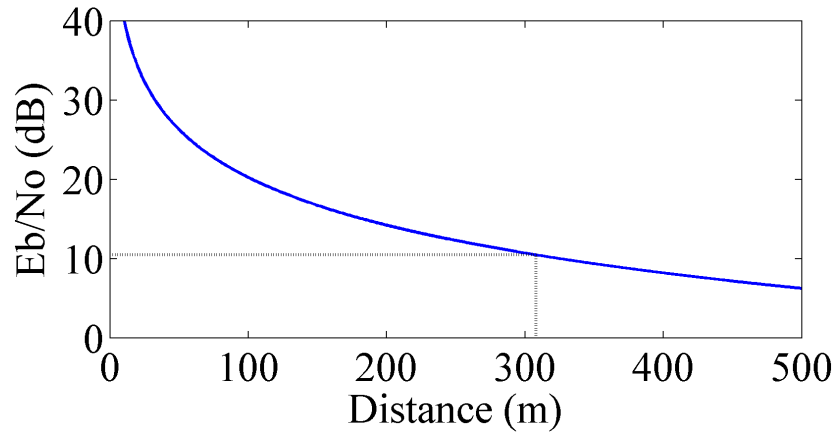


Figure C.4: Illustration of antenna packages attached to the four sides of a 3U CubeSat chassis.



(a) Standard curve showing the bit error rate as a function of E_b/N_o for a BPSK modulation scheme.



(b) Calculated E_b/N_o as a function of the distance.

Figure C.5: Performance of the point-to-point communication at 60 GHz using a BPSK modulation scheme.

References

- [1] *Innovate UK - Digital economy strategy 2015-2018*, February 2015, available at https://www.gov.uk/government/uploads/system/uploads/attachment_data/file/404743/Digital_Economy_Strategy_2015-18_Web_Final2.pdf.
- [2] *Radio Regulations Articles*. International Telecommunication Union (ITU), 2012, ch. I.
- [3] FCC, *Bulletin Number 70 - Millimeter Wave Propagation: Spectrum Management Implications*. Federal Communications Commission, July 1997, available at https://transition.fcc.gov/Bureaus/Engineering_Technology/Documents/bulletins/oet70/oet70a.pdf.
- [4] ITU-R, *Recommendation S.1327: Requirements and suitable bands for operation of the inter-satellite service within the range 50.2-71GHz*. International Telecommunication Union, 1997.
- [5] “IEEE Standard for Information technology– Local and metropolitan area networks– Specific requirements– Part 15.3: Amendment 2: Millimeter-wave-based Alternative Physical Layer Extension,” *IEEE Std 802.15.3c-2009 (Amendment to IEEE Std 802.15.3-2003)*, pp. 1–200, Oct 2009.
- [6] M. Pettus, *White Paper: The Benefits of 60 GHz Broadband Wireless Communications Technology*. Vubiq Networks, April 2015.
- [7] E. Grass, K. Tittelbach-Helmrich, C. Choi *et al.*, “Communication systems operating in the 60 GHz ISM band: Overview,” *International Journal of Microwave and Wireless Technologies*, vol. 3, pp. 89–97, 4 2011.
- [8] FCC, *FCC Increases 5GHz Spectrum for Wi-Fi, Other Unlicensed Uses*. Federal Communications Commission, March 2014.

-
- [9] FCC, *Part 15 Rules for Unlicensed Operation in the 57-64 GHz Band*. Federal Communications Commission, August 2013, available at <https://www.fcc.gov/document/part-15-rules-unlicensed-operation-57-64-ghz-band>.
- [10] “IEEE Standard for Information technology–Telecommunications and information exchange between systems–Local and metropolitan area networks–Specific requirements–Part 11: Wireless LAN Medium Access Control (MAC) and Physical Layer (PHY) Specifications Amendment 3: Enhancements for Very High Throughput in the 60 GHz Band,” *IEEE Std 802.11ad-2012 (Amendment to IEEE Std 802.11-2012, as amended by IEEE Std 802.11ae-2012 and IEEE Std 802.11aa-2012)*, pp. 1–628, Dec 2012.
- [11] *White Paper - 802.11ad - WLAN at 60 GHz: A Technology Introduction*. Rohde & Schwarz, November 2013, available at https://cdn.rohde-schwarz.com/pws/dl_downloads/dl_application/application_notes/1ma220/1MA220_1e_WLAN_11ad_WP.pdf.
- [12] H. Vardhan, S.-R. Ryu, B. Banerjee *et al.*, “60 GHz wireless links in data center networks,” *Computer Networks*, vol. 58, pp. 192 – 205, 2014.
- [13] M. Marcus and B. Pattan, “Millimeter wave propagation: spectrum management implications,” *Microwave Magazine, IEEE*, vol. 6, no. 2, pp. 54–62, June 2005.
- [14] ITU-R, *Recommendation P.676-10: Attenuation by atmospheric gases*. International Telecommunication Union, 2013.
- [15] Futron, *Space Transportation Costs: Trends in Price Per Pound to Orbit 1990-2000*. Futron Corporation, September 2002.
- [16] A. Toorian, K. Diaz, and S. Lee, “The CubeSat Approach to Space Access,” in *Aerospace Conference, 2008 IEEE*, March 2008, pp. 1–14.
- [17] D. Selva and D. Krejci, “A survey and assessment of the capabilities of Cubesats for Earth observation,” *Acta Astronautica*, vol. 74, pp. 50–68, 2012.

-
- [18] H. Heidt, J. Puig-Suari, A. Moore *et al.*, “CubeSat: A new Generation of Picosatellite for Education and Industry Low-Cost Space Experimentation,” in *Proceedings of the Thirteenth Annual AIAA/USU Small Satellite Conference*, Logan, UT, August 2000.
- [19] *CubeSat Design Specification Rev. 12*. The CubeSat Program - Cal Poly SLO, 2009.
- [20] M. Swartwout. (2016) CubeSat Database. [Online]. Available: <https://sites.google.com/a/slu.edu/swartwout/home/cubesat-database>
- [21] J. Bouwmeester and J. Guo, “Survey of worldwide pico- and nanosatellite missions, distributions and subsystem technology,” *Acta Astronautica*, vol. 67, no. 78, pp. 854–862, 2010.
- [22] G. Richardson, K. Schmitt, M. Covert, and C. Rogers, “Small Satellite Trends 2009-2013,” in *Proceedings of the AIAA/USU Conference on Small Satellites*, 2015.
- [23] S. Siceloff, “CubeSat Launchers Expected to Open Research Opportunities for All,” in *NASA*, October 2015, available at <http://www.nasa.gov/feature/cubesat-launchers-expected-to-open-research-opportunities-for-all>.
- [24] R. L. Ltd. (2016) Electron - Rocket Lab. [Online]. Available: <https://www.rocketlabusa.com/>
- [25] I. Bekey, *Advanced Space System Concepts and Technologies: 2010-2030+*. AIAA, May 2003.
- [26] R. Rodriguez-Osorio and E. Fueyo Ramirez, “A Hands-On Education Project: Antenna Design for Inter-CubeSat Communications,” *Antennas and Propagation Magazine, IEEE*, vol. 54, no. 5, pp. 211–224, Oct 2012.
- [27] E. Gill, P. Sundaramoorthy, J. Bouwmeester, B. Zandbergen, and R. Reinhard, “Formation flying within a constellation of nano-satellites: The QB50 mission,” *Acta Astronautica*, vol. 82, no. 1, pp. 110–117, 2013, 6th International Workshop on Satellite Constellation and Formation Flying.

-
- [28] *Telescoping Boom Systems*, Orbital ATK, 2015, available at http://www.orbitalatk.com/space-systems/space-components/deployables/docs/FS028_15%20Telescoping%20Boom%20Systems.pdf.
- [29] *Coilable Boom Systems*, Orbital ATK, 2015, available at <http://www.orbitalatk.com/space-systems/space-components/deployables/docs/Fact%20Sheet%20-%20Coilable%20Boom%20Systems.pdf>.
- [30] S. Engelen, C. Verhoeven, and M. Bentum, “OLFAR a radio telescope based on nano satellites in moon orbit,” in *Proceedings of the 24th Annual Conference on Small Satellites*. Utah, USA: Utah State University, August 2010.
- [31] S. Engelen, K. Quillien, C. Verhoeven *et al.*, “The road to OLFAR - a roadmap to interferometric long-wavelength radio astronomy using miniaturized distributed space systems,” in *Proceeding of the 64th IAC International Astronautical Congress*. International Astronautical Federation (IAF), August 2013, pp. 1–7.
- [32] P. Muri and J. McNair, “A Survey of Communication Sub-systems for Intersatellite Linked Systems and CubeSat Missions,” *Journal of Communications*, vol. 7, no. 4, pp. 290–308, April 2012.
- [33] J. Costantine, Y. Tawk, A. Ernest *et al.*, “Deployable antennas for CubeSat and space communications,” in *Antennas and Propagation (EUCAP), 2012 6th European Conference on*, March 2012, pp. 837–840.
- [34] A. Budianu, T. Castro, A. Meijerink *et al.*, “Inter-satellite links for cube-sats,” in *Aerospace Conference, 2013 IEEE*, March 2013, pp. 1–10.
- [35] *The inter-satellite service*, ser. Telecommunications. Institution of Engineering and Technology, 1999.
- [36] “IEEE Standard Definitions of Terms for Antennas,” *IEEE No 145-1969*, pp. 1–10, Jan 1969.
- [37] J. Kraus, *Antennas*. New York: McGraw-Hill, 1950.
- [38] J. Kraus and R. Marhefka, *Antennas For All Applications, 3rd Edition*. New York: McGraw-Hill, 2002.

-
- [39] J. Poynting, “On the Transfer of Energy in the Electromagnetic Field,” *Philosophical Transactions of the Royal Society of London*, vol. 175, pp. 343–361, 1884.
- [40] “IEEE Standard Definitions of Terms for Antennas,” *IEEE Std 145-1993*, pp. 1–32, July 1993.
- [41] C. Balanis, *Antenna Theory: Analysis and Design, 3rd Edition*. Hoboken, New Jersey: Wiley-Interscience, May 2005.
- [42] H. Friis, “A Note on a Simple Transmission Formula,” *Proceedings of the IRE*, vol. 34, no. 5, pp. 254–256, May 1946.
- [43] J. Kraus and M. R.J., *Antennas For All Applications (3rd Edition)*. Singapore: McGraw-Hill Education, 2001.
- [44] D. Jackson, C. Caloz, and T. Itoh, “Leaky-Wave Antennas,” *Proceedings of the IEEE*, vol. 100, no. 7, pp. 2194–2206, July 2012.
- [45] F. Monticone and A. Al, “Leaky-Wave Theory, Techniques, and Applications: From Microwaves to Visible Frequencies,” *Proceedings of the IEEE*, vol. 103, no. 5, pp. 793–821, May 2015.
- [46] L. Goldstone and A. Oliner, “Leaky-wave antennas I: Rectangular waveguides,” *Antennas and Propagation, IRE Transactions on*, vol. 7, no. 4, pp. 307–319, October 1959.
- [47] S. Podilchak, A. Freundorfer, and Y. Antar, “Broadside Radiation From a Planar 2-D Leaky-Wave Antenna by Practical Surface-Wave Launching,” *Antennas and Wireless Propagation Letters, IEEE*, vol. 7, pp. 517–520, 2008.
- [48] S. Podilchak, P. Baccarelli, P. Burghignoli *et al.*, “Analysis and Design of Annular Microstrip-Based Planar Periodic Leaky-Wave Antennas,” *Antennas and Propagation, IEEE Transactions on*, vol. 62, no. 6, pp. 2978–2991, June 2014.
- [49] H. J. Lezec, A. Degiron, E. Devaux *et al.*, “Beaming Light from a Subwavelength Aperture,” *Science*, vol. 297, no. 5582, pp. 820–822, 2002.

-
- [50] O. Mahboub, S. C. Palacios, C. Genet *et al.*, “Optimization of bull’s eye structures for transmission enhancement,” *Opt. Express*, vol. 18, no. 11, pp. 11 292–11 299, May 2010.
- [51] R. Stanley, “Plasmonics in the mid-infrared,” *Nat Photon*, vol. 6, no. 7, pp. 409–411, 2012.
- [52] M. Beruete, I. Campillo, J. Dolado *et al.*, “Very low-profile ”Bull’s Eye” feeder antenna,” *Antennas and Wireless Propagation Letters, IEEE*, vol. 4, pp. 365–368, 2005.
- [53] P. Baccarelli, P. Burghignoli, G. Lovat *et al.*, “A novel printed leaky-wave ’bull-eye’ antenna with suppressed surface-wave excitation,” in *Antennas and Propagation Society International Symposium, 2004. IEEE*, vol. 1, June 2004, pp. 1078–1081.
- [54] S. Podilchak, P. Baccarelli, P. Burghignoli *et al.*, “Optimization of a Planar ”Bull-Eye” Leaky-Wave Antenna Fed by a Printed Surface-Wave Source,” *Antennas and Wireless Propagation Letters, IEEE*, vol. 12, pp. 665–669, 2013.
- [55] G. Floquet, “Sur les quations differentielles linaires coefficients priodiques,” *Annales scientifiques de l’cole Normale Suprieure*, vol. 12, pp. 47–88, 1883.
- [56] M. Beruete, I. Campillo, J. Dolado *et al.*, “Enhanced microwave transmission and beaming using a subwavelength slot in corrugated plate,” *Antennas and Wireless Propagation Letters, IEEE*, vol. 3, no. 1, pp. 328–331, Dec 2004.
- [57] M. Diaz, I. Campillo, J. Dolado *et al.*, “Dual-band low-profile corrugated feeder antenna,” *Antennas and Propagation, IEEE Transactions on*, vol. 54, no. 2, pp. 340–350, Feb 2006.
- [58] C. Huang, Z. Zhao, and X. Luo, “Application of ”bull’s eye” corrugated grooves integrated with artificially soft surfaces structure in the patch antenna to improve radiation performance,” *Microwave and Optical Technology Letters*, vol. 51, no. 7, pp. 1676–1679, 2009.

-
- [59] G. Minatti, F. Caminita, M. Casaletti, and S. Maci, "Spiral Leaky-Wave Antennas Based on Modulated Surface Impedance," *Antennas and Propagation, IEEE Transactions on*, vol. 59, no. 12, pp. 4436–4444, Dec 2011.
- [60] M. Beruete, U. Beaskoetxea, M. Zehar *et al.*, "Terahertz Corrugated and Bull's-Eye Antennas," *Terahertz Science and Technology, IEEE Transactions on*, vol. 3, no. 6, pp. 740–747, Nov 2013.
- [61] U. Beaskoetxea, M. Navarro-Cia, F. Falcone *et al.*, "Extraordinary-transmission-inspired Bull's eye antenna for automotive radar," in *Radio Science Meeting (Joint with AP-S Symposium), 2014 USNC-URSI*, July 2014, pp. 272–272.
- [62] U. Beaskoetxea, V. Pacheco-Pena, B. Orazbayev *et al.*, "High gain flat sinusoidal Bull's Eye leaky millimetre-wave antenna," in *Antennas and Propagation (EuCAP), 2015 9th European Conference on*, April 2015, pp. 1–2.
- [63] U. Beaskoetxea, V. Pacheco-Pena, B. Orazbayev *et al.*, "77-GHz High-Gain Bull's-Eye Antenna With Sinusoidal Profile," *Antennas and Wireless Propagation Letters, IEEE*, vol. 14, pp. 205–208, 2015.
- [64] C. Vourch and T. Drysdale, "V-Band Bull's Eye Antenna for CubeSat Applications," *Antennas and Wireless Propagation Letters, IEEE*, vol. 13, pp. 1092–1095, 2014.
- [65] C. Vourch and T. Drysdale, "V-band Bull's eye antenna for multiple discretely steerable beams," *IET Microwaves, Antennas & Propagation*, vol. 10, pp. 318–325, February 2016.
- [66] A. Taflove and S. Hagness, *Computational Electrodynamics - The Finite-Difference Time-Domain Method - Third Edition*. Boston London: Artech House, 2005.
- [67] K. Yee, "Numerical solution of initial boundary value problems involving maxwell's equations in isotropic media," *Antennas and Propagation, IEEE Transactions on*, vol. 14, no. 3, pp. 302–307, May 1966.

-
- [68] J. Maxwell, “A dynamical theory of the electromagnetic field,” *Philosophical Transactions of the Royal Society of London*, vol. 155, pp. 459–512, January 1865.
- [69] M. Clemens and T. Weiland, “Discrete electromagnetism with the finite integration technique,” *Progress In Electromagnetics Research*, vol. 32, pp. 65–87, 2001.
- [70] M. Moharam and T. Gaylord, “Rigorous coupled-wave analysis of metallic surface-relief gratings,” *J. Opt. Soc. Am. A*, vol. 3, no. 11, pp. 1780–1787, Nov 1986.
- [71] M. Moharam and T. Gaylord, “Rigorous coupled-wave analysis of planar-grating diffraction,” *J. Opt. Soc. Am.*, vol. 71, no. 7, pp. 811–818, Jul 1981.
- [72] *The Optiscan RCWT calculator*, University of Arizona, available at <http://fp.optics.arizona.edu/milster/optiscan/DOCUMENTATION/RCWTHelp.pdf>.
- [73] P. Keathley and J. Hastings, “Nano-gap-enhanced surface plasmon resonance sensors,” *Plasmonics*, vol. 7, no. 1, pp. 59–69, 2011.
- [74] E. Oberg, F. Jones, H. Horton *et al.*, *Machinery’s Handbook (27th Edition)*. 200 Madison Avenue New York, NY 10016: Industrial Press, 2004.
- [75] *Microwave Absorber Selection Guide - EHP-18PCL Pyramidal Absorber*, ETS-Lindgren, 2003, available at <http://www.ets-lindgren.com/pdf/absorber.pdf>.
- [76] “IEEE Standard Test Procedures for Antennas,” *ANSI/IEEE Std 149-1979*, 1979.
- [77] M. Kowarz, “Homogeneous and evanescent contributions in scalar near-field diffraction,” *Appl. Opt.*, vol. 34, no. 17, pp. 3055–3063, Jun 1995.
- [78] A. Bisognin, D. Titz, F. Ferrero *et al.*, “3D printed plastic 60 GHz lens: Enabling innovative millimeter wave antenna solution and system,” in *Microwave Symposium (IMS), 2014 IEEE MTT-S International*, June 2014, pp. 1–4.

-
- [79] D. Grieg and H. Engelmann, "Microstrip-A New Transmission Technique for the Klilomegacycle Range," *Proceedings of the IRE*, vol. 40, no. 12, pp. 1644–1650, Dec 1952.
- [80] M. Arditi, "Characteristics and Applications of Microstrip for Microwave Wiring," *Microwave Theory and Techniques, IRE Transactions on*, vol. 3, no. 2, pp. 31–56, March 1955.
- [81] H. Wheeler, "Transmission-Line Properties of Parallel Strips Separated by a Dielectric Sheet," *Microwave Theory and Techniques, IEEE Transactions on*, vol. 13, no. 2, pp. 172–185, Mar 1965.
- [82] E. Hammerstad, "Equations for Microstrip Circuit Design," in *Microwave Conference, 1975. 5th European*, Sept 1975, pp. 268–272.
- [83] H. Iizuka, T. Watanabe, K. Sato *et al.*, "Millimeter-wave microstrip line to waveguide transition fabricated on a single layer dielectric substrate," *IE-ICE Transactions on Communications*, vol. 85, pp. 1169–1177, June 2002.
- [84] J.-P. Tetienne, R. Blanchard, N. Yu *et al.*, "Dipolar modeling and experimental demonstration of multi-beam plasmonic collimators," *New Journal of Physics*, vol. 13, no. 5, pp. 53–57, 2011.
- [85] G. Minatti, M. Sabbadini, and S. Maci, "Surface to leaky wave transformation in polarized metasurfaces," in *Electromagnetic Theory (EMTS), Proceedings of 2013 URSI International Symposium on*, May 2013, pp. 298–301.
- [86] G. Minatti, M. Faenzi, E. Martini *et al.*, "Modulated Metasurface Antennas for Space: Synthesis, Analysis and Realizations," *Antennas and Propagation, IEEE Transactions on*, vol. 63, no. 4, pp. 1288–1300, April 2015.
- [87] H. Raether, *Surface plasmons on smooth and rough surfaces and on gratings*. Springer Berlin: Springer Tracts in Modern Physics, 1988, vol. 111.
- [88] J. Gomez-Tornero, "Analysis and Design of Conformal Tapered Leaky-Wave Antennas," *Antennas and Wireless Propagation Letters, IEEE*, vol. 10, pp. 1068–1071, 2011.

-
- [89] H. He, M. E. J. Friese, N. R. Heckenberg *et al.*, “Direct Observation of Transfer of Angular Momentum to Absorptive Particles from a Laser Beam with a Phase Singularity,” *Phys. Rev. Lett.*, vol. 75, pp. 826–829, Jul 1995.
- [90] A. E. Willner, H. Huang, Y. Yan *et al.*, “Optical communications using orbital angular momentum beams,” *Adv. Opt. Photon.*, vol. 7, no. 1, pp. 66–106, Mar 2015.
- [91] Y. Yan, G. Xie, M. Lavery *et al.*, “High-capacity millimetre-wave communications with orbital angular momentum multiplexing,” *Nat Commun*, vol. 5, September 2014.
- [92] M. Oldoni, F. Spinello, E. Mari *et al.*, “Space-Division Demultiplexing in Orbital-Angular-Momentum-Based MIMO Radio Systems,” *Antennas and Propagation, IEEE Transactions on*, vol. 63, no. 10, pp. 4582–4587, Oct 2015.
- [93] L. Allen, M. W. Beijersbergen, R. J. C. Spreeuw *et al.*, “Orbital angular momentum of light and the transformation of Laguerre-Gaussian laser modes,” *Phys. Rev. A*, vol. 45, pp. 8185–8189, Jun 1992.
- [94] P. Schemmel, G. Pisano, and B. Maffei, “Modular spiral phase plate design for orbital angular momentum generation at millimetre wavelengths,” *Opt. Express*, vol. 22, no. 12, pp. 14 712–14 726, Jun 2014.
- [95] V. Bazhenov, V. M.V., and S. M.S., “Laser beams with screw dislocations in their wavefronts,” *JETP Letters*, vol. 52, no. 8, pp. 429–431, Oct 1990.
- [96] L. Marrucci, C. Manzo, and D. Paparo, “Optical Spin-to-Orbital Angular Momentum Conversion in Inhomogeneous Anisotropic Media,” *Phys. Rev. Lett.*, vol. 96, p. 163905, Apr 2006.
- [97] X. Hui, S. Zheng, Y. Chen *et al.*, “Multiplexed Millimeter Wave Communication with Dual Orbital Angular Momentum (OAM) Mode Antennas,” *Scientific Reports*, vol. 5, no. 10148, pp. 1169–1177, 2015.
- [98] Q. Bai, A. Tennant, and B. Allen, “Experimental circular phased array for generating OAM radio beams,” *Electronics Letters*, vol. 50, no. 20, pp. 1414–1415, September 2014.

-
- [99] X. Hui, S. Zheng, Y. Chen *et al.*, “Multiplexed Millimeter Wave Communication with Dual Orbital Angular Momentum (OAM) Mode Antennas,” *Scientific Reports*, vol. 5, no. 10148, May 2015.
- [100] B. Allen, A. Tennant, Q. Bai *et al.*, “Wireless data encoding and decoding using OAM modes,” *Electronics Letters*, vol. 50, no. 3, pp. 232–233, January 2014.
- [101] D. Rabus, *Integrated Ring Resonators The Compendium*. Berlin Heidelberg: Springer-Verlag, 1988.
- [102] H. Huang, G. Milione, M. Lavery *et al.*, “Mode division multiplexing using an orbital angular momentum mode sorter and MIMO-DSP over a graded-index few-mode optical fibre,” *Scientific Reports*, vol. 5, October 2015.
- [103] G. Gibson, J. Courtial, M. Padgett *et al.*, “Free-space information transfer using light beams carrying orbital angular momentum,” *Opt. Express*, vol. 12, no. 22, pp. 5448–5456, Nov 2004.
- [104] A. Yao and M. Padgett, “Orbital angular momentum: origins, behavior and applications,” *Adv. Opt. Photon.*, vol. 3, no. 2, pp. 161–204, Jun 2011.
- [105] G. Molina-Terriza, J. Torres, and L. Torner, “Twisted photons,” *Nat Phys*, vol. 3, pp. 305–310, May 2007.
- [106] G. Xie, Y. Ren, H. Huang *et al.*, “Analysis of aperture size for partially receiving and de-multiplexing 100-Gbit/s optical orbital angular momentum channels over free-space link,” in *Globecom Workshops (GC Wkshps), 2013 IEEE*, Dec 2013, pp. 1116–1120.
- [107] S. Zheng, X. Hui, J. Zhu *et al.*, “Orbital angular momentum mode-demultiplexing scheme with partial angular receiving aperture,” *Opt. Express*, vol. 23, no. 9, pp. 12 251–12 257, May 2015.
- [108] S. Franke-Arnold, S. Barnett, E. Yao *et al.*, “Uncertainty principle for angular position and angular momentum,” *New Journal of Physics*, vol. 6, no. 1, p. 103, 2004.

-
- [109] E. Cano and B. Allen, “Multiple-antenna phase-gradient detection for OAM radio communications,” *Electronics Letters*, vol. 51, no. 9, pp. 724–725, 2015.
- [110] B. Johnson, C. Vourch, T. Drysdale *et al.*, “A CubeSat for Calibrating Ground-Based and Sub-Orbital Millimeter-Wave Polarimeters (CalSat),” *Journal of Astronomical Instrumentation*, vol. 4, no. 2, pp. 1 550 007–1 – 1 550 007–18, October 2015.
- [111] J. Kaufman, B. Keating, and B. Johnson, “Precision Tests of Parity Violation Over Cosmological Distances,” January 2015. [Online]. Available: <http://arxiv.org/abs/1409.8242>
- [112] “IEEE Standard Letter Designations for Radar-Frequency Bands,” *IEEE Std 521-2002*, pp. 1–3, 2003.
- [113] *United States Frequency Allocation Chart*, National Telecommunications and Information Administration (NTIA), August 2011, available at https://www.ntia.doc.gov/files/ntia/publications/spectrum_wall_chart_aug2011.pdf.
- [114] C. Vourch and T. Drysdale, “Low-Profile Antenna Package for Efficient InterCubeSat Communication in S- and V-band,” in *4th Interplanetary CubeSat Workshop (iCubeSat 2015)*, London, UK, April 2015.
- [115] B. Kim, J. Park, and H. Choi, “Tapered type PIFA design for mobile phones at 1800 MHz,” in *Vehicular Technology Conference, 2003. VTC 2003-Spring. The 57th IEEE Semiannual*, vol. 2, April 2003, pp. 1012–1014.
- [116] J. Bouwmeester, J. Reijneveld, T. Hoevenaars *et al.*, “Design and verification of a very compact and versatile attitude determination and control system for the Delfi-n3Xt Nano satellite,” in *Proceedings of the 4S Symposium, Portoro, Slovenia*, June 2012.